Optical properties of organic micro and nanostructures

Sergey Semin

Cover image: Schematic representation of the structure of the investigated materials and photophysical process occurring there.

Optical properties of organic micro and nanostructures
PhD Thesis, Radboud University Nijmegen, The Netherlands
Illustrated
With summary in English, Dutch
ISBN 978-94-6259-632-0
printed by Ipskamp Drukkers B.V., Enschede

The work described in this thesis has been financially supported by
the Foundation for Fundamental Research on Matter (FOM),
which is part of the Netherlands Organisation for Scientific Research (NWO), Marie Curie FP7 People.

Optical properties of organic micro and nanostructures

Proefschrift

ter verkrijging van de graad van doctor
aan de Radboud Universiteit Nijmegen
op gezag van de rector magnificus prof. dr. Th. L. M. Engelen,
volgens besluit van het college van decanen
in het openbaar te verdedigen op donderdag 23 april 2015
om 10:30 uur precies

door

Sergey Semin

geboren op 24 Januari 1986
te Bolgrad, USSR

Promotor:	Prof. dr. Th. H. M. Rasing
Manuscriptcommissie:	Prof. dr. A.I. Kirilyuk (voorzitter)
	Prof. dr. V. Subramaniam (UT)
	Prof. dr. J. Knoester (RUG)

Dankwoord

I really liked and enjoyed the time I have spent in Nijmegen doing my Ph.D. It took me more time than was planned, but this time was spent for interesting and exciting projects. A lot of people supported me and this is my chance to express my gratitude to them.

First of all, I would like to thank my promotor prof. dr. Theo Rasing as he gave me possibility to join his group. Theo, thank you for your support, ideas and all the critical reviews of my abstracts, posters, articles, presentations and, finally, this thesis. It is a great pleasure to work in your group.

For me, Albert and Tonnie are not only the people who take care about hardware part of the experiments. They helped me much more. I am grateful to Albert for his guidance, help in designing experiments and sharing his laser wisdom. I wish him to have a lot of health.

Tonnie created two masterpieces which I simply called second harmonic set-up and waveguing set-up in my thesis but the functionality they offer have deserve more beautiful names. Every problem with hardware was immediately solved by Tonnie. Having the nice examples of LabView programs allowed me to improve my programming skills.

Marilou, it is very difficult to overestimate your help with solving administrative problems. Thank you very much!

I would like to thank prof. dr. Huub Salemink for helping me with the first drafts of thesis, especially, for his numerous clever comments and his ideas of the future of my projects.

In addition, I would like to thank the members of manuscript committee: prof. dr. A. I. Kirilyuk, prof. dr. V. Subramaniam and prof. dr. J. Knoester for their time, interest in my work and helpful comments.

I would like to thank my former supervisor prof. Elena Mishina. She was one of the people who have initiated the peptide project and I am very grateful to her for the opportunity to be involved in it.

I am very happy that we have established collaboration with prof. dr. Alan Rowan and dr. Paul Kouwer. Their constructive criticism to my work helped me to improve my articles.

A large part of the work described in this thesis was done together with dr. Jialiang

Xu. Our collaboration with Jialiang showed me beautiful side of chemistry and helped me to obtain deeper understanding of the processes occurring in my materials. Jialiang, thank you very much for everything you contributed to the ideas, the measurements and the articles. I hope that we can finalise all the projects we started.

I would like to thank dr. Ilya Razdolski for his help with my work and writing thesis. Together we have spent a lot of hours counting photons.

It was very pleasant to work with Matteo and Laura. I am grateful to Laura for her help with chemical part of my work. She is one of the most enthusiastic persons I have ever met. I am very appreciated to Matteo for his nice ideas and contribution to the microscopy part of my work. He is also a very nice room mate. Always positive and smiling, he taught me important Italian words and where I can find the best pizza in Nijmegen.

I would like to thank all the people with whom I had the pleasure to work with: Albert, Alexey, Addis, Bowen, Cris, Dima M., Dima A., Ilya, Benny, Davide, Dennis, Diana, Erwin, Fred, Jan, Jeroen, Jos, Yury, Johan d. J., Johan M., Jonas, Peter C., Peter v. Rh., Raja M., Raja G., Remco, Ruslan, Rostislav, Sam, Sascha, Siebe, Tahora, Thomas, Valera, Kadir, Koen, Lars, Magnus, Maxim, Nikita, Natasha, Wei-Ta, Georgy, Yulong and Yusuke.

During my time in the group as Ph.D student I also had a lot of fun. This I owe for a large part to all my colleagues. I will always remember our group day outs, BBQs, sportsdays and volleyball games.

Last but not the least I would like to thank my family. First of all, I am grateful to my wife Anja. Her love, care and support help me a lot. I would like to thank my parents and my brother Alexey for their care and love.

Sergey Semin,
Nijmegen, March 2015

Contents

Introduction

General introduction

Decades of efforts of many research groups all over the world have resulted in the current progress of technology that has brought us tablet size computers more powerful than the supercomputers from the early days, wireless internet, cell phones and the global positioning system we use daily. Such technological breakthroughs became possible due to the decrease of the sizes of electronics components: e.g. transistors in computer chips and domains in hard disk drives decreased from tens of microns to tens of nanometers. This decrease of component dimensions has brought increased performance, efficiency, and low energy consumption of electronic devices. A similar evolution occurred with the development of optoelectronic and photonic devices. Nowadays, it is possible to find tiny laser diodes everywhere from computers to cars.

Not only the smaller size of devices drives the interest for the creation of miniature optoelectronic or purely optical (photonic) devices. The main advantage in using photons instead of electrons is the speed of information transmission and processing: the substitution of copper wires and radio waves with optical fibers allows to transfer gigabytes of data between continents within seconds. The same principles can be applied to the computer, where optical waveguides will be used to transfer data between processor and memory, or even the creation of a optical computer, where ideas of quantum computing can be embodied.

While the electronic industry is already established and mainly based on silicon and metals with high conductivity as copper, for the newly developing photonic devices the search for new materials is still highly relevant. The difference comes from the fact that one can use different wavelengths of light which allows to increase the amount of processed and transmitted data.

Miniaturisation of the components gives rise to the question of what is the proper approach for their fabrication. Two general concepts of fabrication were developed for the creation of components of miniaturized optical devices: top-down and bottom-up.

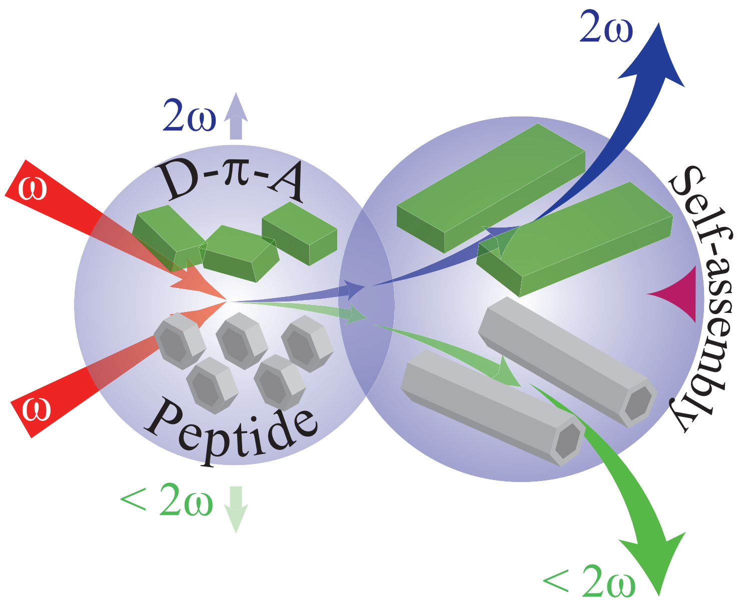

Figure 1: Molecular building blocks can demonstrate the presence of the non-linear optical effects: second harmonic generation (2ω) and two-photoluminescence($< 2\omega$) in solution while excited with intense laser light (with frequency ω). Self-assembly leads to formation of the objects where enhancement of these effects occurs.

The top-down approach delivers precise and size-controlled structures by processing of the bulk material, with e.g. optical lithography or etching. However, top-down techniques have drawbacks as they require expensive and high precision equipment.

The second fabrication strategy is called the bottom-up approach and exploits forces of molecular interaction in order to create nano- and micro objects. The typical example of such fabrication is self-assembly of molecules, where molecular building blocks by means of weak non-covalent bonds arrange in various complex and organised structures. This approach is not so controllable and precise as top-down techniques but offers some advantages such as fast fabrication, flexibility and versatility.

Self-assembly is inspired by nature and can be found in the formation of biological objects like DNA, RNA and proteins. Self-assembly can be applied to a whole class of organic molecules for fabrication of miniaturised optical components leading to efficiency increase of their optical response compared to that of individual molecule (fig. 1). However it also can be used for inorganic materials, namely semiconductors and noble metals, for the creation of quantum dots and metallic nanoparticles. The self-assembly of both organic and inorganic building blocks results in objects with various morphologies and sizes [1].

Both of these fabrication approaches are exploited by science and industry indicating that their strong points are more important than their drawbacks.

The studies demonstrated in this work focus on the optical properties of self-assembled structures fabricated from organic molecules.

State of the art

While organic materials are the theme of the studies shown in this thesis, it is important to mention the other strategies which are used in the exciting world of miniature optics and nanooptics as well.

Indeed, a lot of research was performed in the implementation of organic and inorganic materials as light sources, detectors and transmitters on a micro- and nanoscale [2–4]. The latter application area very often exploits elongated objects like rods or tubes for the propagation of light. One can distinguish two types of waveguiding: passive and active. For passive waveguiding a medium should be transparent for the propagating wavelength, while the total internal reflection effect is used to confine light inside the structure, as the light from the source is transmitted through the medium. The active waveguiding occurs near the absorption band of the material and light generated by the material is propagating though the structure, while the excitation wavelength can be fully absorbed.

Passive waveguiding is widely exploited in silicon optical fibers for high speed data transmission. The same concept but on the microscale was used to track the propagation of a femtosecond pulse through a passive dielectric waveguide made of silicon nitride [5].

One more example of passive waveguiding can be found in devices called photonic crystals (PC) [6; 7]. In a PC, the refractive index periodically changes in one or more dimensions, which can be achieved by, for example, milling of a 2D pattern of holes in metal or dielectric material. Control over the period of the structure allows to discriminate the propagation of light along certain directions confining light inside the PC. This approach allows to create waveguides and mirrors, combining them in something complex like a Mach-Zehnder interferometer, consisting of waveguides, mirrors and beam-splitters on a silicon chip with the size of tens of μm designed for an IR laser with $\lambda = 1.51$ μm (see fig. 2) [8].

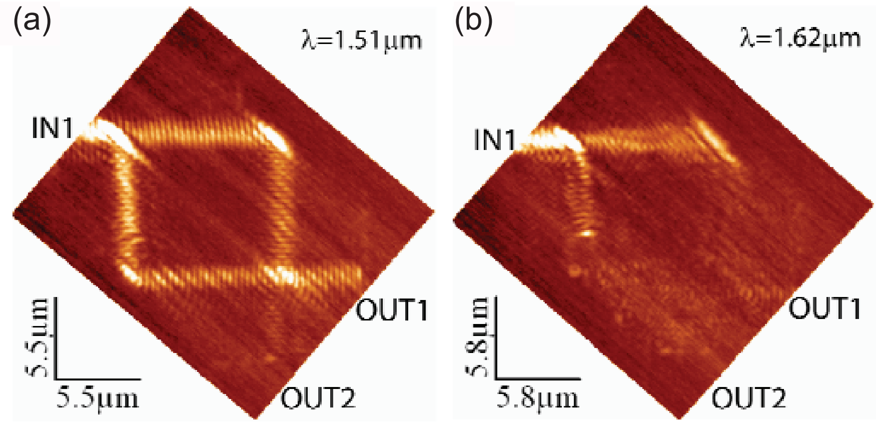

Figure 2: Mach-Zehnder interferometer based on photonic crystal in (a) phase-matching regime where light is collimated and (b) non-matching regime, which results in absence of the light collimation (from ref. [8])

.

A further concept of passive wavequiding uses the surface plasmon which is a coherent oscillation of delocalised electrons that exist at the interface between two materials (one of them is usually a metal). The plasmon can be excited at one end of a metallic nanowire by a focused laser, propagates several micrometers to another one and be outcoupled there as light, which was successfully shown in silver nanowires [9; 10].

The active waveguiding is more related to the area of micro and nanowires. Semiconductor materials like CdS or ZnO can be used for the creation of nanoribbons and nanowires, which demonstrate active waveguiding when operated near their band-edge, since light absorption and emission can occur in this range simultaneously. The arrays of such structures can act as optically or electrically pumped lasers [11; 12].

Organic molecules, e.g polymers which are long chains of identical molecules, readily form wire-like structures of several nanometres in diameter. The use of fluorescent polymers or doping with organic dyes allows to obtain optically active nanofibers and nanolasers in the blue range ($\approx$ 450 nm)[13; 14].

Self-assembly of short molecules of active organic materials also allows to obtain objects which demonstrate such optical effect as waveguiding: both passive and active (fig. 3) [15].

These waveguides can have specific optical properties as low-loss propagation, highly polarised emissions, white-light generation and propagation, possibility of lasing and light generation in the visible and UV range [16].

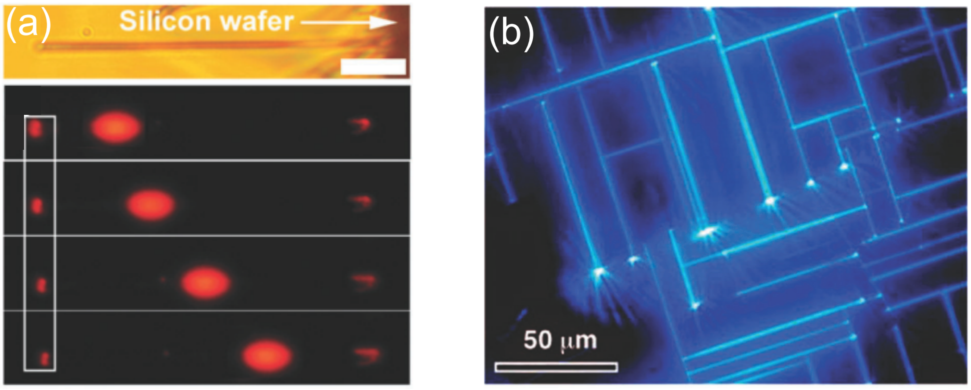

Figure 3: Examples of miniaturised optical waveguiding objects. (a) Organic waveguide based on 1,5-diaminoanthraquinone dye molecules. The picture shows optical microscope image and micro-area excited PL images of the wire taken by exciting each wire at four different positions (scale bar is 10 μm) [15]. White rectangle depicts position of the tube's end; (b) Photoluminescence microscopy image of the needle like crystals epitaxially grown on the shadowed region of the KCl (001) surface with excitation at λ_{ex} = 365 nm [15].

As it can be seen from these examples organic molecules offer easy fabrication together with a variety of adjustable optical properties, morphologies and sizes.

Scope of thesis

This thesis addresses the growth, linear and nonlinear optical characterisation of some self-assembled microsized objects which might find their function in the expanding area of photonic devices. Two molecules were investigated in this thesis: diphenylalanine (FF) and 2,7-diphenyl-9H-fluoren-9-one (DPFO). Both of them are building blocks for the fabrication of elongated microsized objects from solution by means of molecular self-organisation. This is the case for the FF, as it is a natural compound that belongs to the class of peptides, structures formed by amino acids, consisting of two or more blocks connected to each other by peptide bonds. Optical response of this molecule is located in the UV range. The non-covalent interaction makes the FF molecules to form microsized tubes (FFMTs) from a water solution with a noncentrosymmetric crystal lattice.

DPFO is a synthetic organic compound which belongs to the low-weight intramolecular charge-transfer (ICT) molecules. This type of molecules consist of two parts: one is an electron donor and the other as electron acceptor, while the π-conjugation bridges these parts of the molecule. Such a molecular structure makes ICT molecules to be good candidates for diverse optical applications. The π-conjugation of DPFO molecules is more developed than in FF molecules, resulting in the light emission in the green range. This molecule self-assembles into microfibers in a heptane environment.

In this thesis we have studied the structures from FF and DPFO and investigated how their structure influences the nonlinear optical response. As both materials arrange in elongated objects with lengths over hundred microns and well defined crystal lattices, we also studied the possibility of using these structures as waveguides.

This thesis is organised as follows. The first chapter of the thesis is dedicated to the sample fabrication techniques. It starts from the introduction to the self-assembly process, which is followed by descriptions of the structural properties which can influence the linear and non-linear optical properties of the organic materials. The last part of this chapter describes the details of the fabrication of the microstructures based on the FF and DPFO molecules. Some basic structural and physical properties of both materials are described.

Chapter 2 gives an introduction to the basics of nonlinear optical properties of materials. It starts with the description of the light matter interaction followed by details of the second harmonic generation (SHG) as well as the two-photon luminescence (TPL). We discuss the techniques and typical set-ups which can be used for the investigation of the nonlinear optical properties in microsized and nanosized objects. The chapter ends with the description of the optical set-ups which were used for study of the materials described in chapter 1.

The results of the investigation of the FFMTs are presented in chapter 3. The chapter starts with the description of the influence of a magnetic field on the alignment of the microtubes during the self-assembly. Then we study the SHG response of the individual FFMTs and relate it to the crystal structure. Influence of the phase transformation on the nonlinear optical properties occurring in the FFMTs during heat treatment is explained. Phase transformation can give extra functionality to the FFMTs due to the appearance of TPL. The chapter ends with the examination of the waveguiding properties of the individual FFMTs. We also demonstrate how the observed phase transformation can be used for modification of waveguiding properties.

The study of the DPFO microstructures is presented in chapter 4. We demonstrate how the SHG technique is used to study the molecular arrangement inside an individual microfibre. Like for the FFMT, we perform a study of the waveguiding properties of individual DPFO microfibres. Influences of the geometry and environment on the waveguiding of the light is studied in the last part of the chapter.

The thesis is concluded with a summary in English and Dutch.

References

[1] S. Zhang, "Fabrication of novel biomaterials through molecular self-assembly.," *Nat. Biotechnol.*, vol. 21, pp. 1171–8, Oct. 2003.

[2] K.-J. Baeg, M. Binda, D. Natali, M. Caironi, and Y.-Y. Noh, "Organic light detectors: photodiodes and phototransistors.," *Adv. Mat.*, vol. 25, pp. 4267–95, Aug. 2013.

[3] S. H. Kim, S. Park, J. E. Kwon, and S. Y. Park, "Organic Light-Emitting Diodes with a White-Emitting Molecule: Emission Mechanism and Device Characteristics," *Adv. Funct. Mater.*, vol. 21, pp. 644–651, Feb. 2011.

[4] X. Guo, Y. Ying, and L. Tong, "Photonic nanowires: from subwavelength waveguides to optical sensors.," *Acc. Chem. Res.*, vol. 47, pp. 656–66, Feb. 2014.

[5] M. L. Balistreri, H. Gersen, J. P. Korterik, L. Kuipers, and N. F. van Hulst, "Tracking femtosecond laser pulses in space and time.," *Science*, vol. 294, pp. 1080–2, Nov. 2001.

[6] E. Yablonovitch, "Inhibited Spontaneous Emission in Solid-State Physics and Electronics," *Phys. Rev. Lett.*, vol. 58, pp. 2059–2062, May 1987.

[7] S. John, "Strong localization of photons in certain disordered dielectric superlattices," *Phys. Rev. Lett.*, vol. 58, pp. 2486–2489, June 1987.

[8] H. M. Nguyen, M. A. Dundar, R. W. van der Heijden, E. W. J. M. van der Drift, H. W. M. Salemink, S. Rogge, and J. Caro, "Compact Mach-Zehnder interferometer based on self-collimation of light in a silicon photonic crystal.," *Opt. Express*, vol. 18, pp. 6437–46, Mar. 2010.

[9] C. Rewitz, T. Keitzl, P. Tuchscherer, J.-S. Huang, P. Geisler, G. Razinskas, B. Hecht, and T. Brixner, "Ultrafast plasmon propagation in nanowires characterized by far-field spectral interferometry.," *Nano Lett.*, vol. 12, pp. 45–9, Jan. 2012.

[10] A. W. Sanders, D. A. Routenberg, B. J. Wiley, Y. Xia, E. R. Dufresne, and M. A. Reed, "Observation of plasmon propagation, redirection, and fan-out in silver nanowires.," *Nano Lett.*, vol. 6, pp. 1822–6, Aug. 2006.

[11] T. Voss, G. T. Svacha, E. Mazur, S. Müller, C. Ronning, D. Konjhodzic, and F. Marlow, "High-order waveguide modes in ZnO nanowires.," *Nano Lett.*, vol. 7, pp. 3675–80, Dec. 2007.

[12] A. Pan, D. Liu, R. Liu, F. Wang, X. Zhu, and B. Zou, "Optical waveguide through CdS nanoribbons.," *Small*, vol. 1, pp. 980–3, Oct. 2005.

[13] D. O'Carroll, I. Lieberwirth, and G. Redmond, "Microcavity effects and optically pumped lasing in single conjugated polymer nanowires," *Nat. Nano*, vol. 2, pp. 180–184, Mar. 2007.

[14] A. Camposeo, F. Di Benedetto, R. Stabile, A. a. R. Neves, R. Cingolani, and D. Pisignano, "Laser emission from electrospun polymer nanofibers.," *Small*, vol. 5, pp. 562–6, Mar. 2009.

[15] C. Zhang, Y. S. Zhao, and J. Yao, "Optical waveguides at micro/nanoscale based on functional small organic molecules.," *Phys. Chem. Chem. Phys.*, vol. 13, pp. 9060–73, May 2011.

[16] Y. S. Zhao, A. Peng, H. Fu, Y. Ma, and J. Yao, "Nanowire Waveguides and Ultraviolet Lasers Based on Small Organic Molecules," *Adv. Mat.*, vol. 20, pp. 1661–1665, May 2008.

Chapter 1

Sample fabrication

This chapter is an introduction to the history and properties of the organic compounds investigated in this work. Some basic principles related to the fabrication of the structures based on organic materials will be mentioned. Special emphasis will be on the structural features that influence the optical properties of the fabricated structures most strongly. We will discuss details of synthesis, crystal structure of self-assembled objects and their physical properties. Both of the investigated materials self-assemble into noncentrosymmetric microsize crystals and present interesting linear and nonlinear optical properties.

1.1 Synthesis and structure

Organic Molecules (OMs) and devices based on these have already found their place in the optical part of the science and technology world. Liquid crystals displays (LCDs)[1] and organic light emitting diodes (OLEDs) [2] are widely used in modern devices and dyes based on OMs are exploited as markers in optical microscopy [3; 4].

The ability of OMs to self-assemble into highly ordered structures makes them useful for further utilisation of organics into applied technology. The self-assembly is an example of a bottom-up approach where molecules organise into complex structures by weak interactions. The variety of organic molecules together with their fabrication flexibility allows to obtain a huge number of different objects with sizes ranging from a few nanometres to hundreds of microns. This diversity and simplicity of fabrication can be very useful for developing miniaturized optical devices which can find their places in photonic integrated circuits.

Several requirements can be formulated for the OMs to be useful for optical applications. The first one is that a molecule should have an optical response in the desired spectral region, which should be of adequate intensity. This can be tuned by proper designing of the molecule or adding of “guest” molecules or atoms. The ability of the molecule to self-assemble in structures of desired and controllable shape can be the second requirement. It can be achieved by changing the self-assembly conditions and molecule structure. OMs which self-assemble into the elongated shapes like rods, tubes and wires attract special attention because they demonstrate waveguiding properties as light is confined inside the structure due to the difference of the refractive index of the structure and the environment. As last requirement one can name the ability of self-assembled structures to be aligned on the larger scale or to be manipulated individually. This ability is very useful for the implementation of the materials in the technology. These three requirements are quite important; unfortunately it is not always possible to combine all of them in one molecule or structure, which makes the search for new materials of interest.

Two molecules were investigated in this thesis: diphenylalanine (FF) and 2,7-diphenyl-9H-fluoren-9-one (DPFO). Both of them are building blocks for the fabrication of elongated microsized objects from solution by means of molecular self-organisation. Self-organisation occurs because molecules interact with each other and form structures driven by their intrinsic properties. Very often these processes are biomimetic, i.e. they are copied from nature. This is the case for the FF, as it is a natural compound that belongs to the class of peptides, structures formed by amino acids, consisting of two or more blocks connected to each other by peptide bonds. The optical response of this molecule is located in the UV range and originates from the benzene rings.

DPFO is a synthetic organic compound which belongs to the low-weight intramolecular charge-transfer (ICT) molecules. This type of molecules can be divided in electron donor, electron acceptor and the π-conjugation bridge, which connects these parts of the molecule. Such a molecular structure allows ICT molecules to demonstrate optical activity in the visible range. The structure of DPFO itself results in the observation of optical response in the green part of the spectral region.

This chapter will give an introduction to the basics of the self-organisation process and some structural properties which influence the optical response. The molecular structure, the fabrication process, as well as the structural features of self-organized structures for both of the molecules will be discussed here.

1.1.1 Self-assembly - an introduction

Self-assembly (SA) is a well-known bottom-up approach used for nano- and micro object fabrication. This technique uses chemical and physical forces on the nanoscale level as well as interactions with the substrate and solvent to assemble atoms or molecules into larger ordered structures [5].

SA is used in biological systems which exploit the SA approach to create their own parts: lipid membranes [6], protein aggregates or in artificial complex objects like molecular machines [7; 8]. Utilisation of the SA principles gives the opportunity to simply construct objects for modern technology: sensors, transistors, data propagation, synthesises, drug delivery and many others [9].

As components for SA one can use single molecules, groups of molecules or segments of macromolecules. Interactions of building-blocks with each other force them to go from a disordered state into a molecular crystal or folded macromolecule(fig. 1.1). These interactions are usually weak but are represented as a combination of many

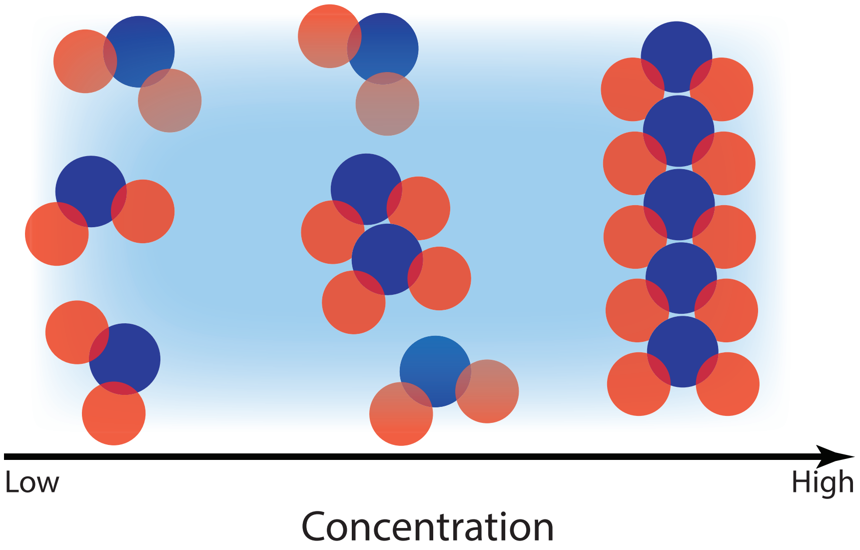

Figure 1.1: Schematic representation of self-assembly process. At low concentrations building blocks (molecules) freely move in the solvent with interactions. At increased concentration objects can attach to each other to form small aggregates. At high concentration interactions become stronger and the molecules form bigger and stable aggregates.

different non-covalent interactions. They include hydrogen bonding, electrostatic and van der Waals interactions, hydrophobic interactions and aromatic stacking interactions. The latter is important for the case of the amyloid proteins self-assembly [10]. The weakness of the interaction allows molecules to adjust and optimize their position in the aggregates. The SA process usually occurs in a solution at an interface in order to achieve some freedom in motion and to give mobility to the molecules. If the intermolecular interaction of the building blocks is not so strong as hydrogen bonds or π-π interaction, the SA can be stimulated with the help of external fields [11].

1.1.2 Alignment of the SA structures

While the control over structure size and morphology can be achieved via concentration, solvent or substrate patterning, very often the process of SA results in an array of nano- and microstructures randomly distributed over the surface of the substrate. This is not suitable for many real applications, hence approaches to the manipulation and control of the alignment of the SA structures have been developed. Alignment and arrangement can be performed on the larger scale and also with individual objects.

Well-known example of an aligning technique can be found in such a device as a liquid crystal display (LCD). A LCD consist of pixels containing liquid crystal (LC) molecules which are aligned along one direction. A usual technique to do that is rubbing of the substrate (fig. 1.2(a)). A pattern of parallel grooves is created on the surface of the substrate which forces the LC molecules to align in the desired way [12].

A LC by itself can also be used for aligning molecules as a guiding matrix (fig. 1.2(b)). They force the embedded “guest” molecules to align along the direction of the “host”. This results in the self-assembly of fibrous structures inside a LC, the obtained

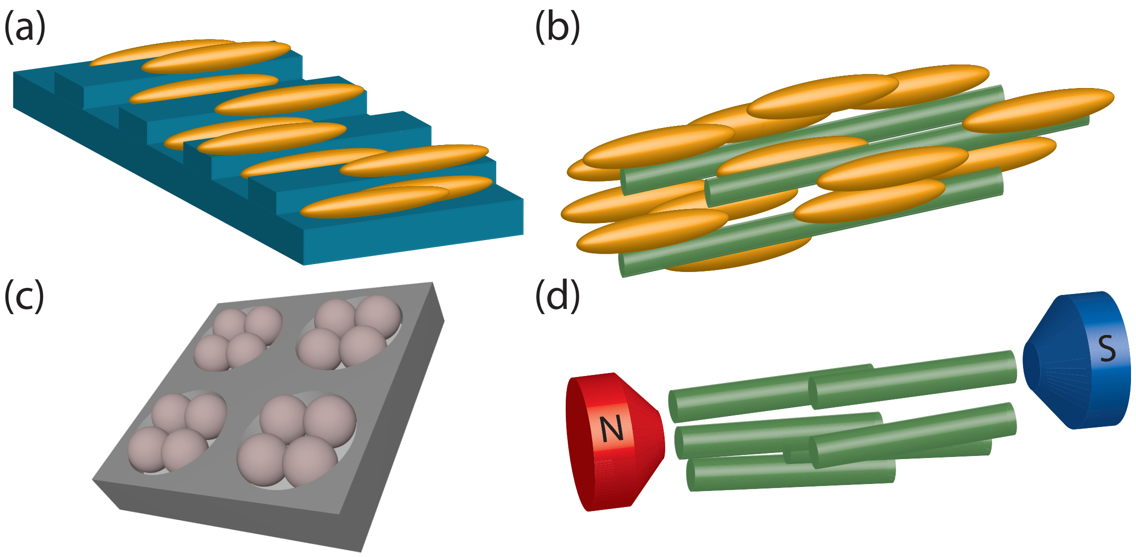

Figure 1.2: Several approaches used to align microobjects by means of external influence: (a) rubbing of the the substrates makes LC molecules to align along rubbing direction; (b) alignment of one type of molecules (green cylinders) in the matrix of the other one(yellow ellipsoids); (c) 2D matrix of holes filled with spherical particles; (d) use of external magnetic field to align microobjects.

structure is called a liquid-crystalline physical gel [13; 14]. However, both LC and “guest” molecules should be compatible with each other, the presence of a LC matrix can disturb the SA process, and also the presence of the LC is not always desirable, due to the fact that separation of LC and aligned nanostructures can be difficult.

The template assisted SA is a technique used to direct molecules or micro- and nanoobjects to arrange according to the pattern of the template [15] (fig.1.2(c)). Porous membrane materials (like anodised aluminium oxide, silica, etc.) can be used as templates for alignment of silicon microspheres inside the pores via capillary forces. Control over the ratio between pore diameter and sphere size allows to obtain different configurations of the spheres inside the hole.

A further aligning approach uses electric fields [16]. A technique called dielectrophoresis (DEP) was used to separate individual diphenylalanine peptide tubes and to place them between electrodes in order to investigate their electrical properties. This technique is based on the fact that an external electric field can cause a charge redistribution on the surface of the object, aligning this charged object by the external field.

If the material demonstrates ferromagnetic properties or magnetic anisotropy, a magnetic field can be used for alignment (fig. 1.2(d)). In the opposite case: the self assembling material has no or very weak magnetic properties, ferromagnetic particles (e.g. Fe_2O_3) can be attached to such objects. When the structure should not be disturbed by attaching other objects but still have weak magnetic response, very high magnetic fields are exploited for alignment, as was shown for such organic materials as cyanine dye molecules [17] or peptide amphiphile nanofibers [18].

All aforementioned approaches work mostly with an ensemble of objects, while,

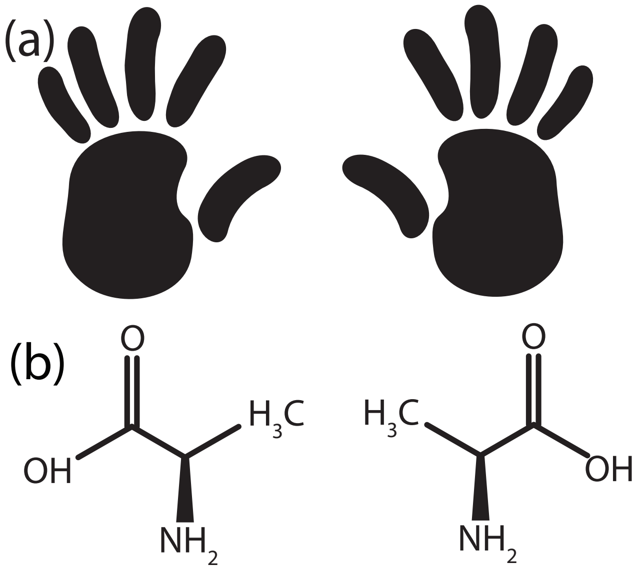

Figure 1.3: Enatiomorphs. a) Human hands as an example of enatiomorphic shapes. b) Enatiomeric amino acids: L-alanine and D-alanine, the geometry of one is the mirror reflection of another.

when utilizing the scanning probe microscopy approach or optical tweezers, individual atomic or molecular objects can be trapped and relocated to a desired place [19; 20].

1.1.3 Chirality

Chirality is a structural property that influence the physical properties of materials. The word derives from the Greek word "$\chi\epsilon\iota\rho$" meaning hand and actually describes the handedness of the object. This propriety is equivalent to the lack of mirror planes in the structure, i.e. mirror reflections of the object do not coincide with each other (fig. 1.3(a)). Objects demonstrating chirality are called "enatiomorphs", or "enatiomers" when speaking about molecules. Despite the fact that it cost the same energy to produce both forms of enatiomeric molecules in an achiral environment, living organisms consist of substances which are chiral. As an example, most of the important amino acids in nature have the same handedness (fig. 1.3(b)).

From an optical point of view, chiral molecules are interesting as they display differences in the interaction with left- and right- handed circularly polarized light, depending on their own handedness. For linear optics, this results in circular-dichroism (CD), caused by different absorption, or optical rotation (OR) due to the different refractive indices and therefore phase retardation between the left- and right-handed circular components. These effects can be used for determination of the enantiomeric purity, i.e. the ratio of both types of molecules in a solvent, the structure of the proteins and DNA, and the configuration of chiral molecules [21; 22].

Chiral properties can be observed in structures without molecular chirality. An

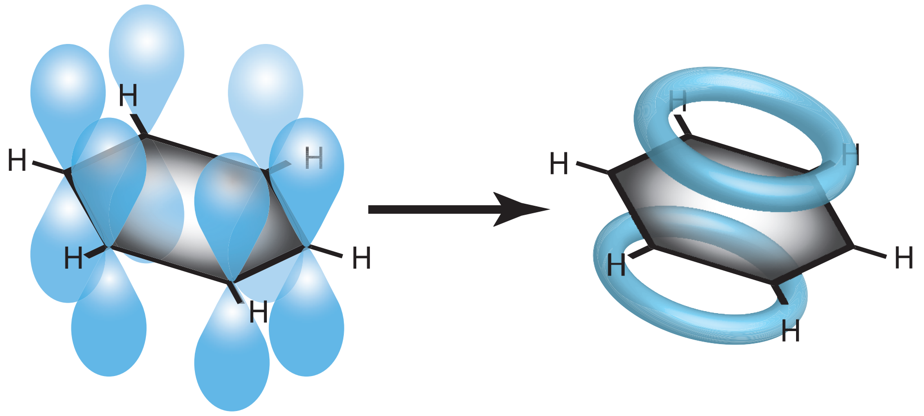

Figure 1.4: Configuration of π electrons in a benzene molecule. Intersection of π-orbitals (blue dumbbells) leads to delocalisation of corresponding electrons. All π-electrons become to be shared (blue rings) between carbon molecules of the benzene ring.

arrangement of atoms, e.g Au, in a geometry with pronounced chirality leads to the appearance of the optical sensitivity to the light handedness. Gammadion-shaped structures can generate a chiral evanescent field which can be exploited for biosensing applications [23]. An array of "L"-shaped nanostructures demonstrates increased chiral optical second harmonic response compared with measurements in linear optics. Higher order multipole nonlinear responses can play a significant role in such kind of systems [24–26].

1.1.4 The role of π-conjugation for optical properties

The appearance of π-conjugation can have a strong effect on the optical response of organic molecules. Conjugation is an arrangement type of connected p-orbitals in molecules with alternating single and double/triple bonds. In this case, the molecule has a region of overlapping p-orbitals, bridging the interjacent single bonds. This leads to the delocalisation of π-electrons across all the adjacent aligned p-orbitals in such molecules. The π-electrons do not belong to a single bond or atom, but rather to a group of atoms.

In general, conjugation helps to decrease the total energy of a molecule and increases its stability. A benzene ring is one of the simplest examples of a conjugated system which has 6 delocalised π-electrons (fig. 1.4).

This delocalisation of electrons strongly influences the absorption/emission properties of a molecule. Increase of the conjugated bond chain length leads to decrease of $\pi\pi^*$ state energy. So the longer the conjugated system is, the lower the energy of the photons interacting with this molecule and results in a red shift of the absorption and emission peaks of the molecule. This red shift can be seen in compounds which have an increasing number of fused benzene rings, e.g. in linearly fused aromatic molecules like benzene, naphtalene and anthracene (fig.1.5) and the emission is red shifted as well [27; 28]. The length of the conjugation (amount of alternating single and double bounds inside the molecule) also affects the quantum efficiency, for longer conjugation it is higher. This rule has a qualitative meaning as it also depends on the molecule planarity and the configuration of the conjugated bonds inside the molecule, as it causes changes of the delocalisation configuration.

Next, we will discuss both materials studied in this thesis in more detail and analyse synthesis and structure.

1.2 FF-peptide structures

FF peptide is a biological molecule which consist of two phenylalanine amino-acids connected to each other with a peptide bond (C(O)NH). Its properties have been intensively investigated because it is the core recognition motif of the β-amyloid polypeptide. Amyloid peptides form fibrils, which naturally occur in a human body during some brain diseases (e.g. Alzheimer disease and Parkinsons disease) [10]. In total there are about 20 human diseases which are associated with the formation of amyloid fibrils. In nature, amyloid fibrils are formed by polypeptides of 30-40 amino-acids, but even short structures like FF can form discrete and hollow nanostructures.

The solvent can influence the self-assembly process of FF molecules and result in the formation of different types of nanostructures. Nano- and microsized tubes can be obtained with the help of water based solvent (details of the fabrication procedure will be described in sec. 1.2.1).

Substitution of the water with 50% methanol subsequently leads to the formation of spherical peptide particles [31]. If the environment is again changed to aqueous, spheres transform to peptide tubes. In aqueous solution, water molecules support the hydrogen bonds arrangement, whereas in a methanol environment the hydrogen arrangement cannot be sustained, leading to different morphologies. The aromatic interaction of the peptide molecules make them self-assemble into spherical structures. The diameter of peptide spheres lies in the range of from 1 to 5 nm [32].

FF molecules can be also used as an intermediate step for further fabrication of nanostructures. Single crystalline, semiconducting nano-wires can be fabricated through a vapor transport process in which the linear form of FF is used as the initial material. Vaporisation of the FF at 250 °C, leads to transformation of the linear form to the cyclic form and the formation of nanowires [33]. The same process can be triggered with the help of chemical treatment of the diphenylalanine. Aldehyde addition can trigger the transformation of a linear peptide into the cyclic form and leads to self-assembly of this new building block into nanoribbons which form platelets with a length of hundreds of μm, a width of tens of μm and a thickness of hundreds of nm [34]. Another example of nanostructure fabrication uses FF tubes as “molds” for the synthesis of metallic nanowires with diameters of hundreds of nanometers. Ag ions were inserted into the hollow part of an FF-tube forming wire surrounded by FF-molecules, whereafter an enzyme was used for degradation of the peptide cladding to make Ag nanowires [35]. These Ag nanowires can be used in nanophotonics and nanoelectronics.

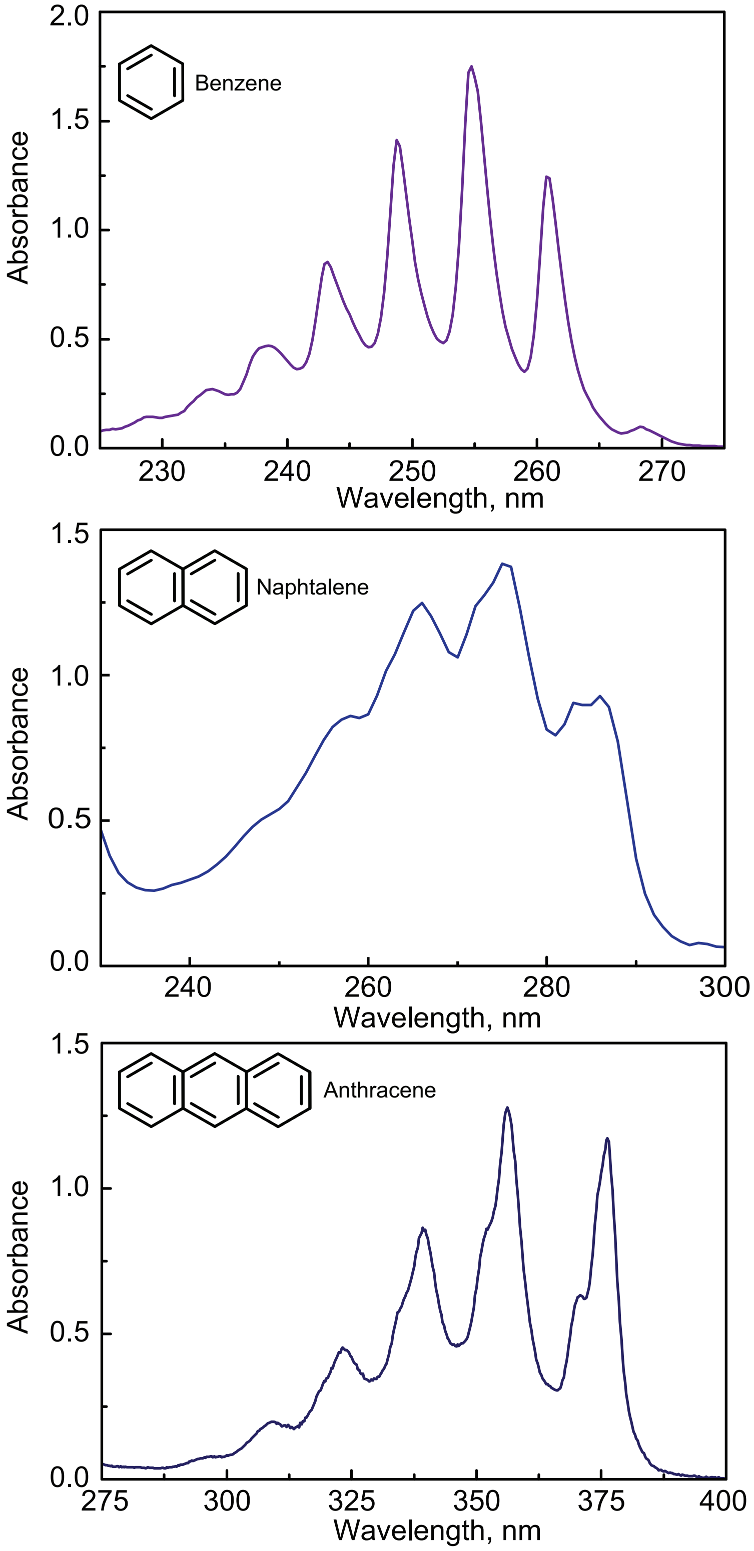

Figure 1.5: Influence of conjugation on the optical properties in linearly fused aromatic molecules like benzene, naphtalene and anthracene. Longer conjugation leads to a red-shift of the absorbance. Spectra were obtained via PhotochemCAD software [29; 30].

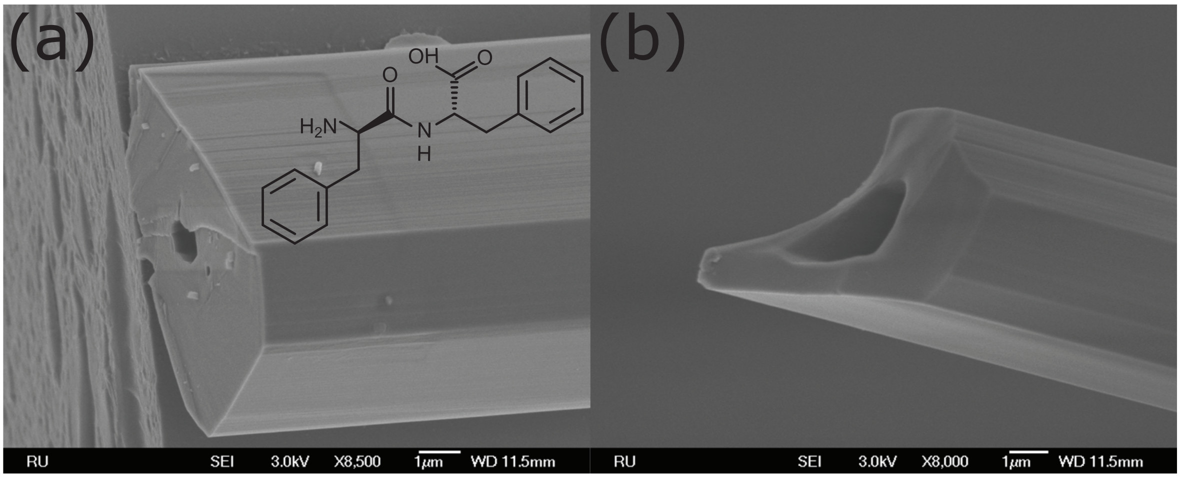

Figure 1.6: Typical SEM image of a peptide microtube edge; (a) Tube with channel diameter approx. 500 nm; (b) Tube with channel diameter approximately 1500 nm.

1.2.1 Self-assembly of FF tubes in water solution

Preparation of FF tubes from water solution is one of the simplest and most popular methods [32; 36; 37]. The standard procedure involves dissolution of FF-dimers in 1,1,1,3,3,3-hexafluoro-2-propanol (HFP) up to a concentration of 100 mg/ml as the first step. This highly concentrated solution can be dropcasted on a cleaned substrate in order to obtain a very dense vertically aligned (perpendicular to the substrate) arrangement of short peptide nanotubes. The second step includes further dilution of the stock solution in water to concentrations less than 5 mg/ml. This results in the formation of horizontally aligned tubes (laying parallel to the surface of the substrate). The water solution in this case is dropcasted on the substrate until the water is evaporated.

For the studies performed in this thesis, we have used horizontally aligned tubes as it more convenient for studies of individual objects. In order to obtain the density that is optimal for our optical studies we used concentrations of 0.2 -0.5 mg/ml. The tube arrangement on the surface after solvent evaporation usually has a circular shape following the shape of the solution droplet. After the sample fabrication, the tubes on the glass substrate are randomly oriented. Vertical tubes have diameters up to 1 μm and lengths up to 100 μm. Sizes of the horizontal tubes vary from 100 nm to 10 μm, their length can reach up to 1 mm. Diameters of the tube channel can vary from tube to tube, their position can also be shifted from the geometrical center (fig.1.6).

On a microscopic scale, peptide tubes demonstrate a relatively complex structure [38]. The FF molecules form head-to-tail chains by means of hydrogen bonds (fig.1.7).

The peptide chain is arranged in a coil-like structure with a hexagonal cross-section (fig.1.8). The diameter of the structure is about 2.4 nm. However, unlike usual spring coils, the turns of peptide structures interact with each other via hydrogen bonds. FF molecules are arranged in such a way that their aromatic rings point outside. This causes several coils to connect to each other due to the interaction of the aromatic rings. The array of parallel coils form the final object: peptide nano/microtube. One can distinguish two types of "channels": one belongs to the molecular arrangement of

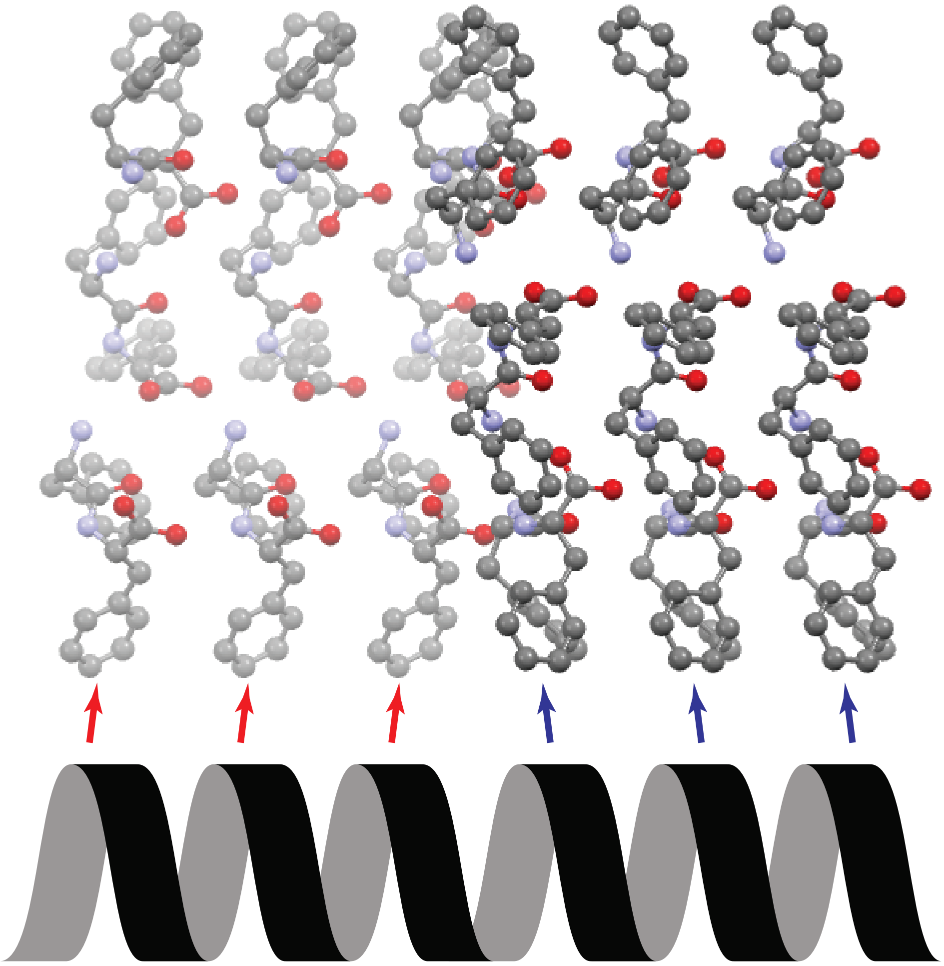

Figure 1.7: Coil-like structure of the FF molecules inside the individual peptide tube, red arrows correspond to the directions of the molecule arrangement at the backside of the coil, blue arrows show the direction for the frontside.

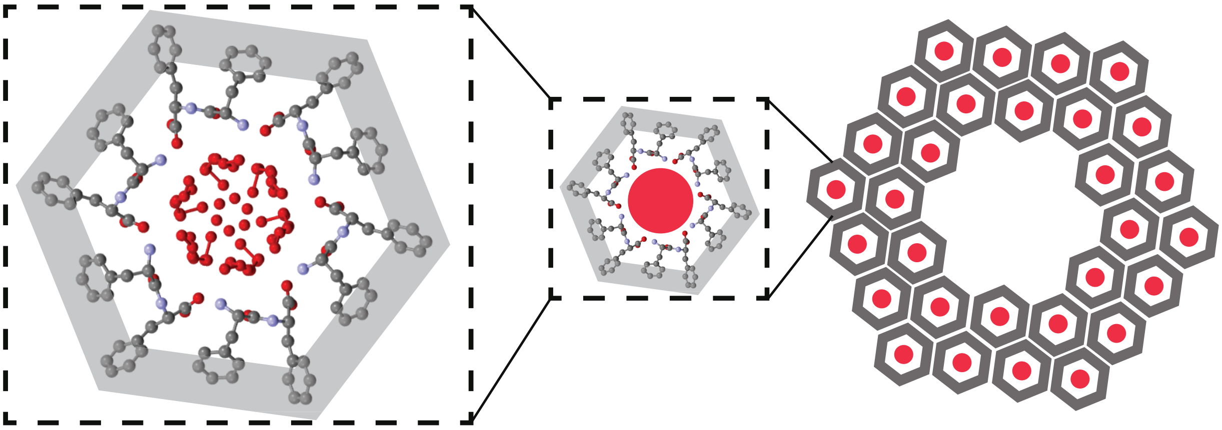

Figure 1.8: Hexagonal arrangement of six FF-molecules with water molecules inside (depicted with red spheres and sticks). By means of hydrogen bonds hexagonal coils attach to each other into the final FF tube. Note the channel of hexagonal arrangement is filled with water (red circles), but the central channel of FF-tube is empty.

FF and contains water molecules; another through the central part of the tube and contains air.

The micro-structure of the FF tubes can be divided into two significant regions: an aromatic zone which is organized by aromatic-aromatic interactions (a hydrophobic zone) and the internal channels formed by hydrogen bonding in which they store water molecules (a hydrophilic zone) [39]. Despite the fact that water molecules are weakly bonded to FF molecules in the peptide tube and can not move freely, they can evaporate from the channels . It was also reported that evaporation of the water is a possibly complex process and includes evaporation of weakly bonded water and more strongly bonded “crystalline” water [37].

It is important to note, that the presence of the water molecules is significant for the structure of the FF mircotubes (FFMT’s) and its physical properties [40]. The water molecules are responsible for the arrangement of the FF molecules in a hexagonal shape.

The part of the coil consisting of the 6 FF molecules and the water molecules can be defined as a “supercell” (fig. 1.8) [41]. We will use this term later for the explanations of the observed effects.

It was shown that the aforementioned synthesis procedure can be simplified by excluding the HFP. The procedure involves heating of the water solution for better dissolution of the peptide powder [42]. The peptide powder was dissolved in Nanopure water at 65°C, stabilized at this temperature for 30 min and then gradually cooled to room temperature.

The described self-assembly from water solution allows simple modifications of the optical properties of the final structure by adding various dyes (e.g. Nile Red) [43], ions and different photosynthesizers [44], magnetic [45] and noble metal nano-particles [42; 46; 47].

1.2.2 Physical properties

FF peptide molecules form crystal structures with a tubular shape. X-ray and electron diffraction studies show that the crystal structure at room temperature can be attributed to the $P6_1$ space group [38]. As such, many physical phenomena described by an odd-rank tensor are allowed: the linear electro-optic effect, piezoelectricity, ferroelectricity and optical second harmonic generation (SHG).

Peptide tubes show a strong piezoelectric response, with a value of the effective longitudinal piezoelectric coefficient d_{33} of about 30 pm/V, which is higher than for the well-known inorganic piezoelectric crystal $LiNbO_3$ [36]. Partial switching of polarisation was also demonstrated under an applied external field in the range of 100-200 kV/cm.

Investigation of the ferroelectric properties of peptide nanotubes resulted in the observation of light induced changes of the hysteresis loop shape, which is a direct consequence of changes in the spontaneous polarisation [48].

Charge transport in the peptide tubes was calculated with the fragment orbital method [49]. According to the calculation, electron transport is more preferable than hole transport in the linear form of the FF-peptide. The calculated bandgap is equal to 5.59 eV, which is in the range of energy gaps observed for boron nitride nanotubes (5.8-5.9 eV) [50]. These results indicate the similarity of the physical properties of the peptide tubes with conventional inorganic ones.

The amount of water molecules present in the crystalline structure of FF-tubes affect their structural and physical properties. A self-consistent charge density functional-based tight-binding method was used to calculate these changes [51]. Calculations were performed for the tubes with different amounts of water molecules: from no water present in the structure to 24 water molecules per “supercell”. For the case for water-free structures negative charges were distributed near carboxylate groups while positive charges near the NH_3 groups. Such a charge separation leads to the formation of a large crystalline dipole moment of 88.32 Debye along the nanotube axis. Introduction of the water molecules into the FF structure led to the growth of the channel size from 11.75 to 13.10 Å. Water molecules tend to align their dipole moment along the FF tubes which results in an increase of the total dipole moment of the building block by 3%.

1.2.3 Phase transition

Applications of the self-assembled materials demand the studies of their behaviour in different environmental conditions: stability at low/high temperatures and pressure. The investigation of the FFMT’s temperature stability revealed that increase of the temperature causes a phase transition. Two processes were reported to be related to the phase transition: one related to the water evaporation from the tubes, another to a molecular transformation.

Let us look at both processes in more detail. The first possible mechanism of a phase transition is based on the fact that during the heating process water molecules evaporate from the channel formed by FF molecules (“supercell”), which causes a

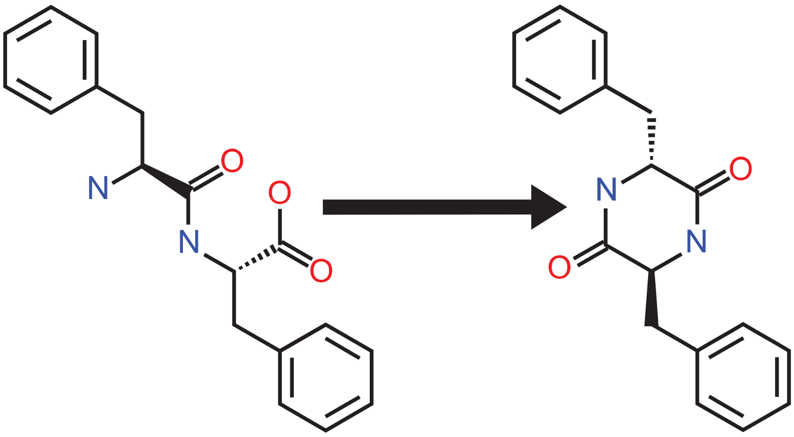

Figure 1.9: Molecular transformation from the linear form of the FF molecule to the cyclic one (DKP). Central part of molecule changed due to the removal of nitrogen and hydrogen atoms.

deformation of the crystal structure. A similar effect of crystal lattice change by water evaporation was observed in L-aspartyl-L-phenylalanine methyl ester, also known as aspartame [52]. This evaporation of water is reversible if the FFMTs are held in an environment with high humidity and pressure, water molecules can return back inside a “supercell” [41].

The second process is related to the molecular transformation. Increase of the temperature leads to a modification of the molecule from its linear form to the cyclic form of peptide which belongs to the group of diketopiperazines (DKP) (see fig. 1.9). Diphenylalanine molecules lose hydrogen and oxygen atoms due to the merger of the terminal carboxylic acid and amine group and form the 2,5-diketopiperazine molecule (see Fig. 1.9). This scenario is irreversible and occurs at higher temperature ranges compared to evaporation of molecules from the “supercell”.

Presence of both steps in the phase transition have been seen by several techniques like differential scanning calorimetry (DSC) and nuclear magnetic resonance (NMR) [37] and modification of the piezoelectric properties of individual FFMTs [53].

The water evaporation from the “supercell” due to the temperature treatment influences the optical properties of the peptide microtubes. It causes changes in the UV spectra of self-assembled peptide structures [41]. The change in the amount of H_2O molecules inside the channel leads to a modification of the “supercell” geometry and size, resulting in changes of the density of the states, which can be observed as a shift of the UV photoluminescence peak (fig. 1.10). Subsequent heating and water vapour treatment cause a blue and red shift; respectively, showing a clear reversibility of the process and an influence of the amount of water inside the tube.

The temperature treatment influences not only the position of the UV luminescence but also its lifetime (at 282 nm) as inelastic scattering of excitons by phonons decreases the exciton lifetime [54]. This process reduces the radiative state population and consequent emission, resulting in a reduction of the luminescence lifetime from 10 ns to 1 ns after heating from room temperature to 60 °C.

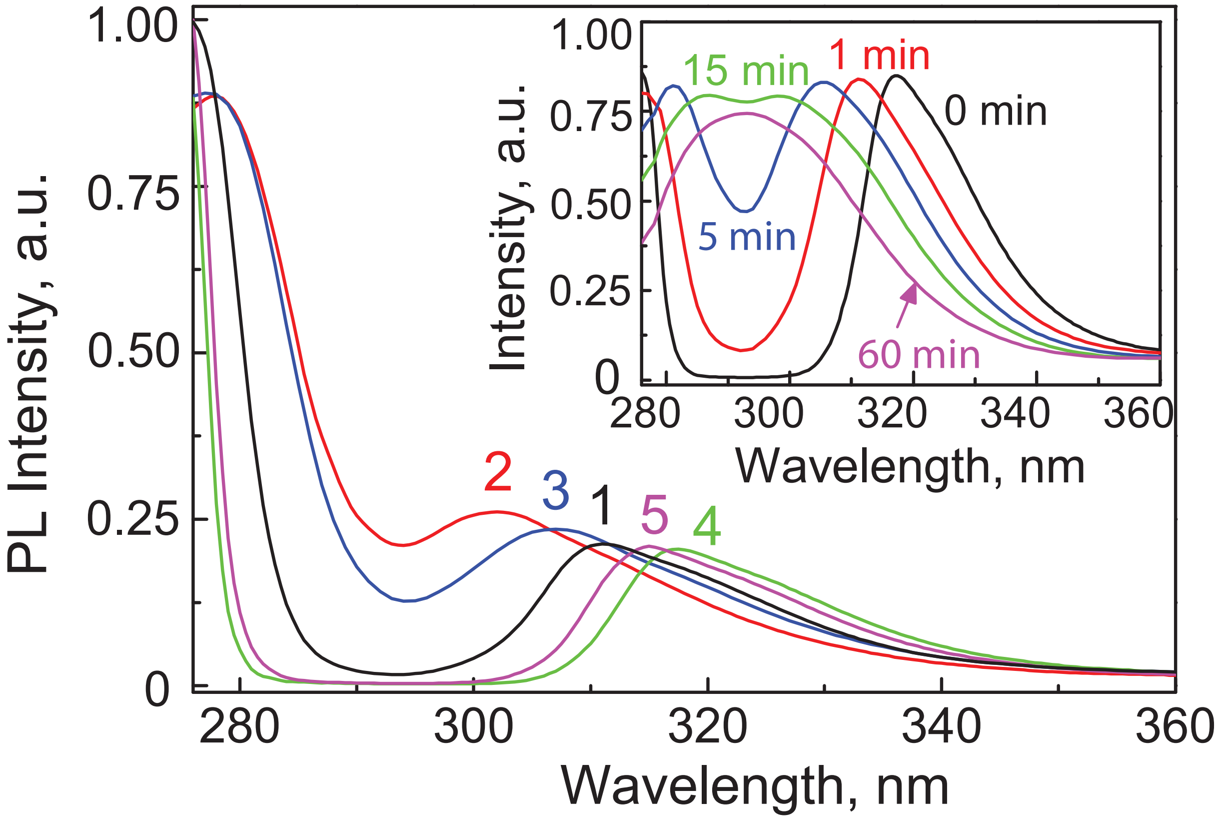

Figure 1.10: Photoluminescence spectra of the initial FFMT samples fabricated using an FF concentration of 120 mg/mL at the relative humidity value of 100% and 22°C after different post-processing procedures. Curve 1: as-fabricated; curve 2: dried at 90°C for 16 h and then exposed to saturated water vapor at 90°C for 16 h (curve 3); curve 4: exposed to saturated water vapour at 90°C for 16 h and then dried at 90°C for 16 h (curve 5). The inset displays the photoluminescence spectra obtained from the FFMT sample fabricated using an FF concentration of 160 mg/mL at the relative humidity value of 100% and 22°C for 0, 1, 5, 15, and 60 min by 256 nm UV irradiation. Reprinted with permission from ref. [41]. Copyright 2011 WILEY-VCH

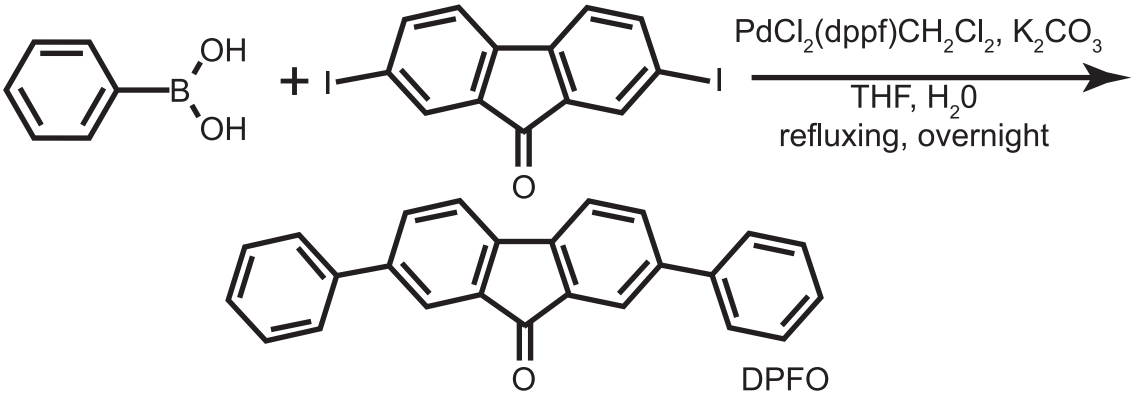

Figure 1.11: Synthesis procedure of the DPFO molecule.

1.3 DPFO microfibres

2,7-diphenyl-9H-fluoren-9-one (DPFO) is an organic molecule based on a fluorenone core with two benzene rings attached via single bonds. It belongs to the class of organic molecules with intramolecular charge transfer (ICT). These compounds often have an electron donor (D) and an electron acceptor (A) part connected to each other by a π-bridge. These compounds have fascinating applications for designing new materials, such as nonlinear optical (NLO) materials, fluorescence probes, and dye-sensitized solar cells [55–57]. This makes low molecular weight D - A-substituted ICT compounds good candidates for the building blocks of hierarchically structured and multifunctional supramolecular self-assemblies and allows the fabrication of well-formed and morphology-controllable architectures with desirable sizes, shapes, and functions [58; 59].

1.3.1 Sample fabrication of DPFO fibres

In contrast to the FF molecule, DPFO is a relatively new material as the molecule was synthesized quite recently [60]. Before we go to the description of the sample fabrication, some information about the molecular synthesis should therefore be presented. Synthesis of DPFO molecules requires a palladium catalysed Suzuki coupling between phenylboronic acid and 2,7-diiodo-9H-fluoren-9-one [61]. Under a nitrogen atmosphere, to a stirred mixture of phenylboronic acid (244 mg, 2.0 mmol) and 2,7-diiodo-9H-fluoren-9-one (432 mg, 1 mmol) in 20 mL of THF and 6 mL of 2 M K_2CO_3 solution in water was added $PdCl_2(dppf)CH_2Cl_2$ (50 mg, 0.06 mmol)(fig. 1.11). The reaction mixture was refluxed overnight. After cooling and removing most of the solvent in vacuum, the mixture was dissolved in 300 mL of CH_2Cl_2, the organic phase was washed with water (50 mL) and dried over Na_2SO_4. The product was purified by column chromatography (silica gel, petrol ether : dichloromethane = 5 : 1) resulting in the fabrication of 260 mg of yellow needle-like crystals with a yield of 78%. This process allows to obtain the stock compound which should be further processed to obtain microstructures.

Self-assembled samples investigated in this thesis were made by the following technique. 10 mg of DPFO powder were mixed with 25 mL of heptane and heated into refluxing to make a saturated solution. Upon slowly cooling to room temperature (2 °C/min) and stabilizing overnight, the compound precipitated as microfibres [60]. Their width ranges from tens to hundreds of microns and the length can reach several millimetres. The shape and size of the microfibres could easily be tuned by changing the concentration of the refluxing solution. A solution with the formed DPFO microstructures was deposited on the glass and silicon substrates. After evaporation of the solvent, the surface of the substrate was covered with randomly oriented DPFO microfibres.

1.3.2 DPFO structure

In order to investigate the single crystalline properties of DPFO structures high quality bulk single crystals of DPFO were fabricated by slowly evaporating a saturated $CHCl_3$ solution at room temperature. Single crystal X-ray diffraction (XRD) analysis (Rigaku Saturn X- ray diffractometer) showed that the V-shaped DPFO molecules are organized in a non-centrosymmetric orthorhombic ($Ccm2_1$) space group with the two side phenyl planes twisted from the fluorenone plane by 36.4°, both in the same direction(fig. 1.12(a),(b))[60]. The $C = O \cdots H$ hydrogen bonds drive the formation of molecular chains along the c-axis , and aromatic $CH \cdots \pi$ interactions attach these hydrogen bonded molecular chains in the second dimension along the a-axis to form the 2-D lamellar structure [62]. Scanning electron microscope (SEM) studies revealed the crystal's 1D microfibre morphology, with widths ranging from several to tens of micrometers and lengths up to several millimetres(fig. 1.12(c)).

Atomic force microscopy (AFM) imaging showed that these fibre were very thin in the third dimension (thickness to width aspect ratio around 1:10 and roughness of R_{max}=18.45+9.94 nm (fig. 1.13(a)). The single crystal character of the DPFO fibres was confirmed by transmission electron microscopy (TEM)(fig. 1.12(c)) and the corresponding selected-area electron diffraction (SAED) patterns (fig. 1.12(d)), which were indexed with the bulk crystal lattice constants and suggested that the microfibres grow along the [001] direction.

Powder XRD of the microfibres revealed that the thin axis of the microfibre perpendicular to the substrate was the b-axis. The growth rates of DPFO molecules are dominated by the nonconvalent interactions between DPFO molecules along the different crystallographic axes which results in these thin and long microfibres. Since the long axis of the microfibres is the crystallographic c-axis, and the permanent dipoles of the molecules are also directed along this direction, it is noteworthy that the molecular dipoles coherently contribute to the macroscopic permanent dipole moment of the microfibre. The existence of a dipole moment is important for NLO as it implies a noncentrosymmetric space group necessary for SHG, and it can significantly increase the second-order nonlinearity [63].

Powder XRD analysis provided another evidence that these fibres were having the same crystal phase as their single crystals because all the peaks in the XRD pattern taken from the as-grown microfibres could be indexed by comparing them with the

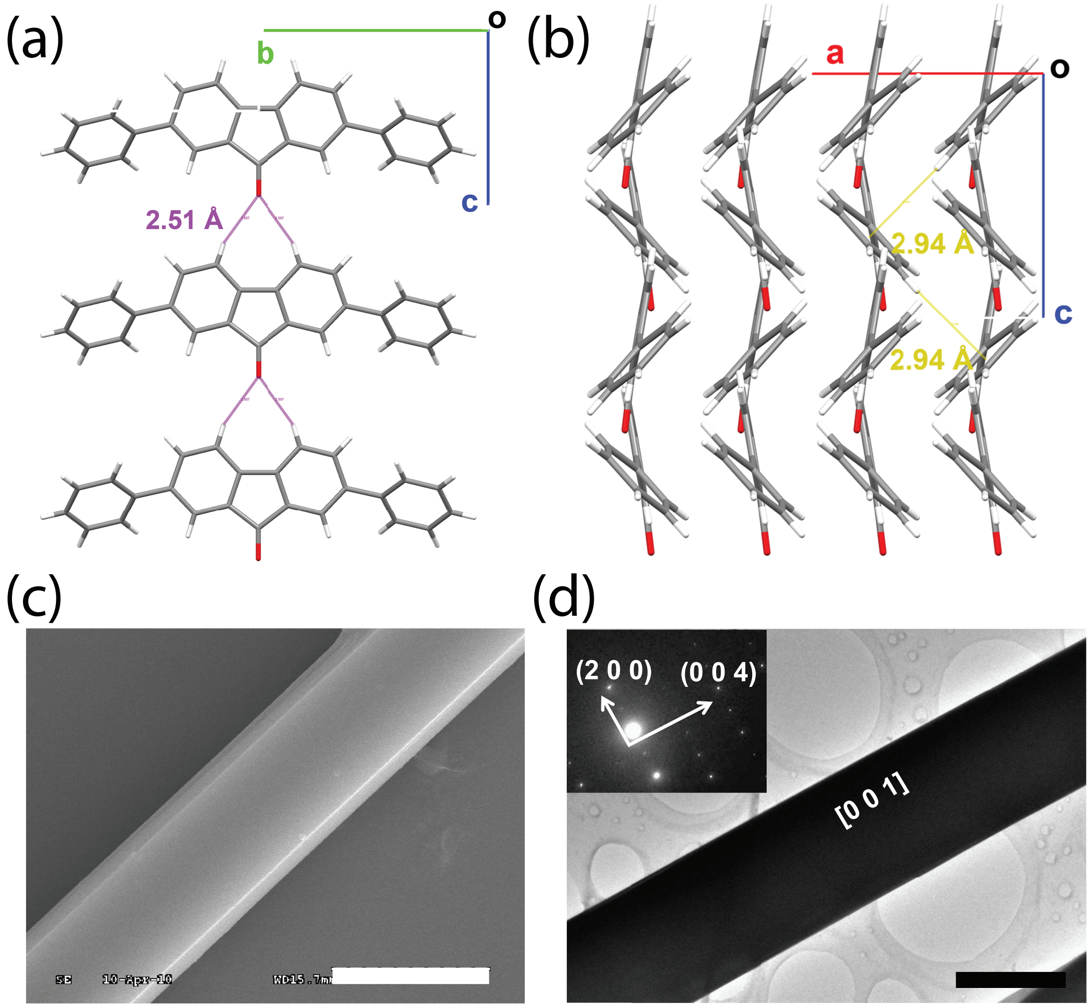

Figure 1.12: (a) Molecular packing of the DPFO molecules in b-c plane; (b) Molecular packing of the DPFO molecules in a-c plane; (c) SEM image of a typical self-assembled DPFO microfibre; (d) TEM image and its corresponding selected area electron diffraction (SAED) pattern of a DPFO microfibre (inset). Scale bars in left and right bottom images are 10 μm.

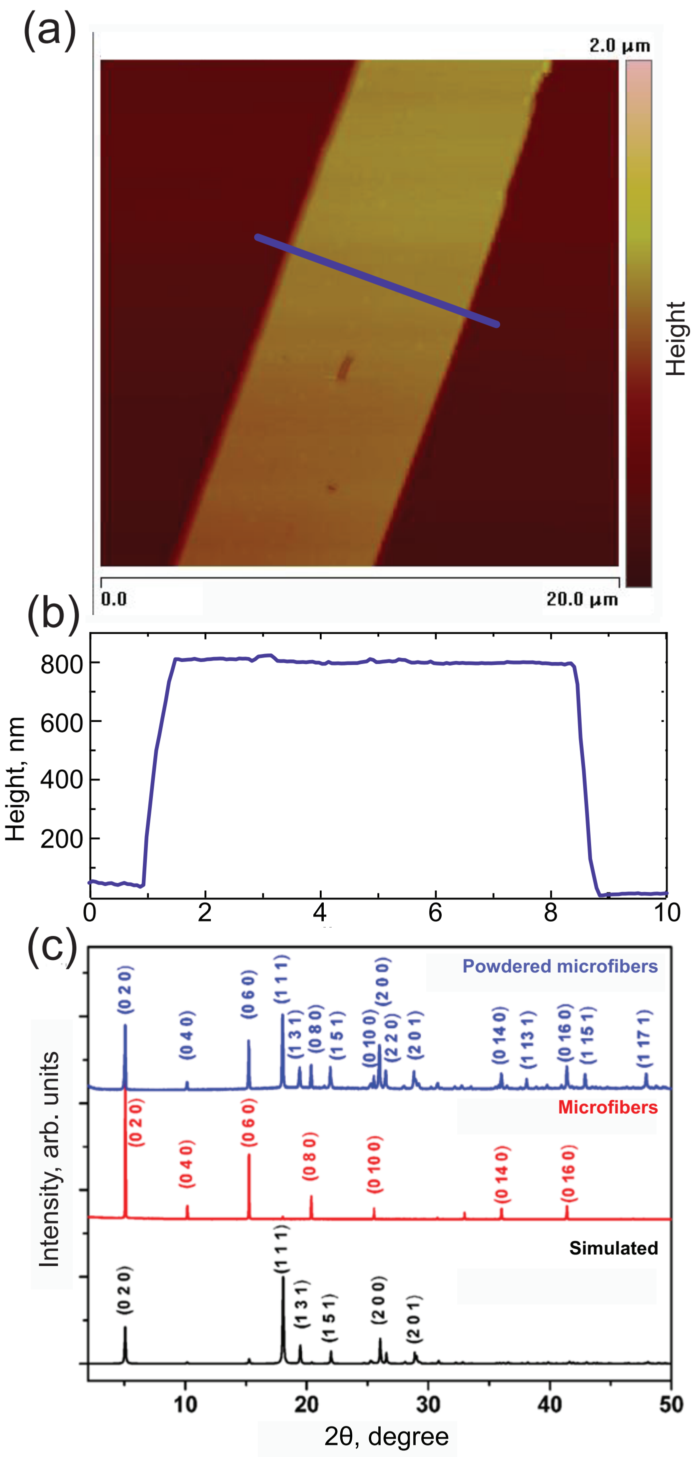

Figure 1.13: Topography of DPFO microfibre obtained by AFM microscopy. Size of image is 20 x 20 μm; b) Height profile ; c) XRD patterns of DPFO after grinding into a powder (blue), as-prepared microfibres(red) and simulated pattern (black).

powder XRD pattern simulated from the single crystal structures1.13. However, all of these peaks were indexed as (0 2 0), (0 4 0), (0 6 0), (0 8 0), (0 10 0), (0 12 0), and etc., which were all crystal faces from only the b-axis.

This can be attributed to the particular morphology of the microfibres, that grow extremely slow in the b-axis direction, such that the resulting fibres are very thin in the direction of the b-axis and the corresponding crystal face was the face having the biggest area.

Not only crystal faces from the b-axis, but also crystal faces in other directions like (1 1 1), gave diffraction peaks (fig. 1.13). After grinding into powder, each face had the same probability to be parallel to the substrate and give a diffraction pattern. The particular growing tendency of DPFO molecules to form into thin (in b-axis) and long (through c-axis) fibres was dominated by the interactions between the DPFO molecules. This agreed perfectly well with the simulated results about the preferences of the molecular expansions in different directions. The most preferred growing direction of the crystal was along the c-axis ("along the dipole"), while the least preferred direction was along the b-axis ("along the molecule"). This particular growth tendency made each fire highly polar with an intrinsic permanent dipole moment from one end of the fibre to the other.

The preferential growth of DPFO single crystals has been modelled using the Morphology module of the Materials Studio package with the Compass force field. To determine the relative importance of the different crystallographic faces, the attachment energy (E_{att}) was computed for a crystal face (hkl), which is defined as the energy per mol of molecule released when a new layer having thickness d_{hkl} is attached to the surface of the crystal. Attachment energy is a measure of the growth rate normal to a surface, so that faces that have higher attachment energy grow faster and have lower morphological importance.

Based on the calculated attachment energies, one can expect that the DPFO crystal first grows in the c-axis ("along the dipole") direction due to the strong $C - C \cdots O$ bonds formed in this direction. Then the π-stacking together with $C - C \cdots \pi$ interactions should promote the extension along the a-axis ("along the stack"). Finally the growth along the b-axis direction ("along molecule") is governed by weaker non-bonding interactions between the side phenyls of the DPFO molecules and yields the smallest attachment energies. The calculations confirm the X-ray measurements that for 1-D fibers the kinetic growth proceeds "along the dipole", namely a 1-D extension along the c-axis direction. 2-D crystals involve mostly growth in the a-c crystallographic plane.

1.4 Conclusions

Organic materials investigated in this thesis possess a noncentrosymmetric arrangement of molecules due to self-organisation, resulting in nonlinear optical properties as well as an elongated shape of both materials, that may allow the observation of waveguiding effects in them.

First, the arrangement of the conjugation of the DPFO molecule allows to observe linear optical effects in the visible range. The optical response from the FF structure originates from relatively short conjugation of benzene rings, lies in UV range and is rather weak.

Second, both of them self-assemble in microsized objects with clearly defined crystal structures. Their dimension is in the range of several microns in width and height and can reach hundred of microns or even millimetres in length.

Third, the point group symmetry of both materials allows to observe a net dipole moment and nonlinear optical effects. Finally, the flexibility of the fabrication process of both materials and their organic nature allow easy modification of the structure morphology, their physical and optical properties.

From the structural studies it can be seen that NLO methods of characterisation are suitable for both materials and can give new information about the properties of the materials such as energy levels, and relaxation times. All the mentioned features of both materials together with the variety of their morphologies make the materials interesting and promising candidates for application in miniature photonic devices.

References

[1] J. Li, C.-H. Wen, S. Gauza, R. Lu, and S.-T. Wu, “Refractive indices of liquid crystals for display applications,” *J. Display Tech.*, vol. 1, pp. 51–61, Sept. 2005.

[2] B. Geffroy, P. le Roy, and C. Prat, “Organic light-emitting diode (OLED) technology: materials, devices and display technologies,” *Polym. Int.*, vol. 55, pp. 572–582, June 2006.

[3] G. S. He, L.-S. Tan, Q. Zheng, and P. N. Prasad, “Multiphoton absorbing materials: molecular designs, characterizations, and applications.,” *Chem. Rev.*, vol. 108, pp. 1245–330, Apr. 2008.

[4] J. E. Reeve, H. L. Anderson, and K. Clays, “Dyes for biological second harmonic generation imaging.,” *Phys. Chem. Chem. Phys.*, vol. 12, pp. 13484–98, Nov. 2010.

[5] G. M. Whitesides and M. Boncheva, “Beyond molecules: self-assembly of mesoscopic and macroscopic components,” *Proc. Natl. Acad. Sci. U. S. A.*, vol. 99, pp. 4769–74, Apr. 2002.

[6] H. S. Kim, J. D. Hartgerink, and M. R. Ghadiri, “Oriented self-assembly of cyclic peptide nanotubes in lipid membranes,” *JACS*, vol. 120, pp. 4417–4424, May 1998.

[7] V. Balzani, M. Gómez-López, and J. F. Stoddart, “Molecular machines,” *Acc. Chem. Res.*, vol. 31, pp. 405–414, July 1998.

[8] M. M. Poranen, a. O. Paatero, R. Tuma, and D. H. Bamford, “Self-assembly of a viral molecular machine from purified protein and rna constituents,” *Mol. Cell*, vol. 7, pp. 845–54, Apr. 2001.

[9] E. Busseron, Y. Ruff, E. Moulin, and N. Giuseppone, “Supramolecular self-assemblies as functional nanomaterials,” *Nanoscale*, vol. 5, pp. 7098–140, Aug. 2013.

[10] E. Gazit, “A possible role for pi-stacking in the self-assembly of amyloid fibrils.,” *FASEB J.*, vol. 16, pp. 77–83, Jan. 2002.

[11] G. Sreenivasulu, M. Popov, R. Zhang, K. Sharma, C. Janes, a. Mukundan, and G. Srinivasan, “Magnetic field assisted self-assembly of ferrite-ferroelectric core-shell nanofibers and studies on magneto-electric interactions,” *Appl. Phys. Lett.*, vol. 104, p. 052910, Feb. 2014.

[12] J. Stöhr and M. Samant, “Liquid crystal alignment by rubbed polymer surfaces: a microscopic bond orientation model,” *J. Electron. Spectrosc. Relat. Phenom.*, vol. 98-99, pp. 189–207, Jan. 1999.

[13] T. Kato, Y. Hirai, S. Nakaso, and M. Moriyama, “Liquid-crystalline physical gels,” *Chem. Soc. Rev.*, vol. 36, pp. 1857–67, Dec. 2007.

[14] Y. Hirai, S. S. Babu, V. K. Praveen, T. Yasuda, A. Ajayaghosh, and T. Kato, “Anisotropic self-assembly of photoluminescent oligo(p -phenylenevinylene) derivatives in liquid crystals: An effective strategy for the macroscopic alignment of π -gels,” *Adv. Mat.*, vol. 21, pp. 4029–4033, Oct. 2009.

[15] Y. Xia, Y. Yin, Y. Lu, and J. McLellan, “Template-Assisted Self-Assembly of Spherical Colloids into Complex and Controllable Structures,” *Adv. Funct. Mater.*, vol. 13, pp. 907–918, Dec. 2003.

[16] J. Castillo, S. Tanzi, M. Dimaki, and W. Svendsen, “Manipulation of self-assembly amyloid peptide nanotubes by dielectrophoresis,” *Electrophoresis*, vol. 29, no. 24, pp. 5026–5032, 2008.

[17] I. O. Shklyarevskiy, M. I. Boamfa, P. C. M. Christianen, F. Touhari, H. van Kempen, G. Deroover, P. Callant, and J. C. Maan, “Magnetic field induced alignment of cyanine dye J-aggregates,” *J. Chem. Phys.*, vol. 116, no. 19, p. 8407, 2002.

[18] D. Löwik, I. Shklyarevskiy, L. Ruizendaal, P. Christianen, J. Maan, and J. van Hest, “A highly ordered material from magnetically aligned peptide amphiphile nanofiber assemblies,” *Adv. Mat.*, vol. 19, pp. 1191–1195, May 2007.

[19] J. Stroscio and D. Eigler, “Atomic and molecular manipulation with the scanning tunneling microscope,” *Science*, vol. 125, no. 1987, pp. 1319–1326, 1991.

[20] D. G. Grier, “A revolution in optical manipulation.,” *Nature*, vol. 424, pp. 810–6, Aug. 2003.

[21] S. M. Kelly, T. J. Jess, and N. C. Price, “How to study proteins by circular dichroism,” *Biochim. Biophys. Acta*, vol. 1751, pp. 119–39, Aug. 2005.

[22] S. Allenmark, “Induced circular dichroism by chiral molecular interaction,” *Chirality*, vol. 422, no. October 2002, pp. 409–422, 2003.

[23] E. Hendry, T. Carpy, J. Johnston, M. Popland, R. V. Mikhaylovskiy, a. J. Lapthorn, S. M. Kelly, L. D. Barron, N. Gadegaard, and M. Kadodwala, "Ultrasensitive detection and characterization of biomolecules using superchiral fields.," *Nat. Nanotechnol.*, vol. 5, pp. 783–7, Nov. 2010.

[24] B. K. Canfield, S. Kujala, K. Jefimovs, J. Turunen, and M. Kauranen, "Linear and nonlinear optical responses influenced by broken symmetry in an array of gold nanoparticles," *Opt. Express*, vol. 12, no. 22, p. 5418, 2004.

[25] S. Kujala, B. Canfield, M. Kauranen, Y. Svirko, and J. Turunen, "Multipole interference in the second-harmonic optical radiation from gold nanoparticles," *Phys. Rev. Lett.*, vol. 98, p. 167403, Apr. 2007.

[26] V. K. Valev, a. V. Silhanek, N. Verellen, W. Gillijns, P. Van Dorpe, O. a. Aktsipetrov, G. a. E. Vandenbosch, V. V. Moshchalkov, and T. Verbiest, "Asymmetric Optical Second-Harmonic Generation from Chiral G-Shaped Gold Nanostructures," *Phys. Rev. Lett.*, vol. 104, p. 127401, Mar. 2010.

[27] R. A. Friedel and M. Orchin, *Ultraviolet spectra of aromatic compounds.* New York,: Wiley, 1951.

[28] V. Gorelik and E. Zhabotinskii, "Two-photon-excited emission from solids," *J. Rus. Las. Res.*, vol. 16, no. 4, pp. 287–308, 1995.

[29] PhotochemCAD software. http://www.photochemcad.com/, 2014.

[30] H. Du, R.-C. A. Fuh, J. Li, L. A. Corkan, and J. S. Lindsey, "Photochemcad: A computer-aided design and research tool in photochemistry," *Photochem. Photobiol*, vol. 68, no. 2, pp. 141–142, 1998.

[31] N. Amdursky, M. Molotskii, E. Gazit, and G. Rosenman, "Elementary building blocks of self-assembled peptide nanotubes," *JACS*, vol. 132, pp. 15632–6, Nov. 2010.

[32] N. Amdursky, P. Beker, I. Koren, B. Bank-Srour, E. Mishina, S. Semin, T. Rasing, Y. Rosenberg, Z. Barkay, E. Gazit, and G. Rosenman, "Structural transition in peptide nanotubes," *Biomacromolecules*, vol. 12, pp. 1349–54, Apr. 2011.

[33] J. S. Lee, I. Yoon, J. Kim, H. Ihee, B. Kim, and C. B. Park, "Self-assembly of semiconducting photoluminescent peptide nanowires in the vapor phase," *Angew. Chem. Int. Ed.*, vol. 50, pp. 1164–7, Feb. 2011.

[34] X. Yan, Y. Su, J. Li, J. Früh, and H. Möhwald, "Uniaxially oriented peptide crystals for active optical waveguiding," *Angew. Chem. Int. Ed.*, vol. 50, pp. 11186–91, Nov. 2011.

[35] M. Reches and E. Gazit, "Casting metal nanowires within discrete self-assembled peptide nanotubes," *Science*, vol. 300, pp. 625–7, Apr. 2003.

[36] A. Heredia, I. Bdikin, S. Kopyl, E. Mishina, S. Semin, A. Sigov, K. German, V. Bystrov, J. Gracio, and A. L. Kholkin, "Temperature-driven phase transformation in self-assembled diphenylalanine peptide nanotubes," *J. Phys. D*, vol. 43, no. 46, 2010.

[37] M. Jaworska, A. Jeziorna, E. Drabik, and M. J. Potrzebowski, "Solid state nmr study of thermal processes in nanoassemblies formed by dipeptides," *J. of Phys. Chem. C*, vol. 116, no. 22, pp. 12330–12338, 2012.

[38] C. H. Görbitz, "Nanotube formation by hydrophobic dipeptides," *Chem. Eur. J.*, vol. 7, no. 23, pp. 5153–5159, 2001.

[39] C. H. Görbitz, "The structure of nanotubes formed by diphenylalanine, the core recognition motif of alzheimer's beta-amyloid polypeptide," *Chem. Comm.*, pp. 2332–4, June 2006.

[40] J. Kim, T. H. Han, Y.-I. Kim, J. S. Park, J. Choi, D. G. Churchill, S. O. Kim, and H. Ihee, "Role of water in directing diphenylalanine assembly into nanotubes and nanowires," *Adv. Mat.*, vol. 22, pp. 583–7, Feb. 2010.

[41] M. J. Wang, S. J. Xiong, X. L. Wu, and P. K. Chu, "Effects of water molecules on photoluminescence from hierarchical peptide nanotubes and water probing capability," *Small*, vol. 7, no. 19, pp. 2801–2807, 2011.

[42] Y. Song, S. R. Challa, C. J. Medforth, Y. Qiu, R. K. Watt, D. Pena, J. E. Miller, F. van Swol, and J. a. Shelnutt, "Synthesis of peptide-nanotube platinum-nanoparticle composites.," *Chem. Comm.*, pp. 1044–5, May 2004.

[43] X. Yan, J. Li, and H. Möhwald, "Self-assembly of hexagonal peptide microtubes and their optical waveguiding," *Adv. Mat.*, vol. 23, pp. 2796–801, July 2011.

[44] J. Ryu, S. Y. Lim, and C. B. Park, "Photoluminescent peptide nanotubes," *Adv. Mat.*, vol. 21, pp. 1577–1581, Apr. 2009.

[45] M. Reches and E. Gazit, "Controlled patterning of aligned self-assembled peptide nanotubes," *Nature Nanotechnol.*, vol. 1, pp. 195 –200, Dec. 2006.

[46] O. Carny, D. E. Shalev, and E. Gazit, "Fabrication of coaxial metal nanocables using a self-assembled peptide nanotube scaffold," *Nano Lett.*, vol. 6, pp. 1594–7, Aug. 2006.

[47] J. George and K. G. Thomas, "Surface plasmon coupled circular dichroism of au nanoparticles on peptide nanotubes," *JACS*, vol. 132, pp. 2502–3, Mar. 2010.

[48] Z. Gan, X. Wu, X. Zhu, and J. Shen, "Light-induced ferroelectricity in bioinspired self-assembled diphenylalanine nanotubes/microtubes," *Angew. Chem. Int. Ed.*, vol. 52, pp. 2055–9, Feb. 2013.

[49] N. Santhanamoorthi, P. Kolandaivel, L. Adler-Abramovich, E. Gazit, S. Filipek, S. Viswanathan, A. Strzelczyk, and V. Renugopalakrishnan, "Diphenylalanine peptide nanotube: charge transport, band gap and its relevance to potential biomedical applications," *Adv. Mat. Lett.*, vol. 2, no. 2, pp. 100–105, 2011.

[50] J. Yu, D. Yu, Y. Chen, H. Chen, M.-Y. Lin, B.-M. Cheng, J. Li, and W. Duan, "Narrowed bandgaps and stronger excitonic effects from small boron nitride nanotubes," *Chem. Phys. Lett.*, vol. 476, pp. 240–243, July 2009.

[51] T. Andrade-Filho, F. F. Ferreira, W. A. Alves, and A. R. Rocha, "The effects of water molecules on the electronic and structural properties of peptide nanotubes.," *Phys. Chem. Chem. Phys.*, vol. 15, pp. 7555–9, May 2013.

[52] C. Guguta, H. Meekes, and R. de Gelder, "The hydration/dehydration behavior of aspartame revisited," *J. Pharm. Biomed. Anal.*, vol. 46, pp. 617–24, Mar. 2008.

[53] I. Bdikin, V. Bystrov, I. Delgadillo, J. Gracio, S. Kopyl, M. Wojtas, E. Mishina, A. Sigov, and A. L. Kholkin, "Polarization switching and patterning in self-assembled peptide tubular structures," *J. Appl. Phys.*, vol. 111, no. 7, 2012.

[54] Z. Gan, X. Wu, J. Zhang, X. Zhu, and P. K. Chu, "In situ thermal imaging and absolute temperature monitoring by luminescent diphenylalanine nanotubes," *Biomacromolecules*, vol. 14, pp. 2112–6, June 2013.

[55] K. Schmidt, S. Barlow, A. Leclercq, E. Zojer, S.-H. Jang, S. R. Marder, A. K.-Y. Jen, and J.-L. Bredas, "Efficient acceptor groups for nlo chromophores: competing inductive and resonance contributions in heterocyclic acceptors derived from 2-dicyanomethylidene-3-cyano-4,5,5-trimethyl-2,5-dihydrofuran," *J. Mater. Chem.*, vol. 17, pp. 2944–2949, 2007.

[56] S. E.-D. H. Etaiw, T. A. Fayed, and N. Z. Saleh, "Photophysics of benzazole derived push-pull butadienes: A highly sensitive fluorescence probes," *J. Photochem. Photobiol. A*, vol. 177, no. 2?3, pp. 238 – 247, 2006.

[57] T. Edvinsson, C. Li, N. Pschirer, J. Schöneboom, F. Eickemeyer, R. Sens, G. Boschloo, A. Herrmann, K. Müllen, and A. Hagfeldt, "Intramolecular charge-transfer tuning of perylenes: Spectroscopic features and performance in dye-sensitized solar cells," *J. Phys. Chem. C*, vol. 111, pp. 15137–15140, Oct. 2007.

[58] J. Xu, L. Wen, W. Zhou, J. Lv, Y. Guo, M. Zhu, H. Liu, Y. Li, and L. Jiang, "Asymmetric and symmetric dipole-dipole interactions drive distinct aggregation and emission behavior of intramolecular charge-transfer molecules," *J. Phys. Chem. C*, vol. 113, no. 15, pp. 5924–5932, 2009.

[59] J. Xu, H. Zheng, H. Liu, C. Zhou, Y. Zhao, Y. Li, and Y. Li, "Crystal hierarchical supramolecular architectures from 1-d precursor single-crystal seeds," *J. Phys. Chem. C*, vol. 114, no. 7, pp. 2925–2931, 2010.

[60] J. Xu, S. Semin, D. Niedzialek, P. H. J. Kouwer, E. Fron, E. Coutino, M. Savoini, Y. Li, J. Hofkens, H. Uji-I, D. Beljonne, T. Rasing, and A. E. Rowan, "Self-assembled organic microfibers for nonlinear optics," *Adv. Mat.*, vol. 25, no. 14, pp. 2084–2089, 2013.

[61] N. Miyaura and A. Suzuki, "Palladium-catalyzed cross-coupling reactions of organoboron compounds," *Chem. Rev.*, vol. 95, no. 7, pp. 2457–2483, 1995.

[62] G. R. Desiraju, "Hydrogen bridges in crystal engineering: interactions without borders.," *Acc. Chem. Res.*, vol. 35, pp. 565–73, July 2002.

[63] M. Kauranen and T. Verbiest, "Supramolecular second-order nonlinearity of polymers with orientationally correlated chromophores," *Science*, vol. 270, no. November, p. 966, 1995.

Chapter 2

Experimental approach

The aim of this chapter is to introduce the physical principles and experimental techniques used for the investigation of the optical properties of the diphenylalanine (FF) microtubes and 2,7-diphenyl-9H-fluoren-9-one (DPFO) microfibres. First we will discuss the linear and nonlinear optical processes occurring in both structures and the experimental set-ups for the investigation of their spectral and nonlinear optical properties. Then we introduce modifications of these techniques which allow to perform these optical investigations down to the micrometer-scale. We also describe the experimental set-up which can be used to study the wave-guiding properties of the structures.

2.1 Introduction

Miniaturisation of devices for electronic, optoelectronic and optics demands development of new materials and objects. Decreasing sizes of objects of interest make standard optical techniques inefficient when characterisation of individual objects is important, as not many techniques allow to study the optical properties on the micro and even nanoscale. This has led to amazing developments of high resolution microscopy techniques. Confocal, stimulated emission depletion (STED), stochastic optical reconstruction microscopy (STORM), scanning near field optical microscopy (SNOM) approaches were developed to push or even overcome the diffraction limit of light. While these high-resolution linear optical microscopy techniques undoubtedly are extremely useful and allow optical imaging at the nanoscale, other optical techniques can offer other benefits. Nonlinear optics and second-harmonic generation (SHG) in particular are proven techniques to study surface effects at interfaces of solids. Both of them have evolved into imaging techniques which resulted in the appearance of two-photon microscopy. This microscopy technique is well known for its highly localized excitation due to nonlinear effects and, hence high resolution and the possibility to work inside media like liquids and cells. Change of the focus position allows to reconstruct the three dimensional structure and therefore allows three dimensional imaging of objects[1]. However, for the objects investigated in this thesis, an extremely high resolution of hundreds of nanometres is not needed; more important is the sensitivity of SHG to the crystal structure of the materials of interest. We have used a modified SHG set-up in order to visualize the nonlinear optical response of objects and performed characterisation of their structure and physical properties.

The idea to use light for data exchange is quite old and can be found in heliographs and signal lamps, however modern implementation of this idea has drastically increased the speed of data transmission of the Internet. The miniaturisation of optical devices requires optical "wires" which will link elements of photonic integrated circuits which can be on the scale of microns. The materials of interest in this thesis can be grown in fibre-like structures that can act as waveguides. The properties of these "wires" should also be investigated.

This chapter will present the basic physical properties of light matter interaction which allows to understand the crucial features of nonlinear optics. The usefulness of the nonlinear optical effects for studies of microsized and nanosized materials will be presented. We will demonstrate examples of the experimental set-ups which can be used for the investigation of the nonlinear optical effects as well as waveguiding.

2.2 Light-matter interaction: Beyond the linear case

Different aspects of light matter interactions were carefully studied both theoretically and experimentally in optics, quantum mechanics and electrodynamics [2; 3]. They describe the linear interaction of light with atoms and molecules, the propagation of light in transparent media, reflection and scattering of light in opaque materials. The invention of the laser in 1960 helped to explore new effects of nonlinear optical origin which were previously not observed, like the generation of higher optical harmonics, the generation of sum and difference frequencies and self-focusing. Both linear and nonlinear interactions are nowadays widely used in photochemistry, photophysics, spectroscopy and microscopy.

The process of light-matter interaction can be described with the classical Lorentz oscillator model [4]. Typical quantum systems do not have any polarisation without external field (except some excited atoms, polar molecules). However when light interacts with an atom, the oscillating electro-magnetic field polarizes the atom, i.e. the atom can be treated as a dipole because the electron distribution changes its position relative to the nucleus. For simplicity, we suppose that the medium is non-conducting and that the electrons are bound to the nuclei, and the attraction of the other nuclei is negligible. Within the electric-dipole approximation, the induced charge distribution in the ensemble of atoms can be described on a macroscopic level as an induced electric-dipole moment (polarisation).

Light induced polarisation strongly depends on the external field E. At low intensities of external fields a linear approximation is valid. However for larger E one has to take into account higher order terms. The total polarization of the material which interacts with the light can be written in the following form [4]:

$$P_i = \chi_{ij} E_j + \chi_{ijk} E_j E_k + \chi_{ijkl} E_j E_k E_l + ... \tag{2.1}$$

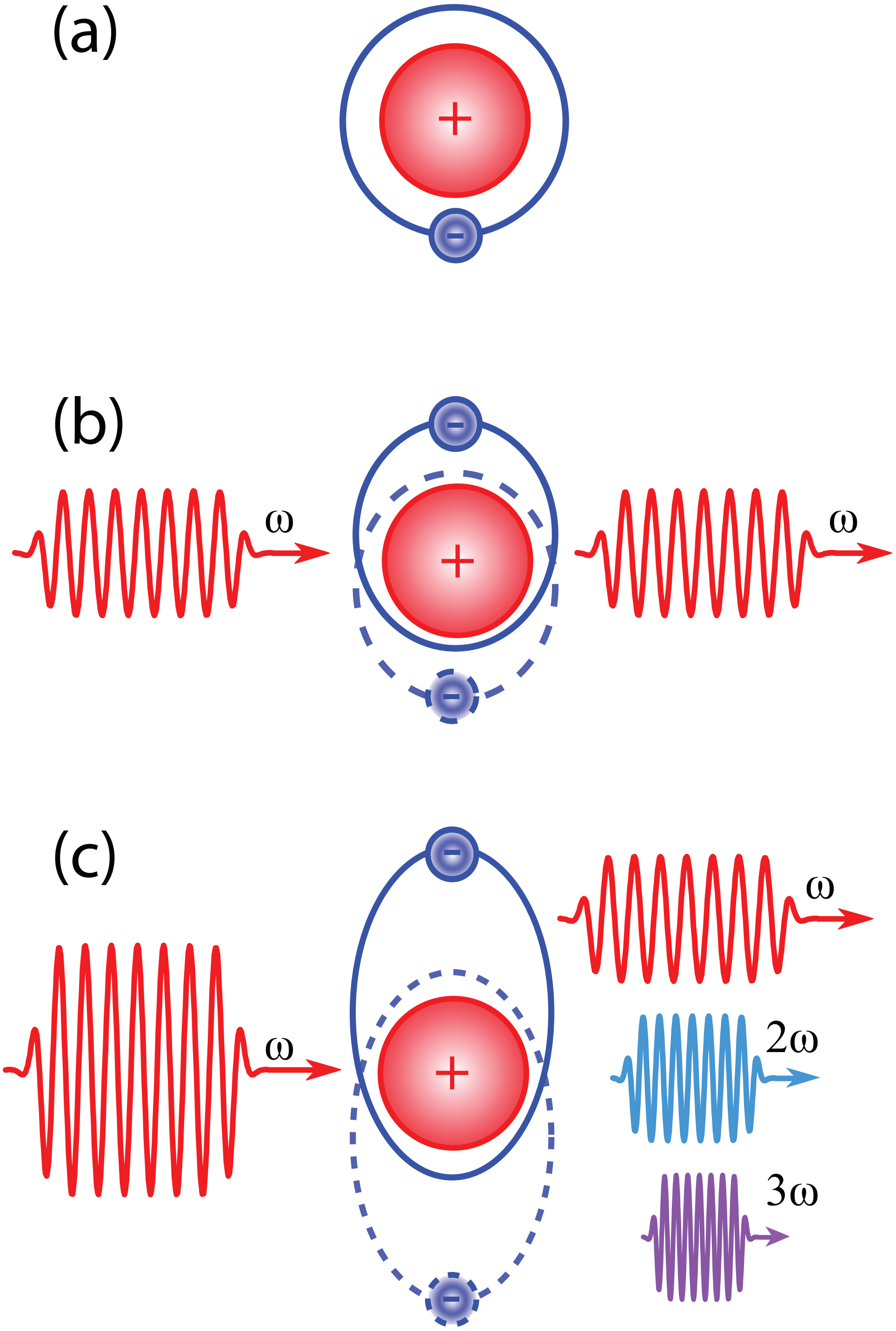

Figure 2.1: Excitation of the electron atom system in electric-dipole approximation; (a) No light excitation, system is not disturbed; (b) Linear case: system is excited with low light intensity at ω frequency which leads to formation of induced polarisation. Formed dipole re-emits light at the same frequency ω as incident; (c) Nonlinear case: system is excited with high light intensity. Higher harmonics (2ω and 3ω) appeared in re-emitted light.

where the first term is linear in the external field E and the coefficients χ_{ij} are responsible for linear optical effects like linear absorption, reflection and scattering. All the other terms are related to non-linear optical effects, where the second term χ_{ijk} is called the second-order non-linear susceptibility and describes second harmonic generation, sum and difference frequency generation. The third order term χ_{ijkl} describes generation of third harmonic, two-photon absorption and stimulated Raman processes. The expansion can be continued describing other higher harmonic effects. In this Thesis we focus mostly on the investigation of second-harmonic generation and two-photon luminescence, so the following parts will describe the basic concepts of these effects.

2.2.1 Second harmonic generation

Second harmonic generation (SHG) can be defined as the conversion of light with a specific frequency ω_1 into light with the doubled frequency $\omega_1 \longrightarrow 2\omega_1$, or, if we speak about wavelength, light with half the wavelength is generated, as $\lambda = \frac{c}{2\pi\omega}$. The first observation of this effect was done by Franken *et al.* in 1961[5]. The work described second harmonic generation in a quartz crystal excited with the help of a ruby laser. Since that day the efficiency and understanding of this process has improved a lot and SHG has become a standard characterization technique of materials and their interfaces[6].

This section will give short introduction and description of the SHG process to reveal important issues needed for understanding the experimental results.

As it was already shown in the previous section the second harmonic generation occurs due to the appearance of the second term in the total polarisation equation 2.1:

$$P^{2\omega}{}_i = \chi_{ijk} E_j E_k \tag{2.2}$$

This non-linear polarisation term at 2ω frequency emits light which is described by:

$$\nabla^2 E^{2\omega} - \mu\varepsilon_0 \frac{\partial^2 E^{2\omega}}{\partial t^2} = \mu \frac{\partial^2 P^{2\omega}}{\partial t^2} \tag{2.3}$$

with some simplification, the solution for this equation can be written in the following form:

$$E(z,t) = \frac{-i\mu_0\omega^2}{2k} P z \tag{2.4}$$

As it can be seen in eq. 2.4 the emitted $E(z,t)$ depends on the propagation distance which can result in phase delay between the induced polarisation and the generated light. The new sources of generated light can become out of phase and cancel each other out. In order to maximize the SHG signal light, the condition of so called phase matching should be fulfilled. This can be seen as follows: $k_\omega = k_{2\omega}$. The expression of the light electric field after propagation in the nonlinear medium of thickness L becomes:

$$E(L,t) = \frac{-i\mu_0\omega^2}{k} P L \mathrm{sinc}(\Delta k L/2) \tag{2.5}$$

The sinc(x) function has a maximum at x=0, which shows that the nonlinear optical effect has greater efficiency if $\Delta k = 0$, where $\Delta k = k_\omega - k_{2\omega}$. For the case of collinear SHG generation this means that the refractive indices for fundamental and second harmonic wave should be equal: $n_\omega = n_{2\omega}$.

The SHG intensity $I^{2\omega}$ can be derived from this equation as $P = \frac{1}{2}\varepsilon_0\chi^{(2)}(E^\omega)^2$ and also assuming that the intensity of the light is proportional to the square of electric field $I = (n/2\eta_0)|E|^2$ where $\eta_0 = \sqrt{\mu_0/\varepsilon_0}$. So the final expression of the SHG intensity is:

$$I^{2\omega} = \frac{\eta_0\omega^2(\chi^{(2)})^2(I^\omega)^2L^2}{2{c_0}^2n^3}\mathrm{sinc}^2(\Delta kL/2) \tag{2.6}$$

This expression demonstrates that the intensity of the SHG is proportional to the tensor of the non-linear susceptibility $I_{2\omega} \propto \chi^{(2)}$. The susceptibility $\chi^{(2)}$ is related to the crystallographic properties of the materials.The second order nonlinear susceptibility χ_{ijk} is a third-rank tensor and contains 27 elements. Often the number of tensor elements can be reduced by taking into account the symmetry of the system. The existence of inversion symmetry in the material makes $\chi_{ijk} = 0$, which results in the absence of SHG in the electric-dipole approximation. Second harmonic response is possible in noncentrosymmetric systems(ferroelectric [7], piezoelectric crystals [8], chiral materials [9], interfaces and at surfaces of centrosymmetric materials [6], where this symmetry is necessarily broken).

In general, the source of electromagnetic radiation is not only limited to the oscillating electric-dipole term. Magnetic dipole (MD) and quadrupole (Q) terms also contribute to the generated signal. So the electromagnetic wave equation can be expanded in the general case as:

$$\nabla^2\overrightarrow{E} - \mu\varepsilon_0\frac{\partial^2\overrightarrow{E}}{\partial t^2} = \mu\frac{\partial^2\overrightarrow{P}}{\partial t^2} + \mu(\nabla \times \frac{\partial\overrightarrow{M}}{\partial t}) - \mu\nabla\frac{\partial^2\widehat{Q}}{\partial t^2} \tag{2.7}$$

Contributions of the MD and Q terms are usually much smaller than the ED one and very often are indistinguishable. Recent developments in nanotechnology renewed the interest in higher harmonic generation and SHG in particular [10–12]. The reason for this is that the SHG method was applied not only to macrosized objects like bulk crystals and interfaces but also to nanosized objects (NSO). An important point here is that miniaturization of optical components demands the study of the non-linear optical properties at the micro- and nanoscale, e.g. SHG in metallic NSO's has distinct features. The optical response from metalic NSO originates from plasmonic oscillations of the conduction electrons near the metal-dielectric interface at optical frequencies.

The nonlinear optical response was also studied in semiconductor NSO: GaN [13] and ZnO[14] nanowires are good examples of them. Both materials demonstrated a high polarization dependence of the nonlinear optical response and high nonlinear susceptibility values. These works clearly demonstrate that SHG allows optical characterisation of the materials at the nanoscale.

The study of the nonlinear optical properties of ferroelectric nanoparticles ($BaTiO_3$) revealed a dependence of the observed signal on the nanoparticle size [11].

Effects occurring in micro- and nanobjects significantly modify their nonlinear optical properties, making SHG an efficient experimental tool.

2.2.2 Estimation of the nonlinear optical susceptibility

The investigation of the nonlinear optical properties of materials is not complete without an estimation of the nonlinear susceptibility of the materials. One of the common approaches to obtain the second order nonlinear susceptibility of materials is the Maker fringes technique[15; 16]. In this technique the optical thickness of the sample is changed by tilting of the sample. The variation results in an interference pattern of the generated SHG, which originates from the difference in the phase velocities of the fundamental and SHG wavelengths 2.6. Modifications of this technique exists as its original version does not consider the anisotropy of materials, absorption, multiple reflection and some multiple-dipole bulk contributions which can lead to mistakes in nonlinear susceptibility estimations [17; 18]. However, despite the fact that the Maker fringes technique can give quite precise values, all its modifications uses relatively large crystalline samples for characterisation which is not achievable for the case of microstuctures investigated in this thesis. A technique which can be be used for a simple and quick estimation of the SHG efficiency is the Kurtz powder technique [19]. It uses powders of the materials and can allow a rough estimate of the nonlinear coefficients of the materials compared with a known reference sample.

2.2.3 Two-photon absorption/luminescence

A further two-photon effect studied in this thesis is two-photon luminescence (TPL). Before proper explanation the one-photon absorption should be discussed.

The probability of an electron to be excited from the ground state (E_{gs}) to a higher excited state (E_{es}) is the highest when there is resonance between the photon energy $\hbar\omega$ and the energy of the transition $E_{es} - E_{gs}$. The second requirement follows from the selection rules which allow certain transitions and forbids others. For the case of electrical dipole interaction and linear polarisation of the excitation light the selection rules for the transition from the ground to excited state, $gs \rightarrow es$ are expressed as:

$$\begin{aligned} &\pi_{es}/\pi_{gs} = -1 \\ &\Delta J = J_{es} - J_{gs} = +1, 0, -1 \\ &\Delta M = M_{es} - M_{gs} = 0 \end{aligned} \tag{2.8}$$

where π is the parity, J- the total angular momentum, and M- the magnetic quantum number. For the case of circularly polarized excitation light $\Delta M = \pm 1$. However, for very intense light fields these selection rules can be different. If both the energy conservation law and selection rules allow a transition its probability per time unit can be described by the Fermi golden rule:

$$\Pi = 2\pi |V^{(1)}_{gs\rightarrow es}| \rho_{es} \tag{2.9}$$

where $V^{(1)}_{gs\to es}$ is a matrix element of the transition from the ground to the excited state, and ρ_{es} is the density of states at the excited state level. If the excited state is not disturbed by the external field, the density of states can be described as a Lorentz distribution with the half-width equal to γ_{es}, which corresponds to the spectral linewidth of the excited state.

The theory of two-photon absorption was proposed by Maria Goppert-Mayer in 1931 in her doctoral thesis. The first observation of this phenomena was done for Eu^{2+} only 30 years later [20]. Like second harmonic generation the two-photon absorption is also a nonlinear optical process. Unlike the process of single-photon absorption, when one photon with energy equal or larger than the transition energy is used to excite an electron in an atom or molecule, the simultaneous absorption of two photons is needed. In general, any combination of photons of different energies that sum up to overcome the difference between ground and excited state can be used. From practical considerations usually photons of the same wavelength are used. The probability of the simultaneous absorption process is very low, so high light fluxes ($10^{20} - 10^{30}\,\frac{\mathrm{photons}}{cm^2 s}$) are needed in order to generate two-photon generated signals, sufficient for detection. Such photon fluxes can be achieved by pulsed laser sources like a Ti:Sapphire femtosecond laser (e.g. a 20 mW 100 fs pulse contains $10^{28}\,\frac{\mathrm{photons}}{cm^2 s}$). Concentration of the light in the time and spatial domain helps to increase the probability of two-photon absorption. The quantitative value which is used to measure the probability of the two-photon absorption is the two-photon cross-section σ_{2p}.

When an electron is excited to a higher level, several ways exist for an electron to relax from the excited level (Fig. 2.2) [21]. It can relax without emission of the photon and its energy will be transferred, for example, to the lattice which results in an increase of the sample temperature. In another route, the electron falls back to the ground state and a photon is emitted. This process takes about $10^{-8} - 10^{-9}$s (fig. 2.3). The emitted photon can have smaller energy than the absorbed one, due to the losses caused by vibrational-rotational relaxation. This process is called fluorescence. Alternative routes of electron relaxation include intersystem crossing which brings the electron to a triplet state level before it goes to the ground state. The lifetime of this excited state is significantly longer than in the fluorescence case due to the lower probability of the relaxation process. It can last from 10^{-4}s to tens of seconds. This process is called phosphorescence. The timescales of radiative and nonradiative processes are summarized in figure 2.3.

2.3 Experimental techniques

Among many other techniques used for the characterisation of the investigated materials, this chapter will focus on the optical techniques. As described in the previous chapter, the investigated samples consist of randomly positioned and oriented objects with sizes ranging from several microns to tens of microns. The size of the objects requires the implementation of microscopic techniques to have the possibility to separate signals from neighbouring objects. The other requirement comes from the

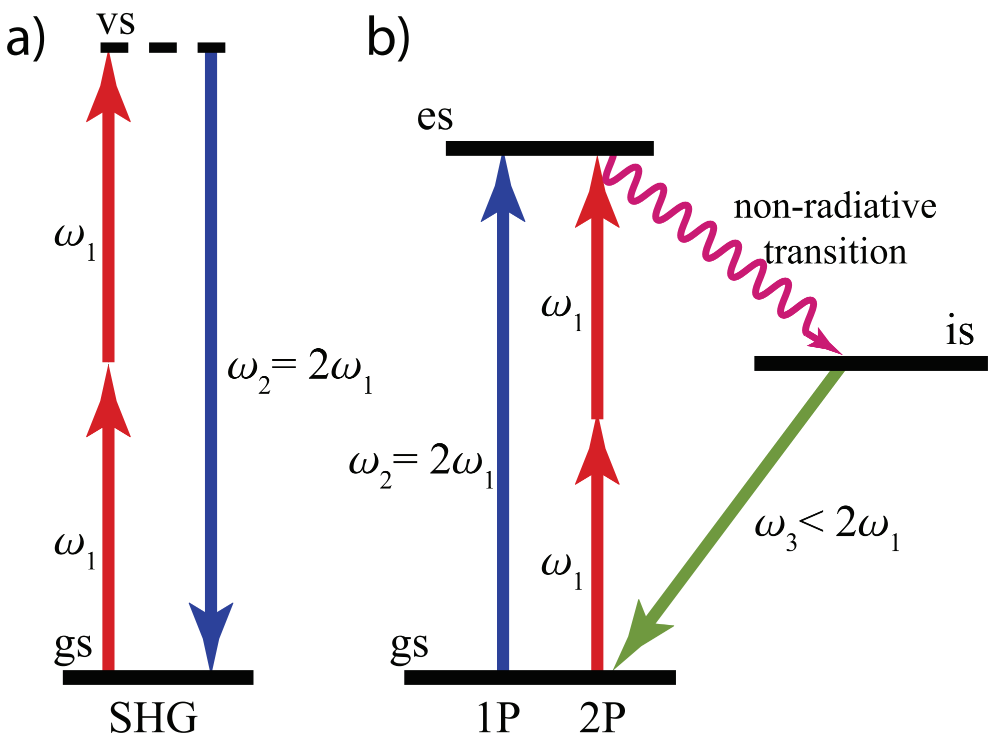

Figure 2.2: Jablonski diagram of the sample excitation a) SHG generation process, the excitation of the electrons by means of two photons of frequency ω_1 to virtual state **vs** ; b) One and two-photon photoluminescence mechanisms.One photon with the frequency ω_2 or two photons with the frequency ω_1 can be used to send electron to excited state **es**.

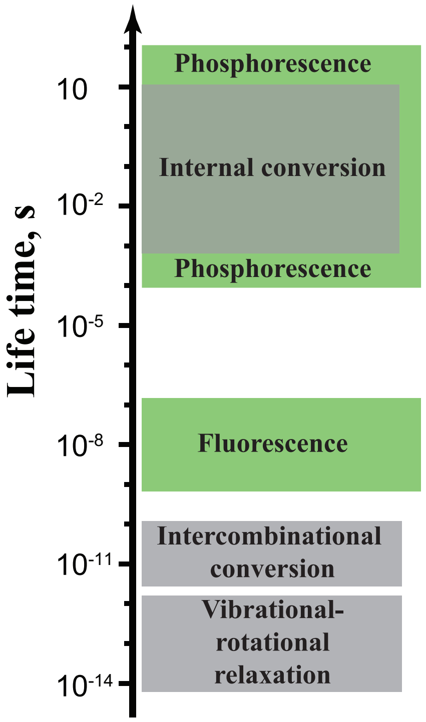

Figure 2.3: Characteristic times of photophysical processes. Green regions correspond to the radiative processes, gray to the nonradiative.

complex nature of the optical response generated in the material. To fulfil this requirement, spectroscopic instrumentation was used to separate registered signals spectrally. This section will give a short overview of the experimental set-ups which were used for the investigation of the nonlinear optical effects in organic molecules which were self-organized as micrometer sized objects.

2.3.1 Second harmonic polarimetry

The basic approach used for the investigation of the SHG response from surfaces and interfaces is called far-field polarimetry. This configuration was used by Franken [5]. The standard set-up for such a measurements is shown in figure 2.4. Linearly polarised light at fundamental frequency ω is focused on the surface of the sample at an incidence angle θ (fig.2.4). Filtered second harmonic signal at frequency 2ω is collected with a detector, due to the low signals it is often necessary to use a photomultiplier tube (PMT). For detection, the transmission geometry can be exploited (thickness and absorption properties of sample and substrate should be taken into account) or the reflection geometry (when sample and substrate are opaque for fundamental and/or second harmonic wavelengths). In the reflection geometry the SHG signal primarily originates from a layer depth within the coherence length. An analysing polariser is placed in the detection part in order to select the desired polarisation component $E_{2\omega,i}$ of the generated SHG. By choosing appropriate settings for the input and output polarisation and sample orientation, it is possible to probe the different elements of the nonlinear susceptibility tensor. Conventionally, polarisation states are defined relative to the plane of incidence. If the polarisation is parallel to the plane of incidence the state is called p-polarized, when the polarisation is perpendicular to the plane of incidence then the state is s-polarized.

A frequently used approach is anisotropy measurements: the sample is rotated around its normal, while input and output polarisation are fixed in the p- or s-state. Measured patterns of SHG intensity $I_{2\omega}(\varphi)$ depends on angle of sample rotation φ and can be measured at four combinations of polariser and analyser p-p, p-s, s-p, s-s. The relation $I_{2\omega}(\varphi) \propto \chi^2$ allows to derive the components of the nonlinear susceptibility tensor and yields information about the structure of the investigated sample.

A further experiment is done in the configuration when input polariser is constantly rotated and sample and output polariser are both fixed. These polarisation measurements can be used to estimate the molecular alignment inside the film. The intensity of SHG is related to the components of the nonlinear tensor $I(2\omega) \propto \chi^2$. The polarisation dependence is fitted to model equations in order to determine the components of the microscopic nonlinear susceptibility χ. The χ components are related to the molecular nonlinear polarisability β, which describes the nonlinear response of the individual molecules. The ratio between the components of χ and β results in the orientation parameter D, which describes the average orientation of the molecules in the monolayers. However, it should be mentioned that this approach is usually applied when anisotropy measurements can not be performed due to the inability to rotate a sample.

Polarimetry is a flexible approach in terms of control of experimental conditions: temperature, pressure, electric and magnetic fields [22–26].

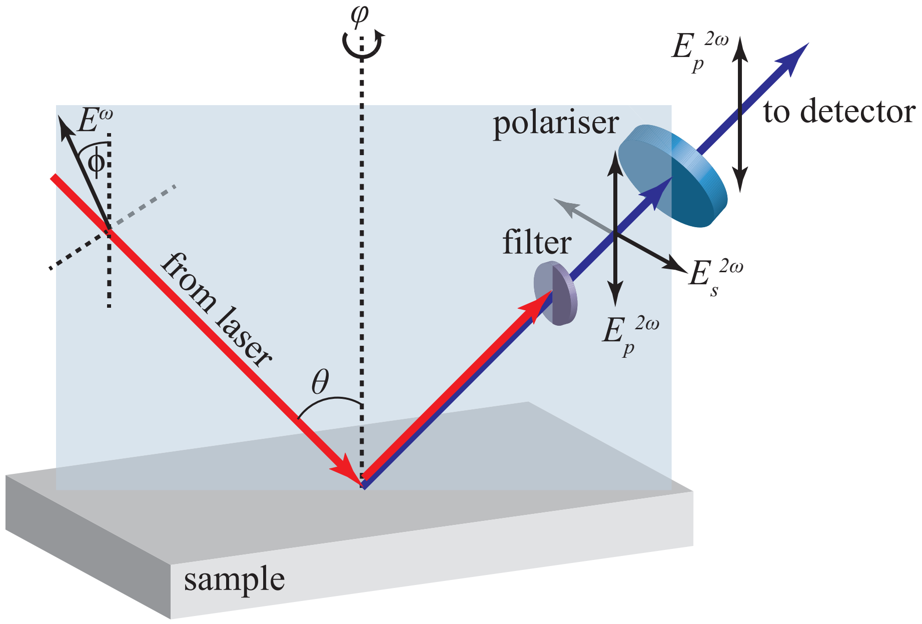

Figure 2.4: Schematic set-up used for for far-field polarimetry in general refection geometry. Incident and reflected laser beams are marked with red arrow. Polarised light of polarisation ϕ hits the sample at the angle of incidence θ. Reflected beam and generated SHG signal goes in the direction of the detector. The filter is used to cut light at the fundamental frequency, the analyser is used to the detect p- and s-polarized components of the SHG. The sample can be rotated around its normal at an angle φ Note that lenses which are usually used for focussing and collection of the light are not depicted.

2.3.2 SHG and TPL microscopy

The main advantage of SHG microscopy over far-field SHG experiments arises from the fact that one can visualize the nonlinear optical response from different parts of a sample. In general, different parts of the sample can produce SHG signal which can differ both in amplitude and phase. The luminescence properties of a material can be also used as the TPL can be detected in the same set-up. The concept of SHG microscopy was successfully used for the investigation of domains in ferromagnetics [27], ferroelectrics [28], multiferroics [29], semiconductor microstructures [30] and the crystalline structure of molecular crystals [31]. Also organic materials, including biological objects, like collagen fibril [32; 33] were successfully investigated with the help of this technique.

Imaging of the non-linear optical response can be performed with scanning, which demands relative shifts of the laser beam and sample. Scanning in the experimental set-up can be performed via two approaches: scanning the laser beam (via a mirror) or scanning the sample. The first approach is faster, but the area of interest is limited as the laser beam should go through the microscope objective aperture. The second one allows to scan larger target areas, but is rather slow. Any of the scanning methods results in a two-dimensional map of SHG intensity linked to the sample coordinates. Theoretically, the resolution of this technique is limited to roughly half the wavelength of the excitation light, as the beam can not be focused better due to the diffraction limit. However the effective resolution due to the nonlinear nature of the optical process can be slightly better. This comes from the fact that a two-photon excited process depends quadratically on the excitation power. So the effective resolution at the second harmonic can be $\sqrt{2}$ better than the resolution at the fundamental wavelength [7]. As we are interested more in flexibility of the optical characterisation rather than in high resolution imaging we have chosen the sample scanning approach, despite the fact it is slower.

Combination of SHG with a confocal geometry allows to increase optical resolution of a microscope. A greater improvement can be reached with the help of near field optical microscopy techniques. Despite the fact that we performed some experiments with a confocal microscope in the nonlinear regime, this data did not give a lot of additional information except of increased resolution. As our objects have typical sizes of several microns or more, the high resolution optical images are not important in most cases.

2.4 Experimental set-ups

The variety of optical effects occurring in the self-organizing organic materials require different approaches for their investigations. Several experimental configurations were used for the investigation of the optical properties of FF and DPFO microstructures.

2.4.1 SHG and TPL polarimetry/scanning set-up

For investigation of the nonlinear optical properties of organic materials we have used the following set-up (fig. 2.5 (a)). It is the extended version of the set-up described in fig.2.4(sec. 2.3.1). We used a tunable femtosecond laser to excite microstructures (Mai Tai, Spectra Physics) at wavelengths in the range from 700 to 990 nm. Pulse width of the laser was about 100 fs with a repetition rate of 82 MHz. We used a lens with a working distance of 3 centimetres and with a gradient change of index of refraction (GRIN lens) to focus the laser radiation on the sample. This lens helps to reduce aberrations, such that the laser can be focused to a spot of about 6 μm in diameter allowing the investigation of the optical properties of individual tubes. The samples were mounted on an computer-controlled XY-scanning table. Light reflected from the tube through the fibre waveguide was led to a monochromator (Acton SP2300, Princeton Instruments). One of the monocromator outputs is connected to a cooled CCD detector (Pylon, Princeton Instruments), which allows to register the entire spectrum from the sample. The detected light can be also send through a monochromator to a photomultiplier tube (PMT) (Hamamatsu H10682-210 photon counting unit), enabling registration of the optical response at a particular wavelength. The detection part can be easily switched by using a flip-mirror. The entrance of the fibre waveguide was placed on the rotational arm, which allows investigation of the objects at different angles of incidence.

2.4.2 Waveguiding set-up

Waveguiding properties of microstructures were investigated in two geometries. The main difference between them arises from the manner of light coupling relative to the direction of wave propagation. In one geometry the $\vec{k}$ of the excitation light is parallel to the direction of propagation (fig. 2.6a)). This approach can be found in fiber optical communication systems as it allows to reach coupling with high efficiency. For investigation of the optical properties of waveguiding microstructures or photonic crystals one needs extra effort compared to the currently used optical waveguides. The small sizes of the objects require the light coupling into the structure and system alignment on a sub-micron scale for coupling optimisation. Optical fibres with tapered end can be used for better local light coupling [34]. Tapered tips can be obtained either by heating and pulling or by chemical etching[35; 36]. Combination with the scanning platform for the sample or the fiber itself helps carefully aligning and investigating waveguiding properties of microsized objects. This type of waveguiding is usually called passive as the sample does not generate light.

Waveguiding can also be observed in geometries, where the object is excited, with $\vec{k}$ of the light perpendicular to the fiber (or propagation direction, e.g. in a confocal microscope) and the internally generated light is observed via scattering at the ends of the fiber (fig. 2.6b)). Light coupling efficiency is lower than in previous case as edge defects scatter the light or the laser focus spot can be bigger than the object but it is sometimes the only way to investigate waveguiding properties of nano-objects. In order to increase the coupling efficiency, the absorption of the sample should match

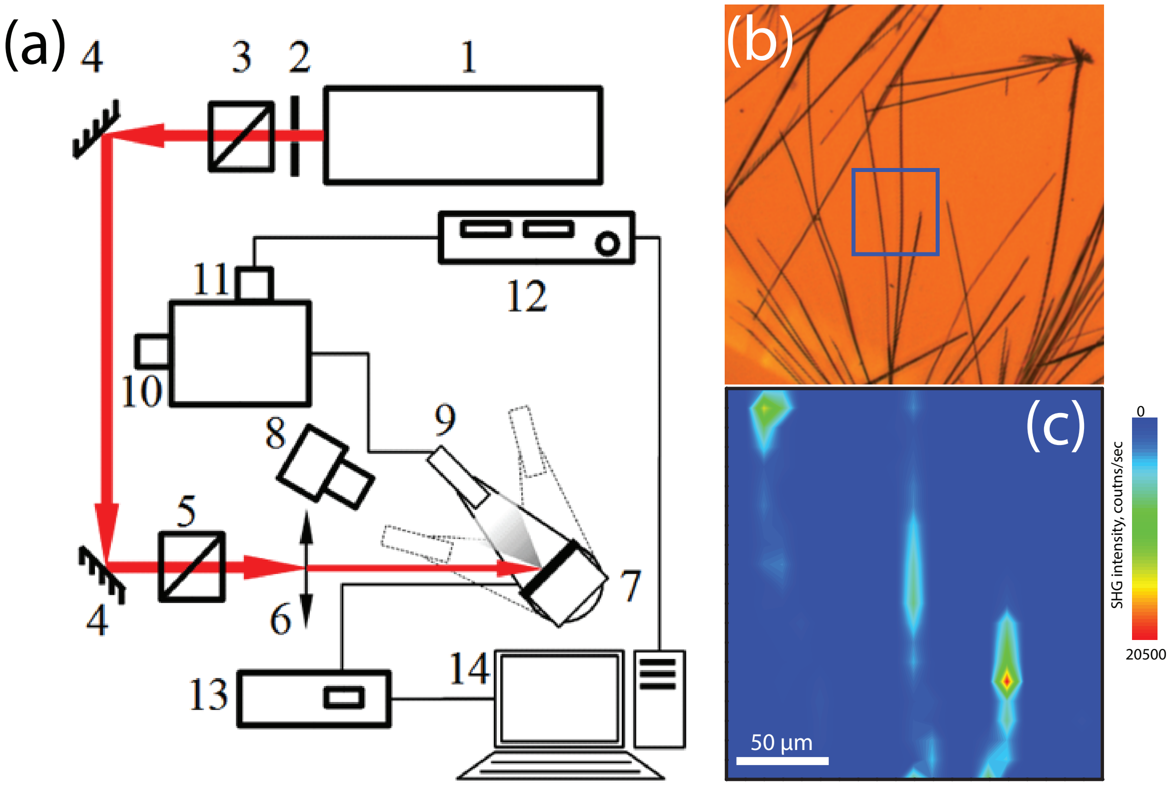

Figure 2.5: (a) Set-up used for SHG measurements of organic microstructures; 1-femtosecond laser; 2-chopper; 3- half-wave plate; 4-mirrors; 5-polariser; 6-focusing lens; 7-XY-scanning table; 8- CCD camera for imaging; 9- waveguide input aperture; 10-photo multiplying tube; 11-Liquid nitrogen cooled CCD for spectral measurements, 12-photon counter; 13- XY-controller; 14-computer; (b) Optical image of the peptide microtubes dropcasted on the glass substrate, square marks region which was scanned ; (c) SHG scan of the FF peptide tubes.

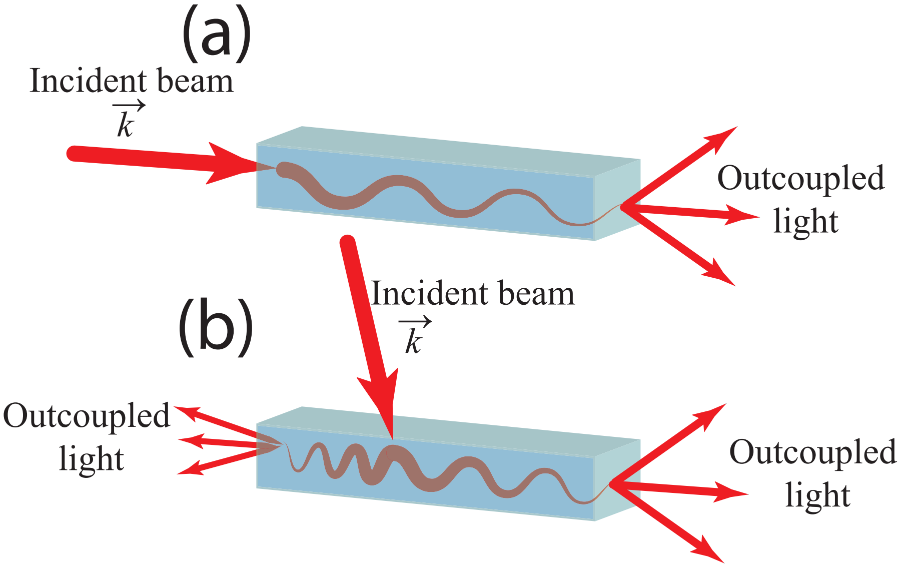

Figure 2.6: Two geometries of wave propagation; a) $\vec{k}$ of incident light is parallel to the propagation direction; b)$\vec{k}$ of incident light is perpendicular to the propagation direction.

the excitation[37–39]. When light with wavelength different from the excitation is generated, such type of waveguide is called active as the object generates the propagating light.

The set-up used for these experiments has different light sources that can be changed between a femtosecond laser ($\lambda = 760 - 840$ nm, Mira 900F, Coherent), a tunable IR diode laser ($\lambda = 1480 - 1560$ nm, Tunics BT, CN Nettest) and a white light source (halogen lamp). The frequency of the femtosecond laser can be doubled with a nonlinear optical crystal which results in 400 nm wavelength. Light from one of the light sources was coupled into the optical fibre, the other part of which has a tapered end allowing to couple light into the micron-sized devices. The propagated light is collected by another optical fibre and can be sent to the PMT or spectrometer if the light source is the femtosecond laser, or to the GaAs diode if the light source is the IR-laser. Both input and output laser can be positioned with mechanical stages and more precisely with piezostages. The presence of the automated stages allows to optimize the coupling of the light and obtain a 2D-map of the intensity distribution in the medium. The microscope with the camera mounted above the sample and fibres allows to adjust the position of the sample and fibres with respect to each other, with an accuracy of 500 nm for the mechanical stages and about 10 nm for the piezoelectric stage. In this way one can visualise the spatial distribution of the outcoupled light which can give information about optical modes inside the waveguide.

The previously described approach works well only if there is free access to the entrance of the waveguiding structures and the sides of the structures do not have defects which have negative influence on coupling into the structure. As an alternative for the cases that were unaccessible otherwise we used a set-up based on an inverted optical microscope (fig. 2.8). Light from a femtosecond laser was sent through a combination of half-wave plate and polariser for the possibility to control the intensity of light on the sample. The attenuated light was sent to the microscope objective via mirrors.

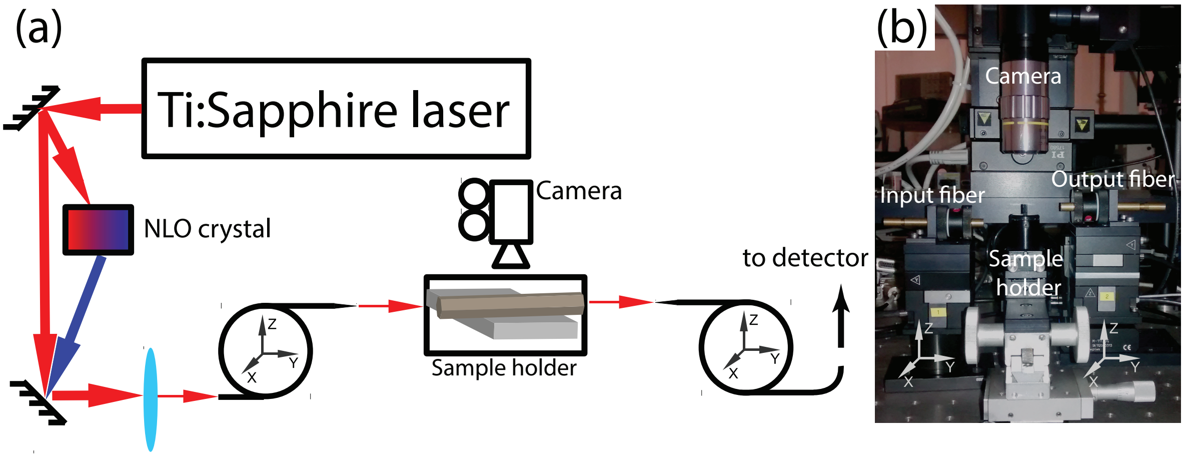

Figure 2.7: (a) Set-up used for investigation of the waveguiding in microobjects. The NLO crystal can be used to convert the excitation light to the double frequency. Tapered ends of both fibres are mounted on micrometer/piezo stages; (b) Photograph of scanning part of the set-up

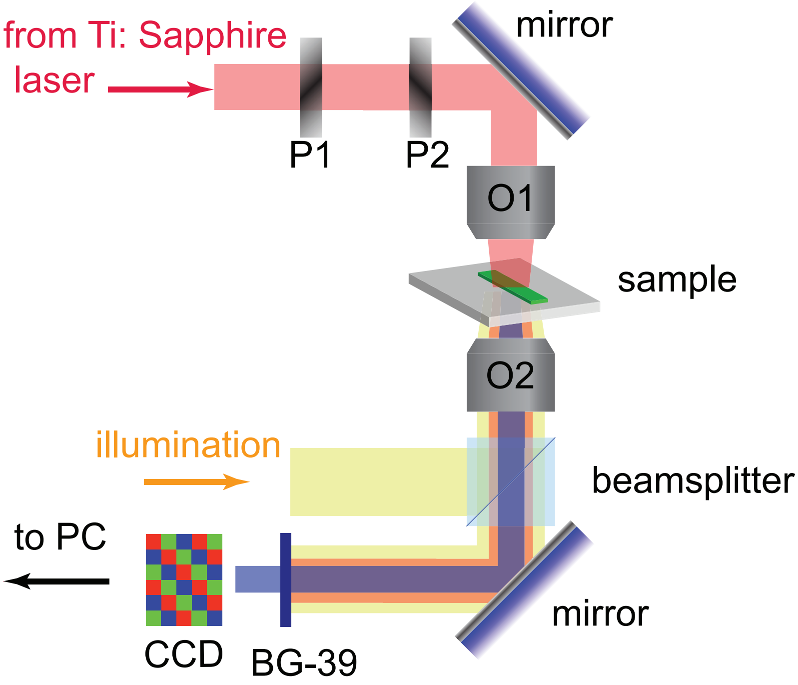

Figure 2.8: Set-up for investigation of the waveguiding properties. The set-up is based on an inverted microscope (Olympus). P1 is a halfwave waveplate, P2 is a Glan polarizer, O1 and O2 are the focusing and collecting objectives, respectively. The CCD- camera is connected to a PC for image analysis.

With the help of the objective light was focused on the surface of the sample. Light that was generated at the excitation spot and coupled (via defects) into the fibre was sent through the BG-39 filter (to remove the excitation laser wavelength) and can be detected by a CCD.

2.5 Conclusions

In this chapter, the main features of the nonlinear optical effects, including SHG and TPL are outlined. The nonlinear nature of both of these effects make them efficient tools to study properties of materials together with the appropriate experimental set-ups. A few key differences between SHG and TPL should be pointed out.

In a general case, SHG is a nonresonant process, i.e. electrons are excited to a virtual state. SHG is strongly related to the crystal symmetry of the material, as it is a second order nonlinear optical process. TPL is a resonant process, i.e. there should be absorption of the photon at a particular wavelength and electrons are excited to a real state with higher energy, where some radiative or nonradiative relaxation can occur. It makes the emission much broader and leads to longer relaxation times compared to SHG. Two photon absorption and hence luminescence have their origin in the optical properties of individual atoms or molecules, however they can be influenced by the the arrangement.

References

[1] G. Katona, G. Szalay, P. Maák, A. Kaszás, M. Veress, D. Hillier, B. Chiovini, E. S. Vizi, B. Roska, and B. Rózsa, “Fast two-photon in vivo imaging with three-dimensional random-access scanning in large tissue volumes.,” *Nat. Methods*, vol. 9, pp. 201–8, Feb. 2012.

[2] L. D. Landau, L. P. Pitaevskii, and E. M. Lifshitz, *Electrodynamics of Continuous Media, Second Edition: Volume 8 (Course of Theoretical Physics).* Butterworth-Heinemann, 2 ed., Jan. 1984.

[3] J. D. Jackson, *Classical Electrodynamics Third Edition*, vol. 67. 1999.

[4] F. Zernike and J. Midwinter, *Applied Nonlinear Optics.* Dover books on physics, Dover Publications, 2006.

[5] P. A. Franken, A. E. Hill, C. W. Peters, and G. Weinreich, “Generation of optical harmonics,” *Phys. Rev. Lett.*, vol. 7, pp. 118–119, Aug 1961.

[6] Y. R. Shen, “Surface-properties probed by 2nd-harmonic and sum-frequency generation,” *Nature*, vol. 337, no. 6207, pp. 519–525, 1989.

[7] S. A. Denev, T. T. A. Lummen, E. Barnes, A. Kumar, and V. Gopalan, “Probing ferroelectrics using optical second harmonic generation,” *J. Am. Ceram. Soc.*, vol. 94, no. 9, pp. 2699–2727, 2011.

[8] R. C. Miller, "Optical 2nd harmonic generation in piezoelectric crystals (ferroelectrics)," *Appl. Phys. Lett.*, vol. 5, no. 1, pp. 17–19, 1964.

[9] S. Sioncke, T. Verbiest, and A. Persoons, "Second-order nonlinear optical properties of chiral materials," *Mat. Sci. Eng.: R*, vol. 42, pp. 115–155, Nov. 2003.

[10] J. Butet, J. Duboisset, G. Bachelier, I. Russier-Antoine, E. Benichou, C. Jonin, and P.-F. Brevet, "Optical second harmonic generation of single metallic nanoparticles embedded in a homogeneous medium," *Nano Lett.*, vol. 10, no. 5, pp. 1717–1721, 2010.

[11] E. Kim, A. Steinbruck, M. T. Buscaglia, V. Buscaglia, T. Pertsch, and R. Grange, "Second-harmonic generation of single batio3 nanoparticles down to 22 nm diameter," *ACS Nano*, vol. 7, no. 6, pp. 5343–5349, 2013.

[12] G. A. Wurtz, R. Pollard, W. Hendren, G. P. Wiederrecht, D. J. Gosztola, V. A. Podolskiy, and A. V. Zayats, "Designed ultrafast optical nonlinearity in a plasmonic nanorod metamaterial enhanced by nonlocality.," *Nat. Nanotechnol.*, vol. 6, pp. 107–11, Mar. 2011.

[13] J. P. Long, B. S. Simpkins, D. J. Rowenhorst, and P. E. Pehrsson, "Far-field imaging of optical second-harmonic generation in single gan nanowires.," *Nano Lett.*, vol. 7, pp. 831–6, Mar. 2007.

[14] J. C. Johnson, H. Yan, R. D. Schaller, P. B. Petersen, P. Yang, and R. J. Saykally, "Near-field imaging of nonlinear optical mixing in single zinc oxide nanowires," *Nano Lett.*, vol. 2, pp. 279–283, Apr. 2002.

[15] P. D. Maker, R. W. Terhune, M. Nisenoff, and C. M. Savage, "Effects of dispersion and focusing on the production of optical harmonics," *Phys. Rev. Lett.*, vol. 8, pp. 21–22, Jan 1962.

[16] J. Jerphagnon and S. Kurtz, "Maker fringes: a detailed comparison of theory and experiment for isotropic and uniaxial crystals," *J. Appl. Phys.*, vol. 41, no. 4, pp. 1667–1681, 1970.

[17] W. Herman and L. Hayden, "Maker fringes revisited: second-harmonic generation from birefringent or absorbing materials," *JOSA B*, vol. 12, no. 3, pp. 416–427, 1995.

[18] F. J. Rodriguez, F. X. Wang, and M. Kauranen, "Calibration of the second-order nonlinear optical susceptibility of surface and bulk of glass," *Opt. Express*, vol. 16, pp. 8704–10, June 2008.

[19] S. K. Kurtz and T. T. Perry, "A powder technique for evaluation of nonlinear optical materials," *J. Appl. Phys.*, vol. 39, no. 8, p. 3798, 1968.

[20] W. Kaiser and C. G. B. Garrett, "Two-Photon Excitation in CaF_2: Eu^{2+}," *Phys. Rev. Lett.*, vol. 7, pp. 229–231, Sep 1961.

[21] V. Gorelik and E. Zhabotinskii, “Two-photon-excited emission from solids,” *J. Russ. Las. Res.*, vol. 16, no. 4, pp. 287–308, 1995.

[22] K. Nouneh, I. Kityk, and K. Michalska-Malelcka, “Temperature dependences of the second-harmonic generation in $LiKB_4O_7$ single crystals,” *Las. Phys.*, vol. 18, no. 8, pp. 1–3, 2008.

[23] M. Fiebig and R. Pisarev, “Nonlinear optics-a powerful tool for the investigation of magnetic structures,” *J. Magn. Magn. Mater.*, vol. 272-276, pp. E1607–E1611, May 2004.

[24] Y. Li, G. Yang, and Z. Dreger, “Effect of high pressure on the second harmonic generation efficiencies of three monoclinic organic compounds,” *J. Phys. Chem. B*, vol. 102, no. 31, pp. 5963–5968, 1998.

[25] O. A. Aktsipetrov, A. A. Fedyanin, E. D. Mishina, A. N. Rubtsov, C. W. van Hasselt, M. A. C. Devillers, and T. Rasing, “DC-electric-field-induced second-harmonic generation in Si(111)-SiO_2-Cr metal-oxide-semiconductor structures,” *Phys. Rev. B*, vol. 54, pp. 1825–1832, Jul 1996.

[26] K. Sato, A. Kodama, M. Miyamoto, A. Petukhov, K. Takanashi, S. Mitani, H. Fujimori, A. Kirilyuk, and T. Rasing, “Anisotropic magnetization-induced second harmonic generation in fe/au superlattices,” *Phys. Rev. B*, vol. 64, p. 184427, Oct. 2001.

[27] A. Kirilyuk, V. Kirilyuk, and T. Rasing, “Nonlinear magneto-optical imaging of interface magnetic structures,” *J. Magn. Magn. Mater.*, vol. 198-199, pp. 620–623, June 1999.

[28] M. Flörsheimer, R. Paschotta, U. Kubitscheck, C. Brillert, D. Hofmann, L. Heuer, G. Schreiber, C. Verbeek, W. Sohler, and H. Fuchs, “Second-harmonic imaging of ferroelectric domains in $LiNbO_3$ with micron resolution in lateral and axial directions,” *Appl. Phys. B: Lasers Opt.*, vol. 67, pp. 593–599, Nov. 1998.

[29] R. Pisarev, “Second harmonic generation spectroscopy in magnetic and multiferroic materials,” *J. Luminesc.*, vol. 133, no. 0, pp. 169 – 174, 2013.

[30] S. I. Bozhevolnyi, A. Maidykovski, B. Vohnsen, and V. Zwiller, “Reflection second-harmonic microscopy of individual semiconductor microstructures,” *J. Appl. Phys.*, vol. 90, no. 12, p. 6357, 2001.

[31] S. Brasselet and J. Zyss, “Nonlinear polarimetry of molecular crystals down to the nanoscale,” *Comptes Rendus Physique*, vol. 8, no. 2, pp. 165 – 179, 2007.

[32] P. Stoller, P. M. Celliers, K. M. Reiser, and A. M. Rubenchik, “Quantitative second-harmonic generation microscopy in collagen,” *Appl. Opt.*, vol. 42, pp. 5209–19, Sept. 2003.

[33] T. A. Theodossiou, C. Thrasivoulou, C. Ekwobi, and D. L. Becker, "Second harmonic generation confocal microscopy of collagen type i from rat tendon cryosections," *Biophys. J.*, vol. 91, no. 12, pp. 4665–4677, 2006.

[34] I. Razdolskiy, S. Berneschi, G. N. Conti, S. Pelli, T. V. Murzina, G. C. Righini, and S. Soria, "Hybrid microspheres for nonlinear kerr switching devices," *Opt. Express*, vol. 19, pp. 9523–9528, May 2011.

[35] G. A. Valaskovic, M. Holton, and G. H. Morrison, "Parameter control, characterization, and optimization in the fabrication of optical fiber near-field probes.," *Appl. Opt.*, vol. 34, pp. 1215–28, Mar. 1995.

[36] P. Lambelet, A. Sayah, M. Pfeffer, C. Philipona, and F. Marquis-Weible, "Chemically etched fiber tips for near-field optical microscopy: A process for smoother tips," *Appl. Opt.*, vol. 37, pp. 7289–7292, Nov 1998.

[37] B. Yan, L. Liao, Y. You, X. Xu, Z. Zheng, Z. Shen, J. Ma, L. Tong, and T. Yu, "Single-crystalline V_2O_5 ultralong nanoribbon waveguides," *Advanced Materials*, vol. 21, pp. 2436–2440, June 2009.

[38] K. Takazawa, Y. Kitahama, Y. Kimura, and G. Kido, "Optical waveguide self-assembled from organic dye molecules in solution.," *Nano Lett.*, vol. 5, pp. 1293–6, July 2005.

[39] Y. S. Zhao, P. Zhan, J. Kim, C. Sun, and J. Huang, "Patterned growth of vertically aligned organic nanowire waveguide arrays.," *ACS Nano*, vol. 4, pp. 1630–6, Mar. 2010.

Chapter 3

Optical properties of diphenylalanine microtubes[1]

In this chapter we study the optical properties of microtubes based on diphenylalanine (FF) molecules formed by the process of self-assembly from a water solution. This process was influenced by a magnetic field resulting in alignment of the formed FF microtubes (FFMTs) along the direction of the magnetic field $\vec{B}$.

The molecular arrangement of individual FFMTs allows the presence of a strong second harmonic generation (SHG) response from the as-grown FFMTs, which decreases after a heat treatment of the sample. A phase transition is the possible reason of such a behaviour of the SHG intensity[1; 2]. We compare our observations with the results obtained with other techniques such as differential scanning calorimetry (DSC) and nuclear magnetic resonance (NMR). The observed phase transition modifies the optical properties of FFMTs in such a way that the FFMTs demonstrate new spectral features related to two-photon luminescence (TPL).

Our studies of the optical properties include the investigation of the waveguiding properties of both as-grown and heat-treated tubes. The results show a high propagation efficiency of FFMTs (up to 65% transmission) in the visible and IR optical ranges.

3.1 Introduction

Self-assembly of bioinspired functional materials with ordered organisation on the nano- and micro scale is attracting a lot of interest due to its versatility, structural simplicity, cost efficiency and biocompatibility. Among various biological building blocks that can self-assemble, diphenylalanine peptide (Phe-Phe, FF) is one of the simplest molecules which easily form micro- and nanostructures from aqueous solution. The

---

[1] This chapter is based on S. Semin et al., Small, 2014 and N. Amdursky, S. Semin et al., Biomacromolecules, 2011

interest in this molecule is connected to the fact that this FF peptide is the core recognition motif of the Alzheimers disease associated with β-amyloid polypeptide. The morphology of the self-assembled structures can be controlled via concentration or solvent, leading to the formation of spherical, fibrous and tubular structures, of which the latter have been investigated the most [3–6].

Water molecules play an important role for self-assembly of the FF tubes. FF molecules form coil-like structures with the hydrophilic internal part making the crystal lattice of the FFMTs to act as a cage for the water molecules. While self-assembly allows to obtain randomly oriented tubes, magnetic and electric fields can be used for their alignment. The diamagnetic anisotropy of the aromatic rings of phenylalanine as well as the dielectric nature of the FFMTs make them sensitive to aforementioned fields.

Many efforts were put into studies of the thermal stability of the FFMTs which resulted in the observation of a phase transition around 100 °C. This phase transition results in changes in the structural and physical properties of the FFMTs. The origin of the phase transition comes from the fact that water molecules evaporate from the internal channels of the FFMT. At higher temperatures a molecular transformation can be observed where the peptide molecule changes it structure from a linear to a cyclic form, which belongs to the diketopiperasine group of molecules.

Alongside with the chemical, structural and electronic properties, much attention was focused on the optical properties of FFMT's. It was shown that the FF dimer building blocks show luminescence located in the UV (284 nm, 4.37 eV) caused by the presence of aromatic rings, whereas the spectrum from FF microtubes (FFMTs) was red-shifted and consists of two peaks at 305 nm (4.07 eV) and at 450 nm (2.70 eV).

The linear response in the visible range is rather weak for applications. In order to enhance the luminescence and extend the functionality of the peptide tubes for optical applications, doping with dyes, photosensitizers and lanthanide ions can be done [7; 8]. This approach increases the intensity of the generated light and adds new emission lines to the optical spectra of the peptide tubes due to the energy-transfer from the FF to the photosensitizer molecules but requires extra steps in the fabrication process. Also, such process is applied to the whole tube (sample), which does not allow to induce modifications of the spectra locally (e.g. an individual tube or part of it), which can be essential for implementation in photonic devices.

The elongated form of the individual tubes as well as their dimensions makes them promising to be used as waveguides. Some experiments were done on the FFMTs with dyes incorporated [4; 9], however no studies were performed on the bare tubes.

This chapter starts with the description of the experiments on alignment of the FFMTs in magnetic fields and the topographical characterisation of the samples used for optical experiments. The remaining part of the chapter is dedicated to the investigation of the optical properties studied on individual FFMT samples. Our studies includes the investigation of the second harmonic generation (SHG) which originates from the noncentrosymmetric arrangement of the molecules inside the FFMTs. We observe that heat and laser induced phase transitions has a large influence on the nonlinear optical properties, resulting in a decrease of the SHG and the appearance of TPL. Practical implementation of the FFMTs as waveguides and study of this property is also demonstrated.

3.2 Alignment

The diphenylalanine (FF) molecule consists of two phenylalanine amino acid molecules connected by a peptide bond. The self-assembly of FF molecules in water results in the formation of randomly oriented tubular microobjects.

Howerver, control over alignment of self-assembled structures is important and needed for applications. Various approaches which can be used for alignment of microobjects were discussed in chapter 2. In our experiments, we used a magnetic field for alignment of the FFMTs.

The influence of the magnetic field on the alignment of the FFMT's can be attributed to the net diamagnetic anisotropy of the aromatic rings. This anisotropy is created due to the presence of a larger magnetic susceptibility in the direction perpendicular to the plane of an aromatic ring of diphenylalanine molecules relative to that in the plane [10].

We have used the facility of the High Field Magnet Laboratory (HFML Radboud University Nijmegen) for experiments on magnetic field alignment. Magnetic field alignment experiments were conducted for the FFMTs freely moving in an aqueous environment and for samples which were left to evaporate in a high magnetic field (20 T).

First we discuss the case when magnetic field was applied to the FFMT in an aqueous environment. Such experiments allow to remove the influence of the substrate's surface and make the effect of the magnetic field $\vec{B}$ to be dominant. For this experiment the solution of the FF molecules was placed in a transparent cuvette and orientations of the formed FFMTs were tracked with a camera *in situ* (fig. 3.1).

The concentration of the FF molecules in water was reduced (from 0.5 mg/ml to 0.05 mg/ml) in order to avoid aggregation of the FF tubes and to reduce their size. Indeed, short and well separated FF microtubes were formed and floated in the solvent with no preferable orientation when no field was applied (fig. 3.1a). Gradual increase of the magnetic field from 0 to 2 T led to the alignment of the randomly oriented FFMTs along the field direction (fig. 3.1b). Similar behaviour was also observed for tubes which were lying at the bottom of the cuvette. At 2 T they “stood up”, i.e. changed their alignment from horizontal to vertical, which means that the alignment effect of the magnetic field exceeded the influence of gravitation. This experiment demonstrated that the FFMTs in aqueous environment are sensitive to the presence of the magnetic field (1 T) and show 100% alignment.

Investigation of the physical properties of FFMTs in the aqueous environment is not convenient, from a practical point of view. It is desired to obtain aligned patterns of dried FFMTs on a substrate. Such experiments were performed before, however, about 50% of the tubes were aligned along the direction of the 12 T magnetic field on an area of about 125×125 μm [10]. To improve the alignment of the peptide tubes on the substrate during the self-assembly process shown in that work, we applied higher magnetic fields (20 T). The solution of the FF molecules in water was placed on a substrate between the poles of the magnet. The magnetic field was oriented vertically and the sample substrate was aligned to be parallel. The water droplet was hanging by surface tension like is shown on figure 3.2.

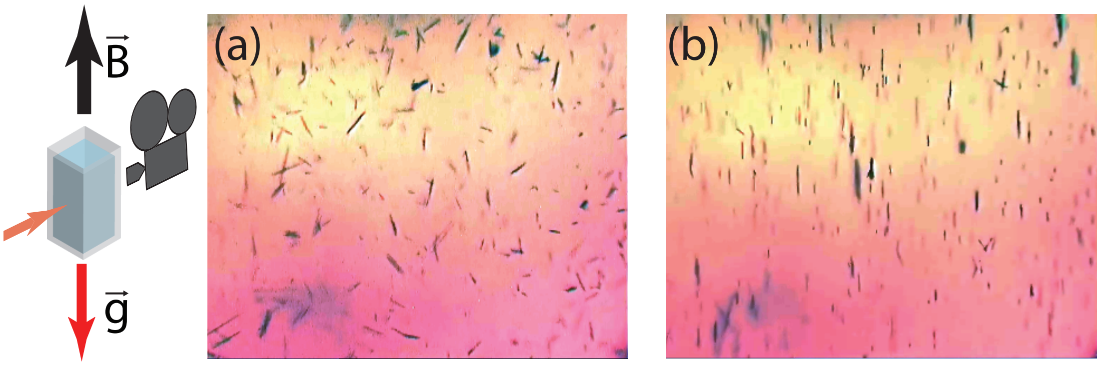

Figure 3.1: Alignment of the peptides tubes in a water solution in a magnetic field. (a)-corresponds to 0 T; (b) to 1 T, black arrow shows the direction of the magnetic field $\vec{B}$, and the red arrow demonstrates the direction of the gravity. Scheme on the left depicts experimental conditions and the position of the camera.

The sample was kept in a magnetic field for about 1 hour to keep the FF-microtubes under the influence of the magnetic field until the solvent was completely evaporated. Mica, silicon and glass substrates were used for this experiment to be sure that the water droplet with the FFMTs would remain on the substrate without dropping down as substrates have different wettability. The concentration of the FF solvent was kept the same for different substrates and experiments in the presence and the absence of the field. We performed a control experiment of self-assembly without magnetic field (fig. 3.2 (left column)), where formation of randomly oriented tubes on all substrates for $\vec{B} = 0$ occurs.

The experiments performed in the presence of the magnetic field demonstrated alignment of the FFMTs along the direction of the field compared to the corresponding reference sample. The area covered with tubes has two distinctive regions: the inner part, where alignment is more pronounced and outer part where tubes tend to align along the edge of the area (inner regions marked with blue squares and the outer with red ones on fig. 3.2). Such a difference in alignment behaviour between inner and outer areas of the sample can be caused by the surface tension force and interaction between the tubes. Both of these effects appear to have more influence on the orientation of the tubes than the magnetic field. This makes 100% alignment to be unreachable during water evaporation. Such a behavour was observed for all types of substrates: glass, silicon and mica.

To conclude this section it should be mentioned that due to the higher mobility, small FFMTs freely floating in solvent can be easily aligned by a magnetic field (with $\vec{B} \approx 1$ T). In the case of dropcasting, we observed less alignment, probably due to the influence of the surface tension during the evaporation process and interaction of the tubes with the substrate which disturbs a perfect alignment of the FFMTs.

3.3 Topography

In chapter 2 it was mentioned that for optical studies we used samples obtained

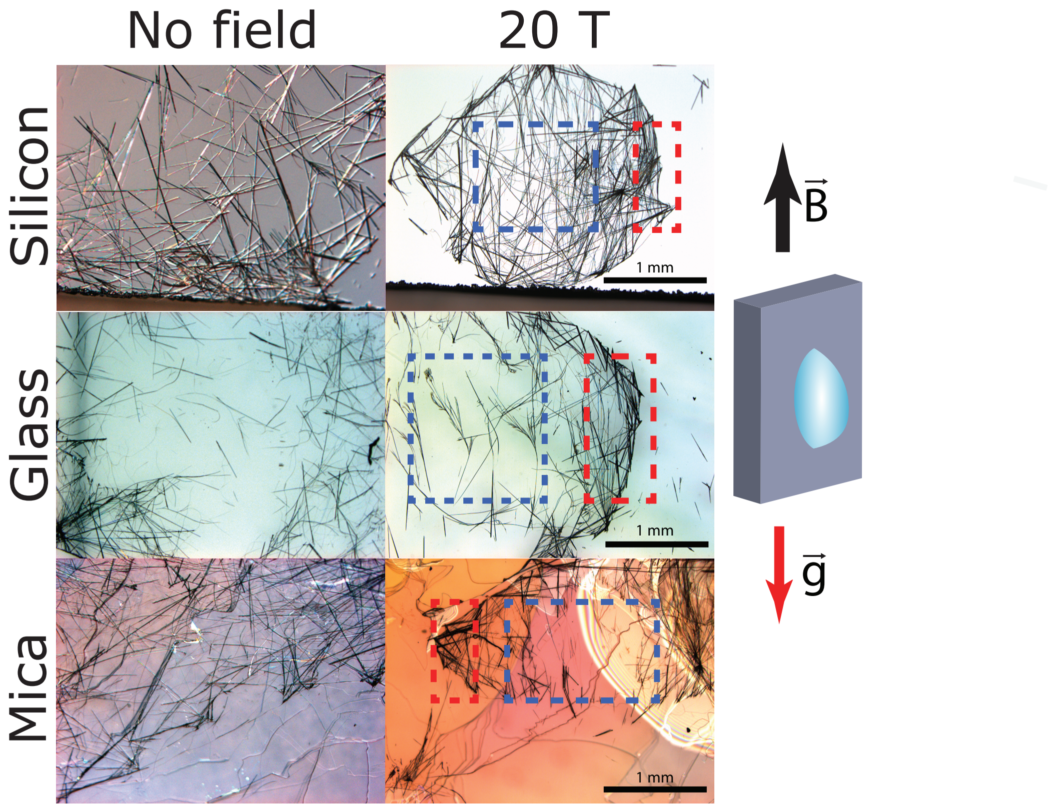

Figure 3.2: Optical micrograps of the peptide tubes samples dropcasted on 3 different substrates in the absence (left column) and presence of a 20 T magnetic field (right column). The black arrow shows the direction of the magnetic flux density $\vec{B}$, while the red one demonstrates the direction of the gravitational field $\vec{g}$. Blue squares depict the inner part of the droplet where alignment along the direction of the magnetic field can be seen, red squares highlight parts of the sample's outer area where alignment of the tubes deviates from the direction of the field and tends to follow the shape of the droplet.

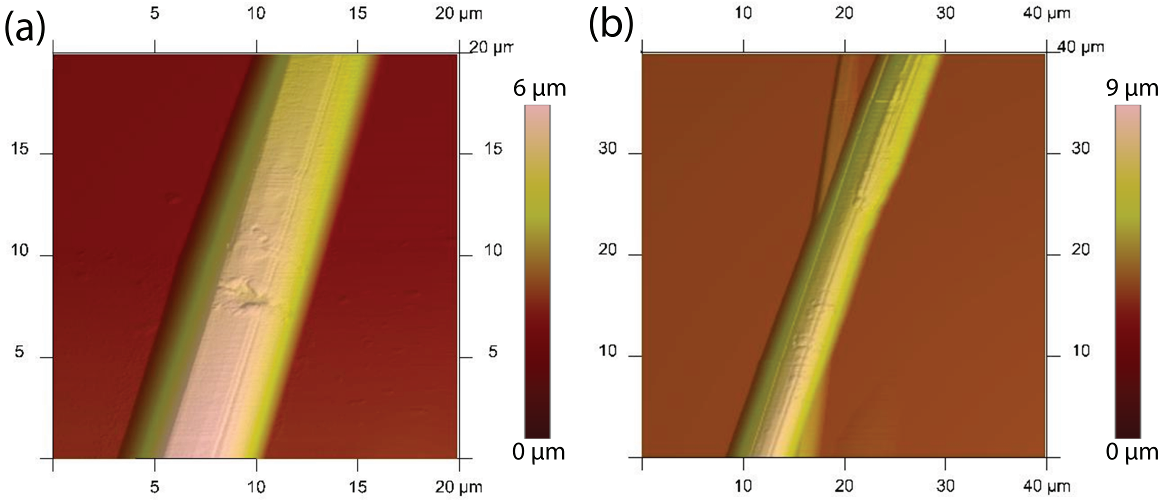

Figure 3.3: AFM images of FF peptide tubes on glass substrate. a) Image of the a single tube (image size 20×20 μm); b) Image of the crosspoint of two tubes (image size 40×40 μm).

from solutions with a concentration of about 0.2-0.5 mg/ml. We have performed studies of the topography of individual tubes in order to check if this fabrication process will result in uniform and long structures with the presence of central channels. The characterisation of topography and morphology of the peptide tubes was performed by atomic force microscopy (AFM) and confocal optical microscopy.

AFM studies confirm that an individual tube has a smooth uniform surface with the top surface roughness of $R_z = 32$ nm (see fig. 3.3). The surface does not show the presence of regular structures or nanotubes, which means that the tube is not a cluster of smaller objects. Fig.3.3(b) demonstrates that in the points of crossing tubes, they overlay and are not ingrown. The tube diameter on fig.3.3 is about 6 μm, which is typical for the tubes made from the used concentration.

After the evaporation process the tubes stick to the substrate and can not be moved freely. AFM scanning employs physical contact of the tip with the sample which makes possible a shift of the tubes with the cantilever. The AFM tip can bend a tube due to the applied force and does not break it, which is evidence of their high mechanical rigidity [11].

Confocal experiments were performed on the same region of the sample as the AFM studies. Images were obtained in two regimes of optical response: (1) the linear transmission regime, where the intensity of the transmitted light at 800 nm was detected and (2) the SHG regime where the transmitted SHG signal generated at 400 nm was detected. For the latter experiments a BG-39 filter was mounted in front of the detector to cut off the light at the 800 nm excitation.

The confocal image in transmission mode is shown on fig. 3.4 (a). Dark regions of the image correspond to areas of the sample with higher absorption. The central part of the tubes is brighter than the outer due to the higher absorption of the tube walls (see inset fig.3.4 (a)). The tubes show a uniform width and inner diameter in the range of one third of the outer diameter ($d_{inner} \approx 2$ μm). The confocal image (fig. 3.4(b)) registered at the SHG wavelength shows no hole structure compared with

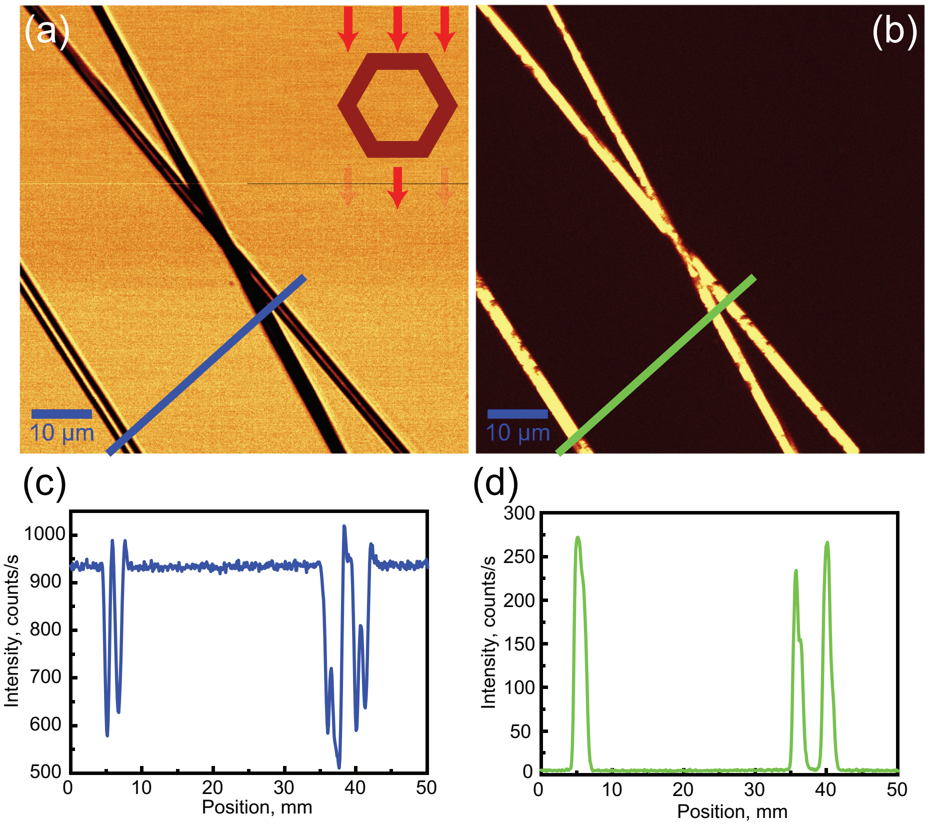

Figure 3.4: Confocal images of the peptide tubes; a) Confocal image obtained in transmission mode, excitation at 800 nm (dark regions correspond to areas with higher absorption, inset shows that walls have higher absorption); b) Confocal image obtained at SHG wavelength (400 nm)(dark regions correspond to the area with low SHG intensity); c) optical signal line traces of transmitted light at 800 nm (along blue line on fig. 3.4 a); d) SHG intensity line traces at 400 nm (along green line on fig. 3.4b). Comparison of the confocal images proves the presence of the the uniform channels inside the tube.

linear transmission experiment as the SHG response is generated on the surface; the bright regions correspond to the areas where the intensity of the generated SHG is higher. Signal cross-sections made for both images (Fig. 3.4 (b), (d)) show that the thickness of the tubes is 5 μm. This value is close to that was obtained with the AFM.

Both the confocal and AFM experiments demonstrate the uniform and smooth surfaces of the FFMTs. Confocal images (fig.3.4 (a), (c)) give further evidence for a uniform channel inside the FFMTs. The average outer diameter of the tube can be estimated as 5 μm, the diameter of the channel is about 2 μm.

3.4 Chirality and SHG properties of the FF tubes

Chirality is a structural property that can influence the optical properties of materials, both linear and nonlinear. Chirality describes the handedness of the object's structure, in other words: the shape of the mirror reflection of a chiral object does not coincide with the initial shape. Human hands are examples of such a geometrical objects.

The FF molecule has an intrinsic chirality originating from the molecule's geometry. Self-organised, FFMT inherits the chirality from the molecule, resulting in coil-like arrangements of the molecules inside individual tubes.

FFMTs have a hexagonal crystal structure with the $P6_1$ point group. The symmetry of the crystal allows to have the following independent nonzero components of the 2^nd order nonlinear susceptibility tensor for FFMT [12]: $\chi_{xxz} = \chi_{yyz}, \chi_{xzx} = \chi_{yzy}, \chi_{xyz} = -\chi_{yxz}, \chi_{xzy} = -\chi_{yzx}, \chi_{zxx} = \chi_{zyy}, \chi_{zzz}$. Components $\chi_{xyz} = -\chi_{yxz}, \chi_{xzy} = -\chi_{yzx}$ occur due to the chirality of the structure giving rise to the chiroptical properties of the nonlinear optical response.

In the general case, chirality can be observed in optical experiments resulting in such linear optical effects as circular dichroism (CD) and optical rotation (OR). Nonlinear optical effects can also be observed as the symmetry breaking due to the chirality of the structure causes additional non-zero components of the nonlinear tensor to appear. These nonlinear optical effects occurring in chiral materials are SHG circular dichroism(SHG-CD), SHG optical rotation (SHG-OR) and SHG linear dichroism (SHG-LD) effects. The SHG-CD effect can be described by the contrast of the SHG intensity for left and right circularly polarised excitation light:

$$SHG - CD = \frac{\Delta I(2\omega)}{I(2\omega)} = \frac{I_{LHC}(2\omega) - I_{RHC}(2\omega)}{I_{LHC}(2\omega) + I_{RHC}(2\omega)} \tag{3.1}$$

where $I(2\omega)$ is the intensity of light at the doubled frequency (SHG). RHC and LHC superscripts related to right-hand and left-hand circularly polarized light, respectively. This value allows to estimate the difference in the SHG for light with opposite handedness. In practice, we can perform the experiment with a continuously rotating $\lambda/4$ plate. These polarisation measurements give information about the relation of the nonlinear susceptibility tensors, but also includes information about SHG-CD.

To address the nonlinear optical response of FFMT's we have performed several polarisation measurements (fixed sample and output polarisation, input polariser was rotated) for different orientations of the tube with respect to the plane of incidence. The scheme of the experiments and their results are shown in fig. 3.5.

During the experiment a $\lambda/4$ plate was constantly rotated, which resulted in a change of the light polarisation state from linear to circularly polarized. The waveplate 0° position corresponds to p-in, 90° -to s-in, 45° and 135° to σ^+ and σ^- circularly polarized light respectively. The experiment was conducted for p- and s-out polarisation configurations (fig. 3.5 (a),(b) and (c), (d), respectively). Each plot shows normalised SHG intensities results obtained for two orientation of the tube rotated by 180°. The tube was aligned parallel or perpendicular to the plane of incidence. The shape of the signal for all measurements is not symmetric with respect to a 180° rotation, which is a clear evidence of the chiral response form the material. Dots corresponds to the experimental data, while lines to the fits to the following formula [13]:

$$\begin{gathered} I_{2\omega}(\varphi) = A((f_1 - g_1 + 4f_2\cos(2\varphi) - (f_1 - g_1)\cos(4\varphi) + 2h_2\sin(2\varphi) - h_1\sin(4\varphi))^2 + \\ (f_2 - g_2 - 4f_1\cos(2\varphi) - (f_2 - g_2)\cos(4\varphi) - 2h_1\sin(2\varphi) - h_2\sin(4\varphi))^2) \end{gathered} \tag{3.2}$$

		0°	180°	90°	-90°
p-out	f	$-0.116-0.034i$	$-0.069-0.015i$	$0.078-0.030i$	$0.003+0.087i$
	g	$0.052+0.042i$	$0.047+0.014i$	$-0.062-0.205i$	$-0.143-0.216i$
	h	-0.377	-0.454	0.296	0.148
s-out	f	$-0.138-0.004i$	$-0.074-0.006i$	$0.064+0.015i$	$0.077-0.050i$
	g	$0.073-0.030i$	$0.048+0.014i$	$-0.212+0.143i$	$-0.288_{0}.107i$
	h	0.381	-0.459	0.286	0.178

Table 3.1: Values of the fit parameters obtained from eq.3.2 for p- and s- output polarisation . The f, g, h parameters are not equal for the opposite orientations of the FF-tube(-90° and 90 °, 0° and 180°). A non-zero parameter g is evidence of an additional contribution to the SHG signal from magneto-dipole and electro-quadruple terms.

	0°	180°	90°	-90°
p-out	-0.124	-0.179	0.195	-0.702
s-out	-0.007	-0.078	-0.135	-0.114

Table 3.2: Values of SHG-Cd contrast $\frac{\Delta I(2\omega)}{I(2\omega)}$ for p- and s- polarised output for the opposite orientations of the FF- tube. Chiral contrast is not equal for the opposite orientations of the FF-tube (-90° and 90°, 0° and 180°)

where the parameters f, g, h describe a combination of nonzero components of the nonlinear optical tensor. For the reflection geometry these have the following form[13]:

$$\begin{aligned}
f_s^R &= -\sin\theta(-2\chi_{xyz}^{eee}\cos\theta - \chi_{xzx}^{eem} + \chi_{zzz}^{mee}\mathrm{sin}^2\theta + \chi_{zxx}^{mee}\mathrm{cos}^2\theta - 2\chi_{xxz}^{mee}\mathrm{cos}^2\theta)\\
g_s^R &= -\sin\theta(\chi_{xxz}^{eee} + \chi_{zxx}^{mee})\\
h_s^R &= \sin\theta(2\chi_{xxz}^{eee} - (\chi_{xyz}^{eem} + \chi_{xyz}^{eem})\cos\theta - 2\chi_{xyz}^{mee}\cos\theta)\\
f_p^R &= \sin\theta(\chi_{zzz}^{eee}\mathrm{sin}^2\theta + \chi_{zxx}^{eee}\mathrm{cos}^2\theta - 2\chi_{xxz}^{eee}\mathrm{cos}^2\theta + \chi_{xzy}^{eem}\mathrm{cos}\theta + 2\chi_{xyz}^{mee}\cos\theta)\\
g_p^R &= \sin\theta(\chi_{zxx}^{eee} - \chi_{zxy}^{eem}\mathrm{cos}\theta - \chi_{xyz}^{eem}cos\theta)\\
h_p^R &= -\sin\theta(-2\chi_{xyz}^{eee}\cos + (\chi_{zzz}^{eem} - \chi_{zxx}^{eem})\mathrm{sin}^2\theta - (\chi_{xzx}^{eem} + \chi_{xxz}^{eem})\mathrm{cos}^2\theta - 2\chi_{xxz}^{mee}\cos\theta)
\end{aligned} \tag{3.3}$$

where the R superscript corresponds to the reflection geometry, p and s subscripts correspond to p-out and s-out polarisation, respectively. Every fit parameter is a complex number, so the superscripts 1 and 2 are the real and imaginary part of the corresponding fit parameter, respectively. A is the relative intensity of the signal. All the parameters of the fits obtained from the experimental data are listed in Table 3.1. The nonzero values of the parameter g in the table 3.1 is evidence that the SHG signal can not be described only in the electro-dipole approximation but also magneto-dipole and electro-quadruple contributions should be taken into account [13].

Experimental data allows to estimate the SHG-CD effect in FF microtubes. Results are presented in table 3.2. Results show that this effect is stronger when the tube is aligned along the plane of incidence.

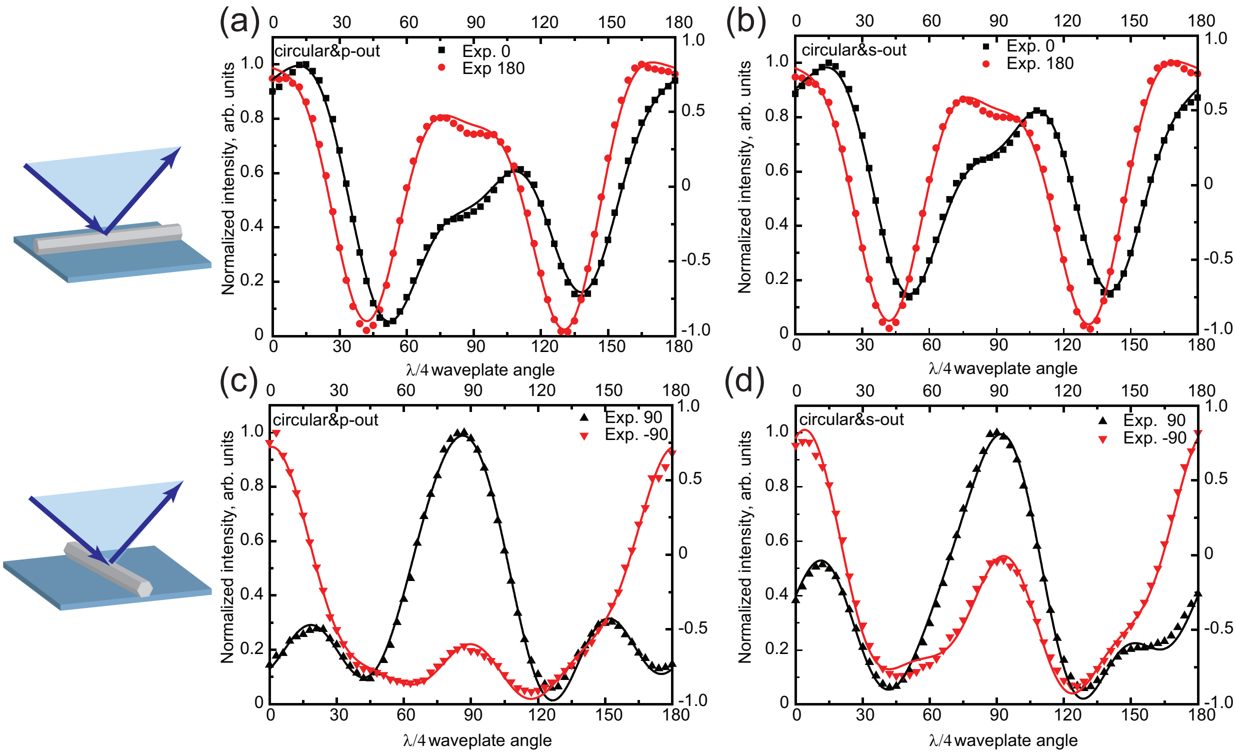

Figure 3.5: Scheme of the experiment and normalised SHG intensity as function of orientation of input $\lambda/4$ plate; Data for tube perpendicular to the plane of incidence for (a) p-out and (b) s-out; Data for tube parallel to the plane of incidence (c) for p-out and (d) s-out. Black and red solid lines are fits, see Eq. 3.2. Note that each plot shows the data for the tube rotated 180° in the plane of the sample.

3.5 Estimation of the value of the non-linear susceptibility

To obtain an estimation of the nonlinear susceptibility of the peptide tubes a standard approach based on comparison with a reference sample (quartz plate) was used.

For SHG calibration, a two-side polished z-cut quartz plate was used with its azimuthal orientation providing the maximal SHG signal in the *p*-in, *p*-out polarisation combination. Only the signal generated from the top surface was detected.

The value of the effective χ_{FFMT} was estimated from the coherent SHG signal [14]:

$$\chi_{FFMT} = \chi_{quartz} \left(\frac{I_{FFMT}}{I_Q}\right)^{1/2} \left(\frac{l_{quartz}}{l_{FFMT}}\right) \tag{3.4}$$

where I_{FFMT} and I_Q are the SHG intensities from FFMTs and quartz crystal, l_{quartz} and l_{FFMT} are the FFMT and quartz coherence length, and χ_{quartz} is the effective value of the quartz susceptibility (in which the experimental geometrical factors are taken into account), respectively. The coherence length in this reflection geometry is determined by $l_{coh.} = \lambda_\omega/4(n_\omega + n_{2\omega})$. For quartz at $\lambda_{ex.} = 960$ nm, $n_\omega = 1.451$ and $n_{2\omega} = 1.463$ this gives $l_{coh.}$= 82 nm.

The exact refractive index of the FFMTs is unknown, however the refractive index for organic materials is usually in the range of 1.4-1.8 [15]. The size of the peptide tubes does not allow to perform optical characterisation on a single tube; at the same time the distribution of the FFMTs gives rise to huge scattering which makes measuring the refractive index of FFMTs a difficult task with the standard ellipsometry technique.

We have performed an experiment which allowed us to roughly estimate the index of refraction within a mentioned range of indexes. It is based on using a liquid which has a matching refractive index. This approach is very old and was already used for mineralogy [16]. We used liquids with the index of refraction ranging between n $= 1.33 - 1.6585$. If the $n_{liquid} \approx n_{mat}$ the material should be hardly distinguishable or invisible in the surrounding liquid. The best results were observed for bromonaphthalene (Sigma-Aldrich) with index of refraction n = 1.6585. However, the matching was not ideal as tubes were slightly visible but these results were much better than for other liquids used. Due to this rough estimations we conclude that FF tubes refractive index is about of $\mathrm{n}_{FF} \approx 1.66$.

From the obtained index of refraction we estimate that the coherence length is in the range of 70-80 nm, which is similar to that of quartz. The average signal from the tubes was about 500 times higher than from quartz, however, in some places the signal was about 3000 times higher. Rough scanning and the presence of defects are among the possible reasons for such a difference. The value of $\chi_{quartz} = 1$ pm/V, so we can estimate value of $\chi_{FFMT} = 25 \pm 10$ pm/V. Comparing this value with biological structures, like collagen fibrils ($\chi_{cf} = 0.4$ pm/V) or even inorganic nonlinear optical materials LiNbO3 ($\chi_{\mathrm{LiNbO_3}} = 21$ pm/V)[ref] allow us to conclude that the value of χ_{FFMT} is very high, indeed, though the error bars are large.

3.6 SHG as probe of a structural phase transition

The strong SHG response of the FFMT's occurs due to the noncentrosymmetric arrangement of the FF molecules. The structure of the peptide tubes consist of FF molecules but in addition to them there are water molecules caged inside the molecular coils. One turn of the molecular coil consisting of six FF and nine water molecules can be defined as a "supercell" [17](more details on the supercell structure can be found in chapter 2). The amount of the water molecules inside this "supercell" can be changed by heating and influences both the linear and nonlinear optical properties.

SHG is a two photon process, so the study of the SHG response of materials usually includes the measurement of its power dependence. We performed such an experiment and observed that at low power the as-grown FFMTs produce strong SHG, which up to a critical value follows the expected quadratic power law (see fig. 3.6). When the laser fluence reaches the value of $I_\omega = I_\omega^{crit,1}$, the slope of $I_{2\omega}$ strongly deviates from quadratic. This deviation can be assigned to the phase transition from a noncentrosymmetric to a centrosymmetric phase described in details in chapter 2 [3; 18]. Simultaneously, the TPL signal appears and increases exponentially (see fig. 3.6, red dots). After the power reaches another critical value $I_\omega = I_\omega^{crit,2}$, both signals start to decrease. This appears to correspond to a changing of the shape of the tubes up to melting. The morphology of the tubes does not change at $I_\omega = I_\omega^{crit,1}$ and we consider the phase of the tubes in this power range as annealed.

Our SHG set-up allows to perform nonlinear microscopy as we can scan the sample, and therefore detect the spatial distribution of the nonlinear optical response at different wavelengths. Figure 3.7 shows a nonlinear optical image of the sample, part of which was locally heated with the laser. Panel (a) shows a SHG map (collected at 400 nm). Panel (b) represents a TPL map (collected at 550 nm) of the very same part of the sample. The region marked with dashed lines was treated by laser radiation, resulting in the phase transition of the FFMTs located in this area. Images on panels (a) and (b) of fig. 3.7 are complementary of each other, as SHG and TPL signals are mutually exclusive. The part of the sample with higher SHG has no TPL signal, as no phase transition was occurred in this area. Similarly, the sample areas with high TPL signals demonstrate no SHG response.

In order to show that the observed behaviour of SHG and TPL can indeed be connected to the structural phase transition, we measured the SHG and TPL signal generated by the FFMT at different temperatures of the sample. To perform these experiments, a heater was mounted on the scanning stage of the SHG set-up. The freshly made FFMT sample was mounted on a heater which allows to control the sample temperature from room temperature up to 200 °C. The heat expansion of the sample holder leads to a shift of the sample and therefore the tube position. In order to reduce the influence of these shifts we have performed 2D intensity scans for every temperature step. At lower temperatures (< 100 °C) the scans were done at 400 nm to detect the SHG signal, and at higher temperatures (> 100 °C) scans at 550 nm were used to select the TPL signal as it gave more contrast (similar to fig. 3.7a b). 2D scans ensure that the signal was not changed by sample movement and was fully related to the structural changes of the sample. After the 2D map was recorded the

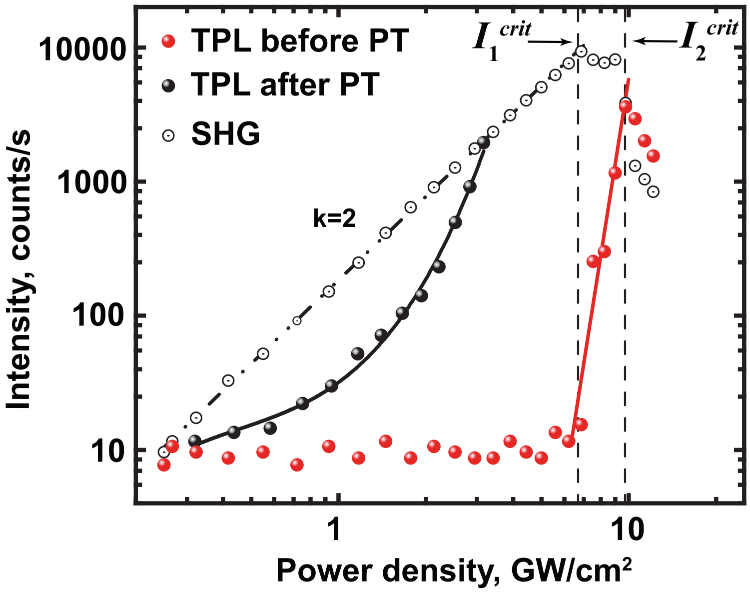

Figure 3.6: Dependence of the SHG and TPL intensity on the incident laser (800 nm) power density. Black open circles demonstrate the intensity of the SHG signal which is linear (in log-log scale) with the slope of 2 and originates from the two-photon nature of the SHG harmonic generation. $I^{crit}{}_1$ is the laser power where the SHG stops to grow and the TPL signal (red dots) demonstrates a sharp increase. TPL is also a two photon process, but its faster growth (slope more than 2) can be related to the phase transformation (PT). Black dots correspond to the second measurements of the TPL power dependence on the same spot after the PT occurred. The growth of the TPL intensity is exponential in this case, which can be related to some superluminescence/amplification process.

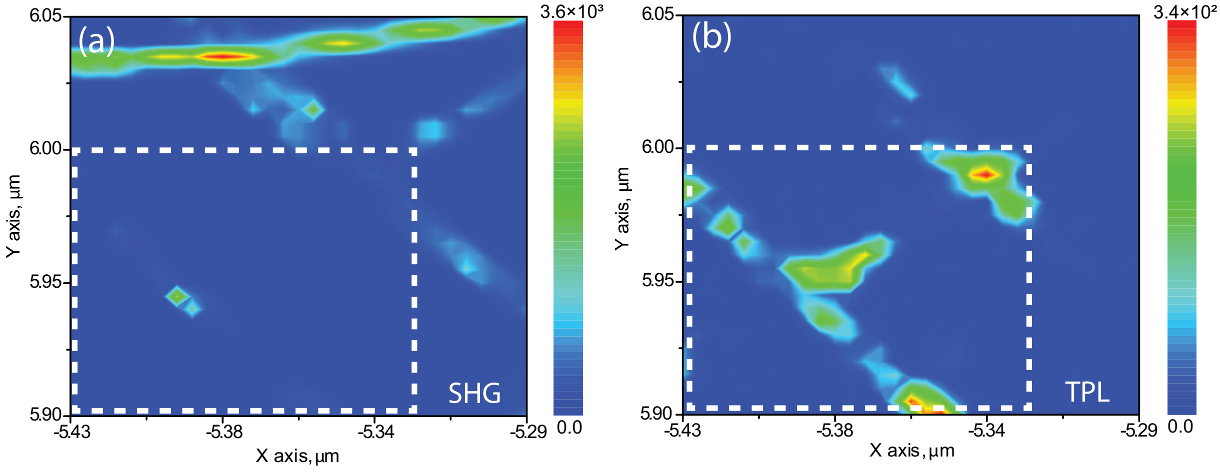

Figure 3.7: Map of nonlinear optical response collected at different wavelength for the same area of the sample for 800 nm excitation; (a) SHG map (collected at 400 nm), region inside the area marked with dashed line was treated by laser; (b) TPL map (collected at 550 nm). These images are complementary to each other, as the SHG and TPL signals are mutually exclusive, due to the phase transition.

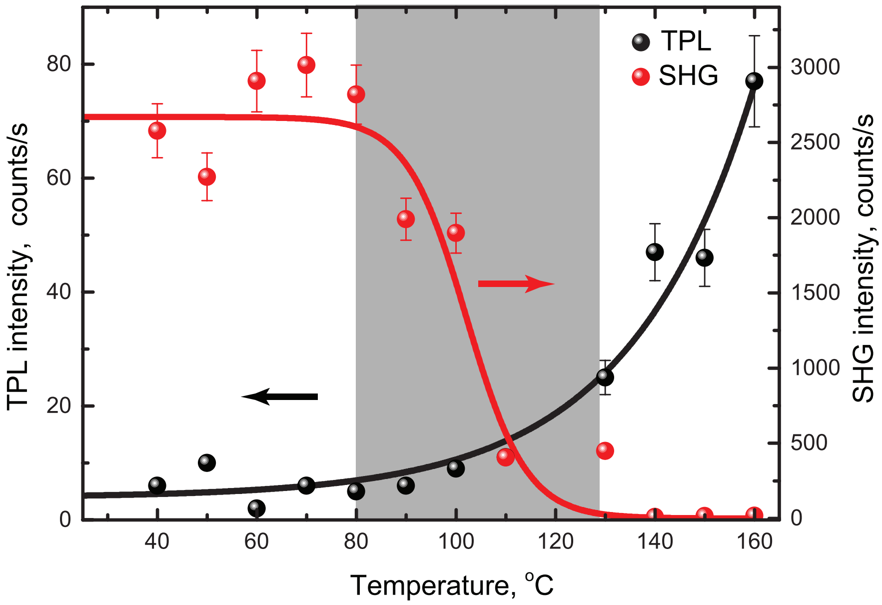

Figure 3.8: Modification of the SHG and TPL signal with increasing temperature. Gray area depict the temperature range where SHG undergoes decrease. Dots corresponds to the experimental data, while lines are the guides to the eye.

generated emission spectra were registered. Then the temperature was increased by 10 °C and the whole procedure was repeated. Unfortunately such approach does not allow us to track changes of the nonlinear response in real-time as it was done for power dependence measurements.

Results of these experiments are summarized in fig.3.8, where the SHG and TPL spectral components are plotted as a function of heater temperature. The SHG signal (red dots) was high until 70 °C as freshly made peptide tubes are noncentrosymmetric. After the temperature of 70 °C, the SHG signal started to decrease until a minimum value was reached at 140 °C (marked with the grey area on fig.3.8). At the same time the TPL signal (black dots) behaves completely different. At temperatures lower than 100 °C no TPL signal was detectable, as the value of 10 counts/s was the level of the background noise. Above 100 °C the TPL signal drastically increased. The sharp decrease of SHG can be attributed to the phase transition appearing, while the appearance of the TPL is surprising.

The obtained results demonstrate, that both increased laser power and sample temperature lead to the appearance of the TPL, so we may conclude that similar processes occur in the sample and the phase transition can be triggered both with a laser and heat.

We used differential scanning calorimetry (DSC) to have an independent correlation of the temperature induced phase transition. DSC is a thermal analysis technique which is widely used for the investigation of the thermal properties of materials [19]. It determines the temperature and heat flow which are correlated with phase transitions as function of time and temperature. A DSC set-up measures the quantity of heat, which is radiated of absorbed by the sample during a change in temperature compared to a reference sample. This technique is widely applied for investigations of phase transitions during biochemical reactions, i.e molecular transitions of a molecule from one conformation to another.

The DCS measurements were conducted with a PYRIS Diamond DSC (Perkin-Elmer). The FF tube samples for this measurements were prepared with a higher concentration (10 mg/ml) of stock solution than for optical measurements (0.5 mg/ml) to increase the amount of formed tubes left after evaporation of the solvent. After the drying of the sample, the formed tubes were removed from the substrate and approximately 3.5 mg of microtubes were placed in a metal container for DSC measurements. The empty metal container was used as a reference sample. Measurements were performed in the range of 30 to 230 °C with the heating speed of 5 K/min. Unfortunately this heating rate is not achievable during our optical experiments when we heat the sample and track its non-linear optical response where we need to wait until the sample will be scanned. This consideration makes DSC measurement to be more sensitive to temperature changes. Comparison of our DCS data with data obtained by nuclear magnetic resonance (NMR), XRD and thermal gravimetric analysis (TGA) gives an understanding what happens with the internal structure of FFMT during heating [1; 18; 20].

Figure 3.9 shows the DSC trace of the FF peptide tubes, which consist of three distinctive regions which can be attributed to physical or chemical process. The temperature region from 30 to 110 °C can be related to the process of the evaporation of the water molecules from the hydrophilic channel (region (a) in fig. 3.9). The narrow dip around 135 °C also represents the evaporation of the stronger bound water molecules, as extra energy is needed to remove them from the crystalline structure (region (b) in fig.3.9). The dehydration in this temperature region was shown by *Jaworska et al.* by intensity changes of ^{1}H NMR spectra, where the intensity of the hydrogen resonance peak allows to track the amount of water inside the peptide tube. The last region of the DSC trace (region (c) in fig. 3.9) can be attributed to the molecular transformation from the linear to cyclic form of the peptide as this molecular transformation was detected by changes of the resonance positions for ^{13}C NMR spectra [18]. The resonance peak induced by carbon belonging to the carboxilic group disappeared, proving the peptide cyclisation process.

Analysis of the DSC signal and reported NMR, XRD and TGA data allows us to conclude that heating of FFMT induces a phase transition, which can occur due to dehydration and molecular transformation. This phase transition results in the observed changes of the nonlinear optical signals.

We compare the results of the temperature dependent SHG/TPL measurements(fig. 3.8) and the DSC results (fig. 3.9). All of these experiments demonstrate thermally induced changes and the analysis of the data allows us to clarify the reason of the changes in the optical properties of the FFMTs.

The SHG signal is high up to 80 °C, which means that the crystal lattice is stable (noncentrosymmetric)(fig. 3.8). At the same time the DSC trace demonstrates a minimum in this range related to the water loss (region (a) of fig.3.9). Both of these facts mean that water loss is not sufficient to introduce changes to the crystal lattice at temperatures lower than 80 °C, while at higher temperatures the crystal structure of FFMT can be distorted due to the lack of water molecules inside the FFMT. The decrease of the SHG signal continues until the temperature of 130 °C (region (b) of

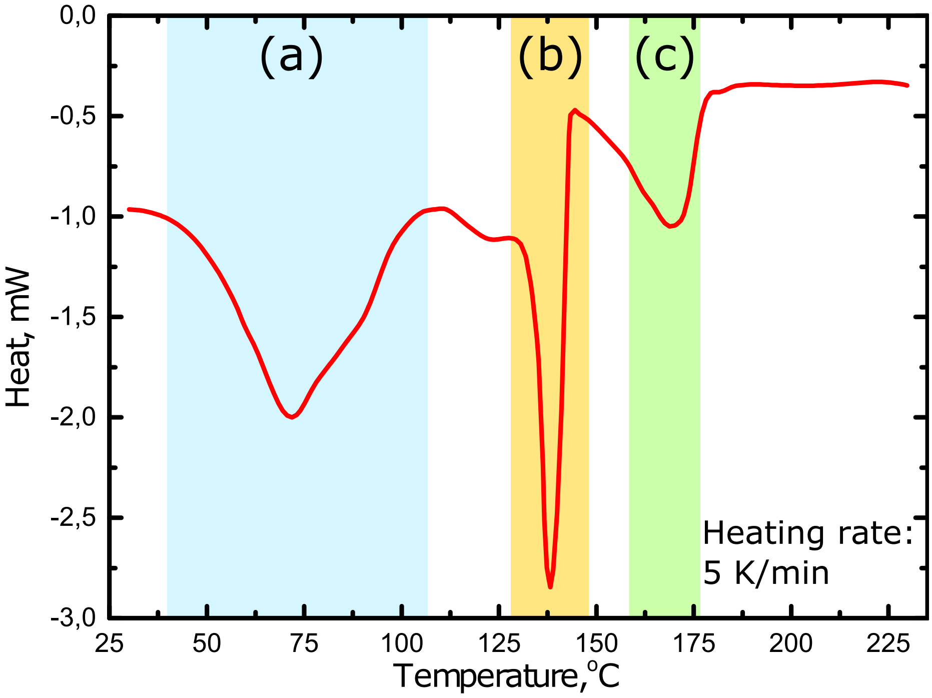

Figure 3.9: Differential scanning calorimetry (DSC) trace of the FF-peptide tubes. Region (a) corresponds to the water removal; region (b) corresponds to the removal of bound water; region (c) corresponds to the molecular transformation.

fig.3.9) where the SHG signal completely disappeared, demonstrating that the crystal lattice symmetry of the tube can not sustain SHG and thus became centrosymmetric. Thus, the temperature dependence of the SHG signal and its decrease can be explained by the mobility of the water molecules inside the FFMT and a distortion of the crystal lattice and its transformation from hexagonal to orthorhombic due to the water evaporation. The appearance and growth of the TPL signal happens for temperatures higher than 120 °C, where water should be removed from the FFMT and a molecular transformation occurs.

The origin of the appeared TPL is unclear, as no new chemical compounds were fabricated. Molecular transformation can not be the reason of the the TPL appearance as the cyclic form of FF peptide has approximately the same π-conjugation length as the linear form, and should not give any response in the visible spectral range. The possible reason can be related to the water containing “supercell”, where collective interactions of peptide and water molecules can lead to the formation of excitons [21]. It is known that the amount of water molecules changes the optical properties of FFMT in the linear regime [20]. Wang et. al. have shown that the content of water molecules in the FFMTs core modifies the bandgap of the “supercell” and, consequently, the PL spectrum profile changes. In particular they observed that the addition of water molecules causes a redshift of the characteristic peak, also confirmed by density functional theory calculations. The presented density of states (DOS) shows not only a splitting of the valence band at about 3 eV, but also the presence of a feature located around 2-2.5 eV, which also redshifts by increasing the core-tubes water content. Although Wang and coworkers do not mention the origin of this feature of the DOS, the theoretical prediction of such electron transitions can be a starting point to clarify the origin of our characteristic FMMTs PL peak in the green region between 425 and 600 nm (2-3 eV).

The processes of water evaporation and molecular transformation influence the morphology of the sample. Scanning electron microscopy was used to investigate the morphology of the peptide tubes before and after the phase transition. Freshly made peptide tubes show smooth surfaces of the facets seen on SEM . Laser treatment locally destroys the upper wall of the tube. The place of laser illumination is surrounded with a melted substance due to the laser impact (fig. 3.10(a), melted area marked with red arrow). Control of the laser power can avoid destruction of the wall and just slightly melt it (fig. 3.10(b)), place of laser impact is marked with the arrow). As the treatment was local, all the rest of the tube was found to be undamaged as no visible changes are observable.

Treatment with high temperatures had a completely different effect on the structure. Annealing at 150 °C for 1 hour in an oven in air environment made the surface of the peptide tube rough and broke it into smaller fibres with lengths of hundreds of nanometres and diameters of tens of nanometres (fig. 3.10(c)). Despite well pronounced morphology changes the tubular shape is kept stable, and the channels are still visible (fig. 3.10(d), channel position is marked with arrow). Both the laser and temperature treatment do not influence the tubular structure of the object.

3.7 Two-photon luminescence

The phase transition of the FFMT's from hexagonal to orthorhombic crystal lattice results in the appearance of luminescence in the green spectral range (maximum around 530 nm). We studied SPL and TPL in as-grown and in annealed samples, the latter by heating in an oven and/or locally heated by a laser (see fig.3.10, 3.11(a)). Spectra of oven and laser heated FFMTs are similar as well as the phase transition behaviour. For as-grown FFMTs the SPL spectrum reveals a wide asymmetric peak with a maximum around 550 nm (2.25 eV). For oven-heated FF microtubes the SPL intensity increases 75 times and the maximum is shifted to 560 nm. Deconvolution by gaussian distributions gives $E_{SPL1} = 560$ nm (2.2 eV) and $E_{SPL2} = 492$ nm (2.52 eV). The heated microtubes in fig. 3.10 were heated up to 150°C which brings them to the phase between the structural phase transition and cyclization of the FF-peptide molecules. Since FF molecules in linear form or cyclic form (diketopiperazine (DKP), more about molecule transformation can be found in subsect.1.2.3) and FF-DKP microtubes formed directly from DKP do not show SPL in the green spectral range, heating by oven or laser in air plays a significant role in the SPL appearance.

The as-grown FFMTs do not produce a two-photon luminescence if excited in the range of 700-1000 nm, but generate strong SHG signals (not heated areas of fig. 3.7 (a)). In contrast, the heated FFMTs generate strong TPL and negligible SHG. Figure 3.7 (b) shows the TPL signal map with the pump at 800 nm. Note, that this TPL appears for laser fluences below a critical value. Since this TPL appears under conditions quite similar to SPL, we assume that they have the same origin.

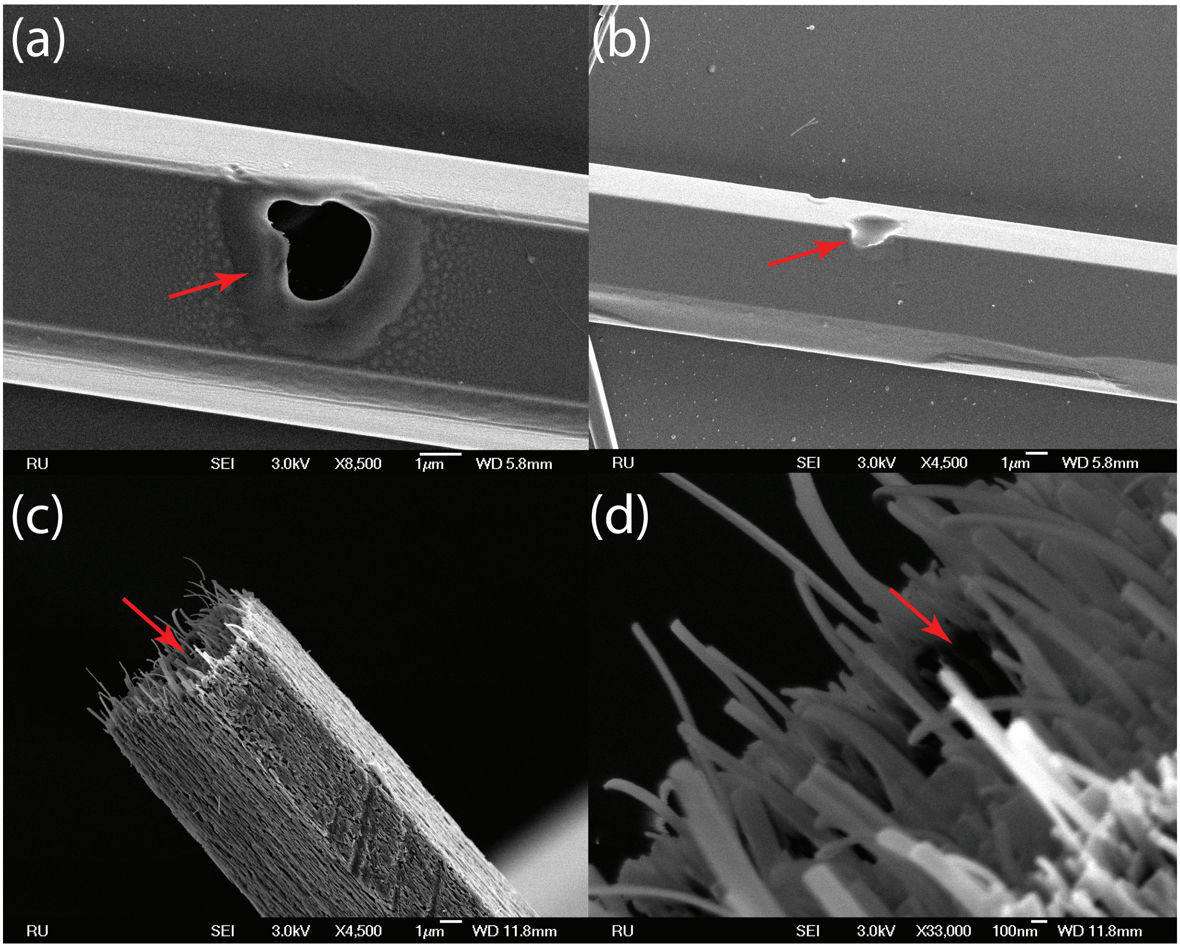

Figure 3.10: SEM images of the peptide microtubes after different types of heat treatment. (a) Laser heated tube, the power of the laser was high, resulting in the hole appearance in the wall of the tube. Red arrow marks melted area around the burned hole; (b) Tube heated with the laser at smaller power than that shown on panel (a). Damage from the laser impact is less pronounced in this case. Red arrow show the place of laser impact; (c) Tube heated in the oven at a temperature of 150 °C, arrow marks the position of the central channel; (d) Zoomed image of the tube heated in the oven. The channel inside the tube can still be seen after the phase transition (marked with arrow).

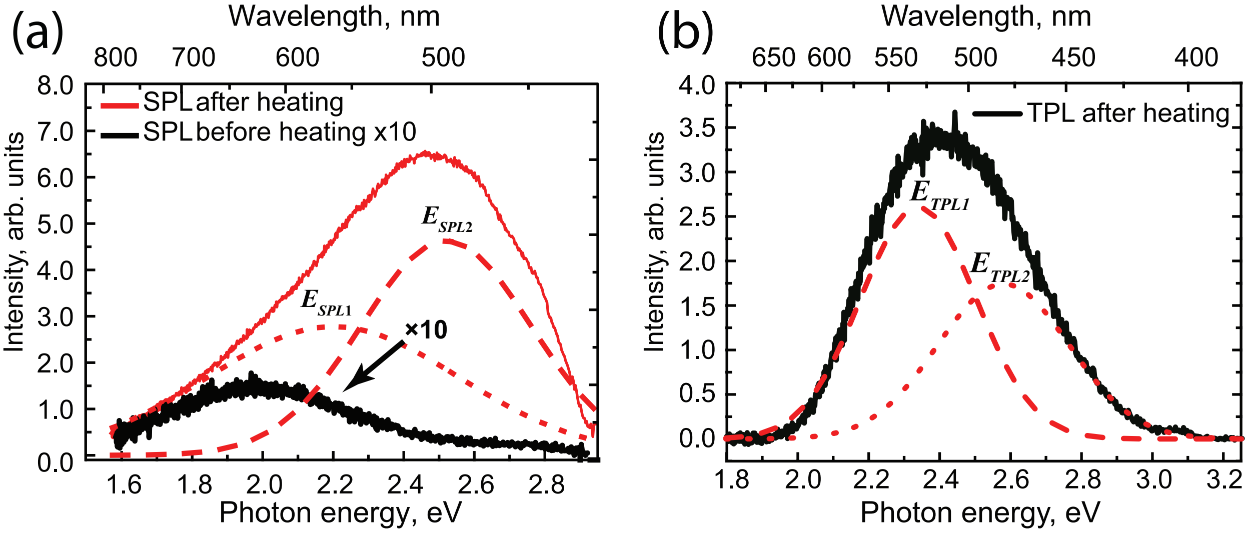

Figure 3.11: (a) Single photon luminescence excited at 400 nm spectral response in the sample before (black curve) and after (red curve) heating in the oven; (b)Two-photon luminescence from the heated sample excited at 800 nm. Dotted lines represent Gaussian deconvolution of the luminescence spectra

It was already shown that the phase transition to the orthorhombic phase is irreversible: after the FFMT is cooled down to room temperature, the TPL appears at very low laser power and there is no observable SHG [2; 3]. Now intensity of the TPL signal $I^{TPL}(I_\omega)$ increases exponentially with intensity of excitation light I_ω, i.e. much faster than the quadratic dependence expected for ordinary TPL. $I^{TPL}(I_\omega)$ is also completely reversible (fig. 3.6, black dots).

Comparison between the two-photon processes of the oven-heated and laser-heated FF mictrotubes shows that in both cases the spectra are quite similar: they both consist of two parts: SHG and TPL, with the TPL spectra showing two maxima around $E_{TPL1} = 540$ nm (2.3 eV) and $E_{TPL2} = 476$ nm (2.6 eV).

Both TPL and SHG contributions can be observed in a wide range of excitation wavelengths, demonstrating a broad tunability of the material (fig. 3.12).

Despite the fact that an FF-molecule produces luminescence in the UV range due to the aromatic rings, the aggregation of the FF-molecules to the watercontaining "supercell" leads to a strong modification of the UV spectra. The amount of the water molecules strongly affects the position of the UV PL peak (see fig. 3.13). This is caused by the variation of the density of states (DOS) in the "supercell" upon removal of H_2O [20]. The calculated DOS allows transitions not only between states corresponding to the UV photons, but also predicts transitions for the photons in the green range (≈ 540 nm $= 2.3$ eV) which we observe in our work.

In order to understand the nature of the photoluminescence in the annealed FFMTs, we performed excitation and time-resolved TPL measurements. To perform time-resolved measurements a pulse-picker (OG8/1, Avesta Project) was introduced into the optical set-up before the focusing lens. It allowed to reduce the frequency of the laser from 82 MHz to 1 KHz and it was synchronized with the photon counter. The photon counter was switched into the gated regime which allowed to reconstruct the time

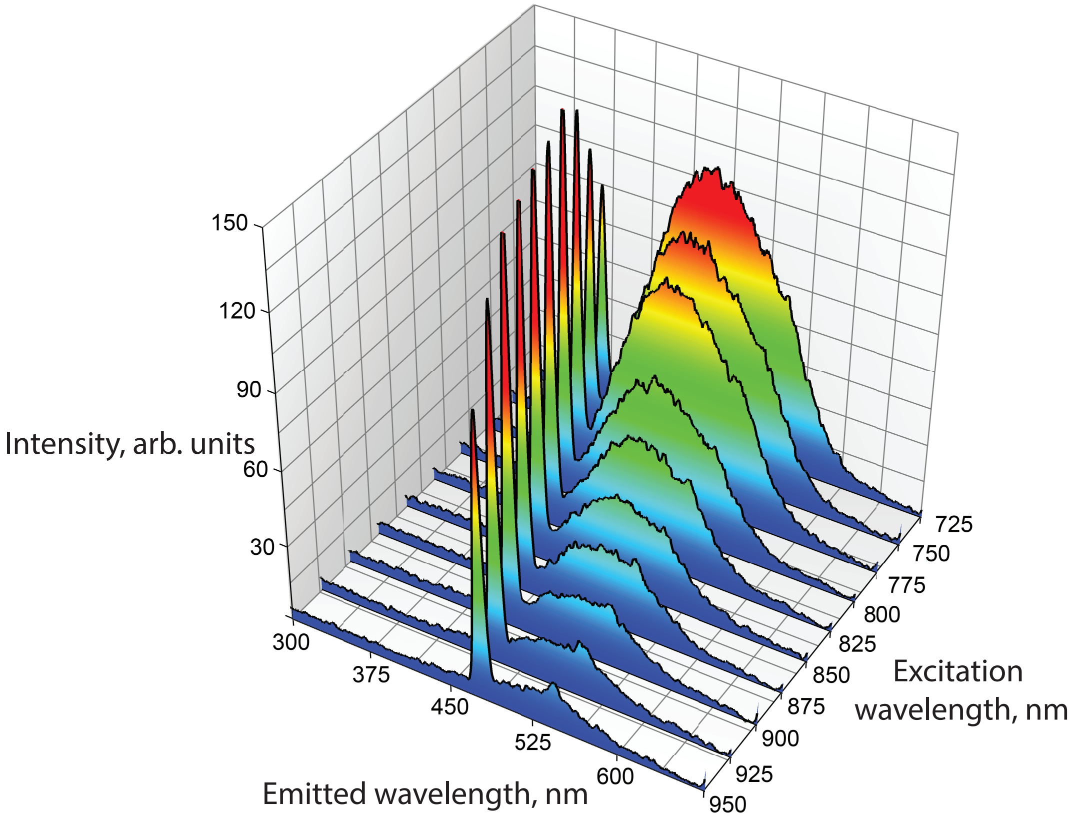

Figure 3.12: Tunability of the nonlinear response from the FFMT's. The narrow peak corresponds to the SHG signal, while the broad peak represents the TPL. Change of the excitation wavelength gives a response of both SHG and TPL wavelengths in the whole range of the excitation laser.

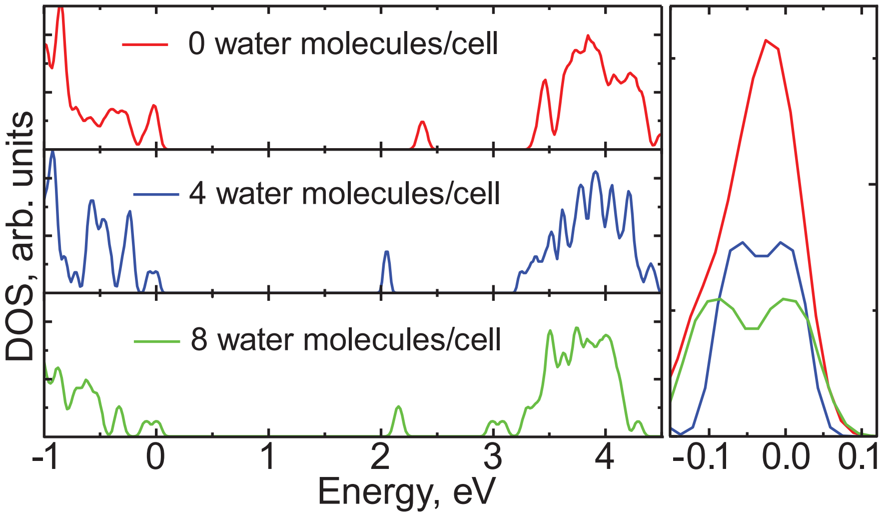

Figure 3.13: Left: DOS of FF PNTs with 0, 4, and 8 water molecules per supercell. Right: enlarged valence band maximum (VBM) region located around 0 eV. Splitting of the VBM due to incorporation of water molecules can be clearly seen and it leads to splitting of the PL peak observed in our experiments. Note the presence of the additional peak around 2-2.5 eV. Reprinted with permission from [20]. Copyright 2011 WILEY-VCH.

profile of luminescence signal by changing the delay between gate and synchronisation pulse.

The results of the excitation spectra are presented in fig. 3.14 (a). The SPL excitation spectrum possesses a maximum at 413 nm (3 eV), whereas the TPL intensity increases up to the edge of the laser tunable range, to 375 nm (3.3 eV). The width of the spectra and their asymmetry suggest that the two-photon excited emission process takes place under conditions of strong exciton-vibronic interactions (as an example, the symmetric phenyl breathing mode is included in fig. 3.15) [22]. The TPL signal decays very fast: the relaxation time is about or less than 5 ns (which is the temporal resolution of our set-up) (3.14 (b)). Such a fast process of radiative relaxation can be attributed to the singlet to singlet transition (fluorescence).

Comparison of the spectra for SPL and TPL demonstrates the different shape of the observed signals. Both of them have the same two spectral components, however the ratio of their intensities is different for single and two-photon excitation (fig. 3.11). In order to explain the redistribution of the peak intensities for SPL and TPL, the following process is proposed (fig. 3.15). The ground state adiabatic potential can be described by [23]:

$$U_0 = \frac{\hbar\omega}{2} q^2 \tag{3.5}$$

where $\hbar\omega$ is the energy of a vibrational quantum. The expression for both excited states can be described as follows [23]:

$$\begin{aligned} U_1 &= \frac{\hbar\omega}{2} {q_1}^2 + \Delta_1 + \nu_1 q \\ U_2 &= \frac{\hbar\omega}{2} {q_2}^2 + \Delta_2 + \nu_2 q \end{aligned} \tag{3.6}$$

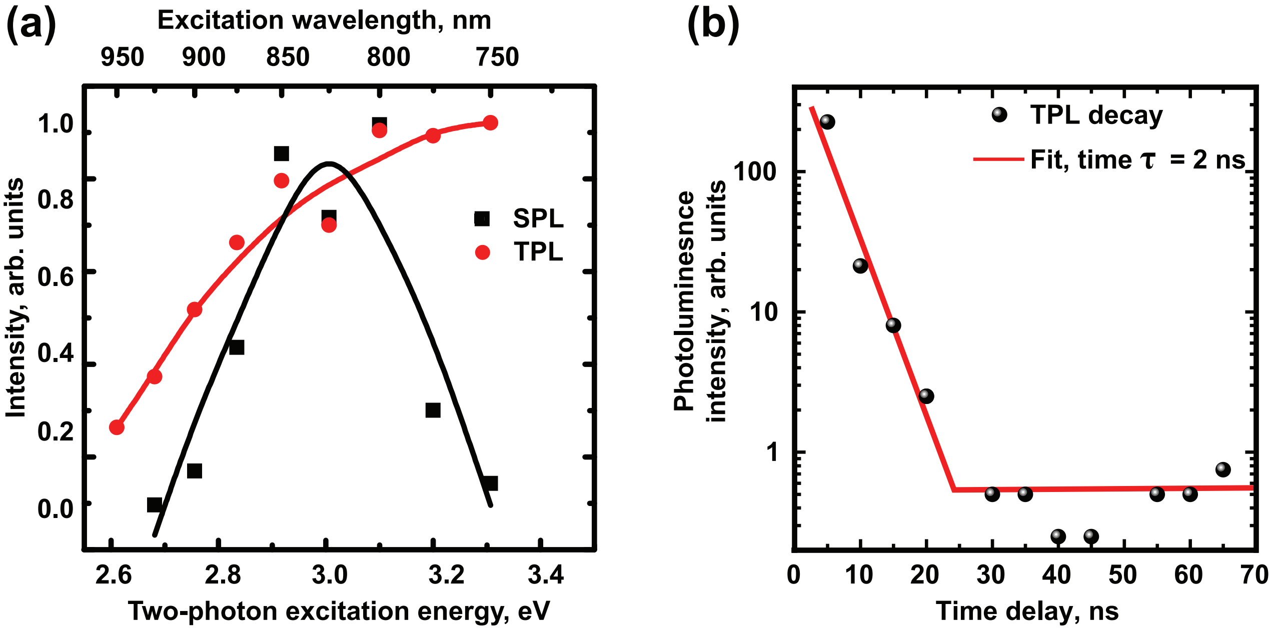

Figure 3.14: (a) Excitation spectra of SPL and TPL in the laser annealed microtubes; (b) TPL decay of laser annealed FFMT.

where Δ_1 and Δ_2 are the energy gaps between the ground state and the corresponding excited state.

Taking into account the presence of two bands in the SPL and TPL spectra, centered at $E_{SPL1} \approx E_{TPL1} \approx E_1 \approx 2.3\ eV$ and $E_{SPL2} \approx E_{TPL2} \approx E_2 \approx 2.6\ eV$, one can assume that the radiative local centers are characterized by two excited electronic states. Figure 3.15 presents a single coordinate configuration diagram with two excited states, that allows to give a qualitative explanation of the TPL and SPL. The phonon energy $\hbar\Omega = 0.124\ eV \approx$ 1003 cm^{-1} corresponds to a symmetric breathing mode of a phenyl which can be a typical energy for vibrational states in peptide tubes.

The excited state U_2 is responsible for the short wavelength component E_2 of the SPL spectrum. The location of the state U_1 is deduced from the positions of the E_{TPL1} emission spectral band with a maximum at $E_{TPL1} \approx E_{SPL1} = E_1 = 540\ nm \approx$ 2.3 eV and from the maximum of the TPL excitation spectra of about 3.3 eV (fig. 3.11). Both states U_1 and U_2 are characterized by strong electron-phonon interaction as evidenced by the width and the asymmetry of the luminescence peaks. The difference in peak intensity at E_1 and E_2 suggest that the probability of the radiative transitions from the U_1 state proportional to ${\tau_1}^{-1}$, should be higher than that from the U_2 state: ${\tau_1}^{-1} > {\tau_2}^{-1}$. At room temperature T_R, the activation barrier height δ_{12} between the minima of the U_1 and U_2 adiabatic potential surfaces satisfies the inequality $\delta_{12} > \mathrm{kT_R}$, which explains the possibility to observe both luminescence bands at low excitation intensity (single-photon excitation). In the case of TPL (high excitation level), when the local temperature of the sample is increased, the relation $\delta_{12} > \mathrm{kT_R}$ becomes invalid and the excited electrons overcome the δ_{12} barrier. This leads to a population of the U_1 adiabatic potential surface minimum and subsequently, because $\tau_1 < \tau_2$, to a vibronic radiative transition from the U_1 state. The $U_0 \rightarrow U_1$ transition results in empty

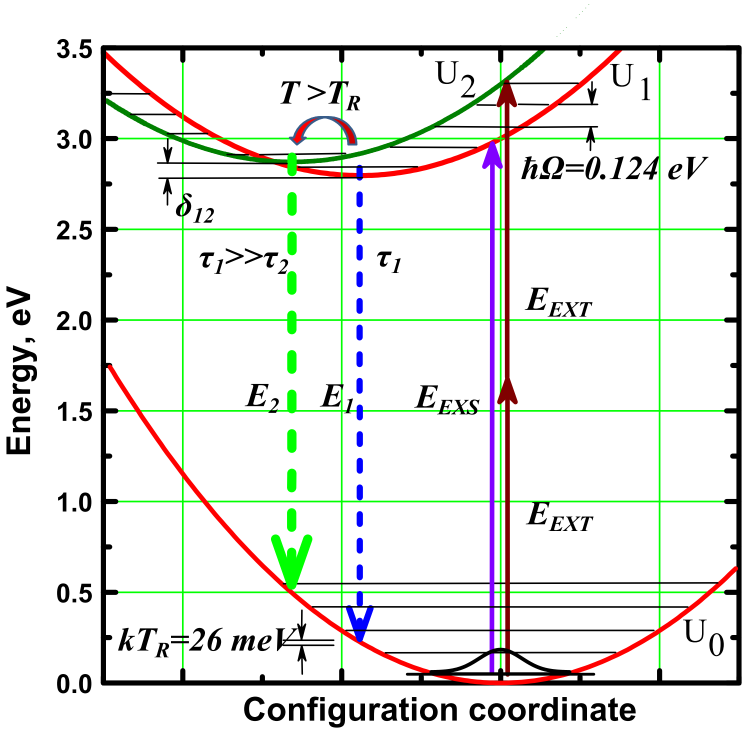

Figure 3.15: Single configuration coordinate diagram showing the arrangement of the ground state (U_0) and excited states (U_1) and (U_2) potentials, that allows to give a qualitative explanation of the SPL and TPL spectral characteristics.

vibrational levels of the ground state U_0, which, in turn, may result in the amplification of the emission if the pumping power density is high enough. This is consistent with the exponential power dependence of the TPL (see fig. 3.6). Such mechanism is responsible for lasing in vibronic lasers which realize a quasi-4-level scheme.

Photon-induced defect generation, or in other words, photon-induced doping with color centers gives a way to produce bio-compatible four-level gain laser media, which can be explored for optical frequency converters. These organic FFMTs hint at numerous additional applications in photonics (light emitting diodes and amplifiers) and even as functionalized organic near-field probes and sensors. The properties of these unique materials may allow electrode-free visible light sources compatible with physiological environments to be developed, thus promising a lot of applications in bio-photonics.

The strong and tunable single-photon and two-photon luminescence in the visible range, which appears after temperature treatment of self-organized peptide microtubes significantly extends the functionality of these bio-inspired microstructures. Analysis of the luminescence characteristics together with the annealing conditions allow us to conclude that the most probable reason for the observed effects, including the luminescence enhancement, is thermo-induced modification of the watercontaing “supercell” generating radiative centres and allowing the appearance of the light not only in the UV but also in the green range. The observed effects suggest a new approach for the creation and modification of the optical properties dipeptide microstructures.

3.8 Waveguiding properties of peptide microtubes

The fact that peptide microtubes have a uniform and well-defined crystal structure, a simple fabrication process and a small absorption in the green and red part of the visible spectrum makes them good candidates to serve as optical waveguides. We studied the waveguiding properties of the peptide tubes both for the case of fresh and laser heated peptide tubes.

3.8.1 Waveguiding in non heat-treated tubes

To study waveguiding properties of FFMTs, we have to couple light in and out of the tubes in a proper way which is not easy due to the size of the objects. This was achieved by manipulating the tubes in such a way that their ends were free from the substrate surface, whereas light was coupled in and out using tapered optical fibers mounted on precisely positioned stages(fig. 3.16(a)). An image made with an optical microscope shows a peptide microtube placed between two optical fiber tips (fig. 3.16 (b)). When the position of the optical fibers is optimized it is clearly seen that the light at the wavelength of the 800 nm propagates through the FFMT and outcouples on its end (marked with red circle on fig. 3.16 (c)).

A similar experiment was made for the case of splitting tubes having two branches (fig. 3.16 (d)). These divide the propagating light into two parts, but due to the random character of the self assembly process, it is impossible to control the sizes of the splitting tubes and, hence, the beam-splitting ratio. The measured intensity ratio was of about 1:8 for 800 nm and 1:16 for 1518 nm (fig. 3.16 (d)). The difference in ratio for two wavelengths can be caused by differences in mode distribution.

We have made an estimate of the light transmission through the FFMT in such a geometry, which is related to the efficiency of the propagation. Transmission can be calculated as $T_{FFMT} = \frac{I_{trans}}{I_{max}} * 100\%$, where I_{trans} corresponds to the signal when the tube is located between the incoupling and outoupling fibers. The value I_{max} was measured when two ends of the optical fibres were placed close to each other and optimized for a maximum transmission signal. The maximum T_{FFMT} we measured reached 65% for a tube of about 1 mm in length or, recalculated in losses, $L_1 = -3.01$ db/mm. This is about ten times better than values shown in dye incorporated peptide tube $L_2 = -31.5$ db/mm for a 225 μm length of propagation. The reason for this difference of T_{FFMT} can arise from a better geometry of light in- and outcoupling in our experiments and due to additional absorption caused by the presence of the dyes in the tubes used in the work of *Yan et al* [7].

Optical images as presented in fig. 3.16 do not give a clear understanding which part of the tube is responsible for light propagation. One can assume that two propagation behaviours are possible: light can travel (1) in the hollow part of the tube and (2) via its walls. In order to get a better understanding of the waveguiding process we have made spatial scans with the detection fiber in the plane perpendicular to the axis of the tube (in the *z*-*x* plane, see fig. 3.16(a)). The movement of the fiber in *z*-*x* plane gives spatial distribution of the outcoupled light in the far-field which is related to the

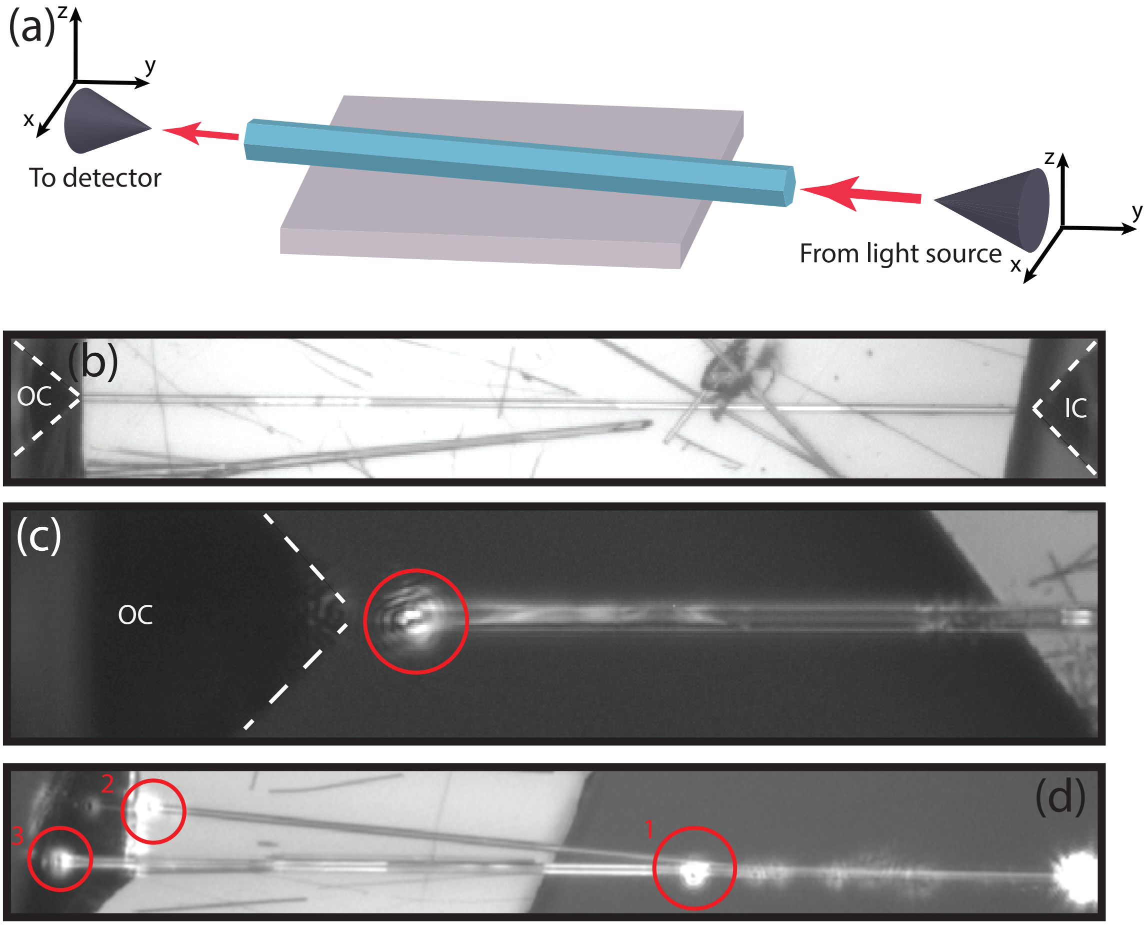

Figure 3.16: Propagation of the light through the FF-tube; (a) Sketch of the experiment and tube location. Grey cones depict parts of the optical fibers used for excitation of the object and detection of the transmitted ligth. Both of the fibers can be moved by XYZ scanning tables, for alignment. Note that light is propagating from right to left for all images in this figure. (b) Overview image of FFMT on the substrate, two dark cones marked with dashed lines correspond to the incoupling (IC) and outcoupling (OC) optical fibers ; (c) Zoomed image of outcoupling part where propagating light is clearly seen (marked with red circle). White dashed lines depict positions of the detection fiber (OC); (d) Waveguiding through the splitting tube. Red circles depicts light outcoupling in: (1) place of tube splitting; (2) side tube; (3) main tube.

mode distribution inside the peptide tube. Scans were performed for 400 nm, 800 nm and in the IR range at 1560 nm. The results clearly show the tubular character of light propagation through the walls of the tube for 400, 800 and 1560 nm (fig. 3.17). It can be also seen that light does not propagate inside the substrate. In the case of 1560 nm, the tubular structure is less pronounced, but light still propagates through the walls as the central part of the tube demonstrates minimal signal. These results were compared with calculations of light mode distribution.

Calculations of the waveguiding properties were performed with the help of Lumerical FDTD Solution software. We investigated the propagation of a monochromatic wave with gauss distribution of the intensity through the peptide tube for different wavelengths, chosen to match our experimental conditions. Thus we have light with the wavelength at 400 nm (second harmonic signal), 800 nm (fundamental) and 1560 nm. As a model structure we use a tubular structure with inner diameter 1.4 μm and outer diameter 3.2 μm with different lengths (which correspond to the real dimensions of the tubes). Analysis of the calculated data shows the possibility of the propagation of the light through the walls of the microtubes. These results are in good agreement with the experimental results which show similar behaviour. The calculations also showed localisation of the light close to the substrate, which was also observed in the experimental results (3.17).

The same experiments were done for the case of white light propagation (halogen lamp used as light source). Precise positioning of the in-coupling and out-coupling fibres allows us to perform spectral investigation of individual tube in the longitudinal direction. A circular shape is not observable anymore and less resolved compared to the case of laser excitation. A poor localisation can be caused by the very high divergence of the light source (halogen lamp) together with its low intensity compared to the laser. Typical spectra obtained for several different positions of in-coupling and out-coupling fibre demonstrate a lot of noise and low reproducibility, despite averaging between 100 measurements for each spectrum. However, these measurements demonstrate that even with such a poor (compared to laser) light source it is possible to obtain transmission of around 10-15% . It also shown that freshly made tubes do not have any well pronounced, significant and specific molecular optical response in the visible range, which is in agreement with our luminescence measurements (see previous sections of this chapter).

3.8.2 Waveguiding experiments of heated FF tubes

In order to study the role of heat induced defects we performed waveguiding experiments in another geometry. As we have shown before, heat or laser treatment allows to introduce modifications in the peptide tubes responsible for modifications of the optical properties. These modifications include the appearance of the enhanced broad luminescence peak in the range of 500 to 580 nm. Thus the optical properties of the individual FFMT are modified with a laser and introduce luminescence inside a tube. This may also induce changes of the waveguiding characteristics. For this experiment an inverted microscope set-up was used and the excitation beam was send perpendicularly to the long axis of the tube. The geometry of these experiments differs from that was used in previous section.

Optical microscopy images show tubes on the substrate which were laser treated

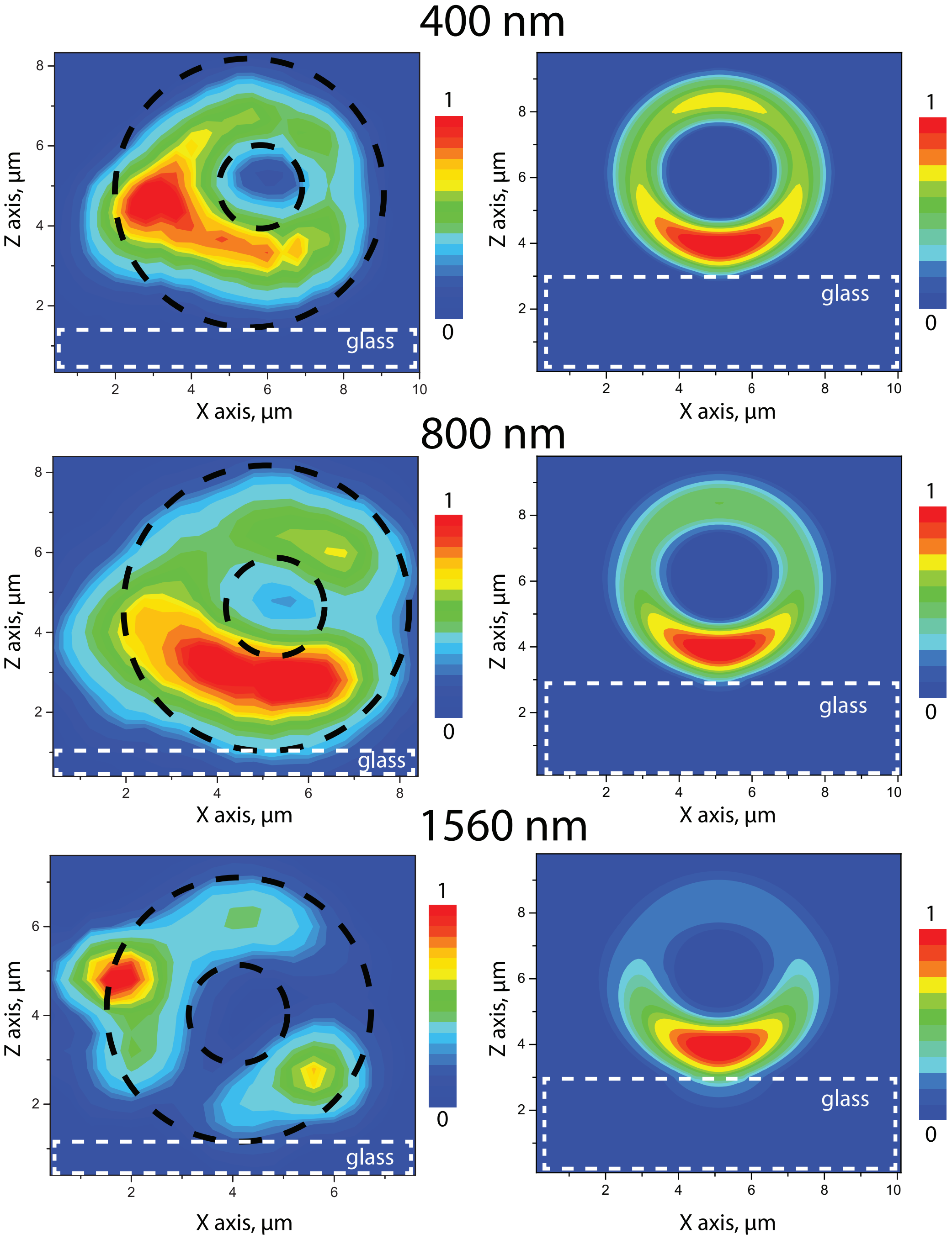

Figure 3.17: Measured field distribution (left) and corresponding calculated modes (right) in the FF peptide tube for the 400 nm, 800 nm and 1560 nm wavelengths. Experimental data clearly show circular shape of light distribution. Black dashed lines shows approximate position of the tube. White dashed lines depicts position of the glass substrate.

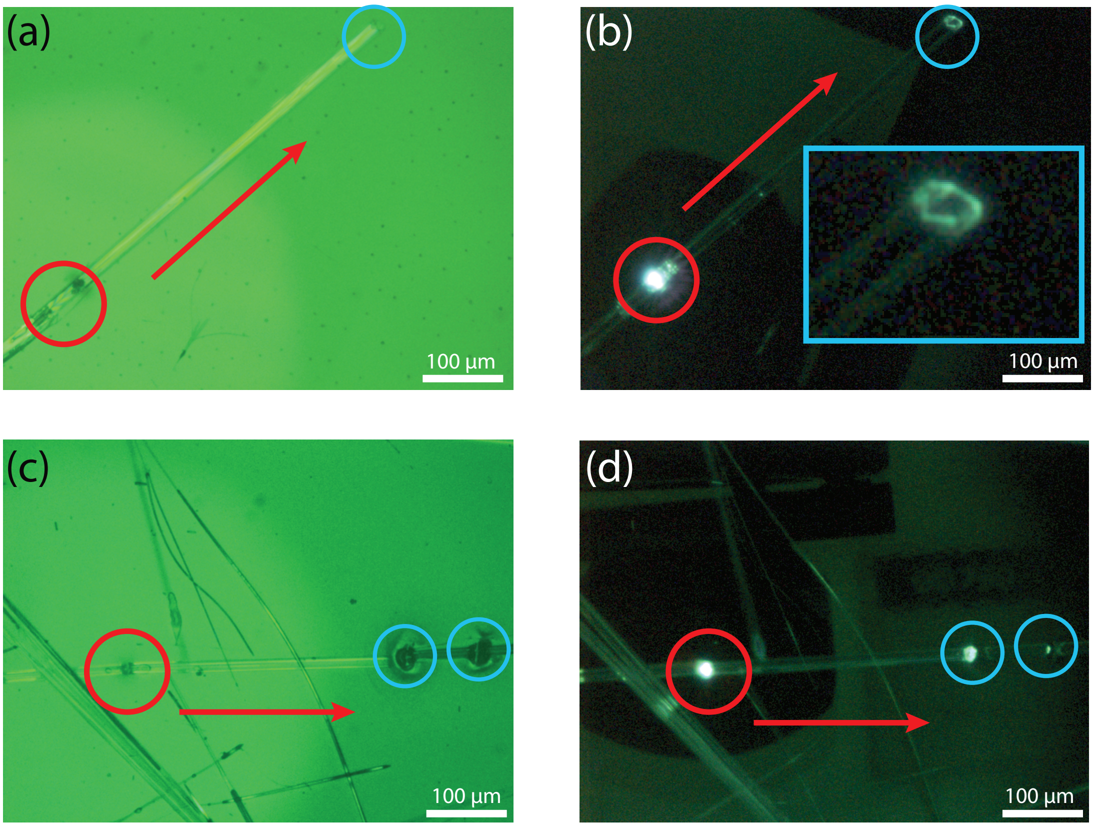

Figure 3.18: Examples of waveguiding in FF-tubes. Red circles mark the points of excitation, blue circles - points where light is outcoupled. Arrows show the direction of light propagation; (a), (b) Light outcouples from the edge of the tube. Inset in (b) shows tubular behaviour of propagation; (c), (d) Light was outcoupled via another defect (distance of propagation is about 340 μm). Note that light can be partially outcoupled from the second defect.

in order to demonstrate luminescence waveguiding of the locally induced luminescence (fig. 3.18(a)-(d)). Red circles depict the places which were processed with the laser and used as TPL sources. It is clearly seen that places where a defect was formed, have a different morphology compared to the nontreated parts (also in accordance with Section 3.6). The excited defects produce bright luminescence that partly couples into the tube and propagates there. The light can be outcoupled from another defect such as the edges of the tube (fig. 3.18(a),(b)) or via another laser induced defect. However, these sets of experiments do not allow to estimate the efficiency of the propagation, as the brightness of the output spot was dependent on the quality of the defect and the coupling efficiency. However, local defects allow us to simplify in-coupling and out-coupling of the light into the peptide tubes and combine a light source and waveguide in one “device”.

From our previous results it is known that heating in the oven leads to the appearance of the same optical response (TPL) as after laser heating (Sections 3.6 and 3.7). The optical micrograph (fig. 3.19) demonstrates luminescence from the same area of the FFMT sample after local treatment with the laser and after the sample was kept at 150 °C in an oven, which changes the structure of the whole sample. The luminescence

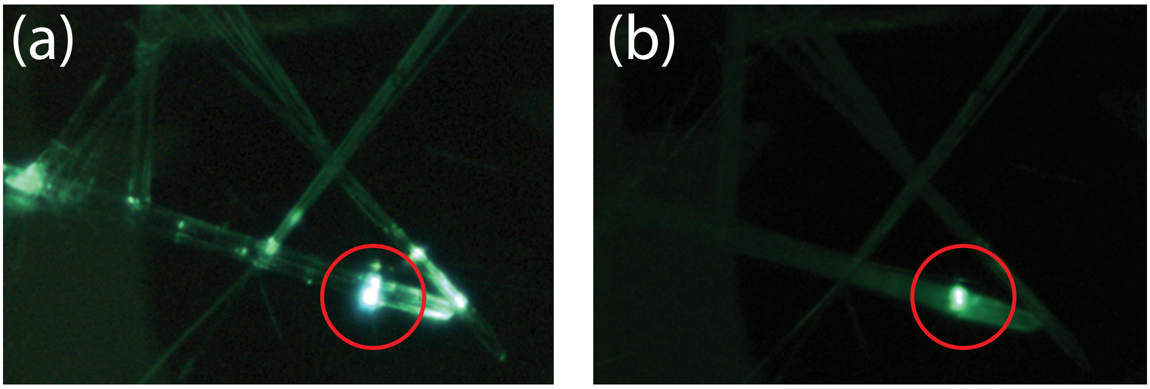

Figure 3.19: Light propagation in the tube. (a) Before sample heating. Light was coupled at the defect (marked with the red circle). Propagation and outcoupling via defects and edges can be observed; (b) Waveguiding after heating. Sample was kept at 150° degrees for an hour in oven. Luminescence can be observed in the place of excitation (marked with red circle). Waveguiding can not be observed due to the scattering and absorption of the light in the FFMT.

response is similar for both cases as expected, however, the waveguiding behaviour is not: the heating in the oven destroys the waveguiding properties . The reason for such drastic change of waveguiding can be related to the defects generated by the heating in the FFMT crystal structure (see fig. 3.10(c), (d)). These defects can cause extra scattering of the propagating light. Another reason might be the fact that such defects are optically active in the TPL spectral region, so these can absorb light. Both of these effects significantly reduce the propagation distance in oven heated FFMTs.

3.9 Conclusions

The FF-peptide molecules self-assemble into microtubes (FFMTs) in a water environment. We have demonstrated that fields of 1 T can be used for alignment of tubes while they are floating in the solvent. Water evaporation strongly disturbs alignment of dried tubes due to surface-tension forces, and even high magnetic fields (20 T) are not sufficient to produce good alignment of the FF tubes.

We have demonstrated that as-grown FFMTs have a strong SHG response due to the lack of inversion symmetry of their crystal structure. The chiral structure of the FF microtube allows to observe chiroptical effects such as a difference of the SHG efficiency for right and left-circularly polarised light. The analysis of the data allows to conclude that the SHG response includes magnetodipole and electro quadrupole contributions.

The structure and SHG response can be modified with heat treatment as well as via laser annealing, both of them induce different morphology changes but similar changes of optical signals: a decrease of SHG and the appearance of strong TPL. The reason for these signal changes is due the phase transformation, which can be divided in two subsequent steps: one corresponds to the evaporation of the water molecules from the inner structure, the second one is caused by a molecular transformation. We find step two to be related to a decrease of the SHG signal due to the modification of crystal lattice from hexagonal to orthorhombic. The first step most likely is related to the appearance of TPL in the processed microtubes, despite the fact that single FF molecules do not show any luminescence in the visible range. The appearance of TPL is likely related to the optical response of the FF "supercell".

The undisturbed crystal structure of a FF-microtube clearly demonstrates waveguiding. Waveguiding can be observed for wavelengths from the visible to near IR ranges of the spectrum. The local laser treatment of the FF-tube leads to the formation of local regions which can generate TPL and these regions then act as a light source. Thus the generated TPL can also propagate along the tube and be outcoupled from another defect or end of the tube. Both calculations and experiments demonstrate that the waveguiding occurs via the walls of the FFMT. All these observed effects make FF-microtubes structures promising candidates for photonic applications.

References

[1] N. Amdursky, P. Beker, I. Koren, B. Bank-Srour, E. Mishina, S. Semin, T. Rasing, Y. Rosenberg, Z. Barkay, E. Gazit, and G. Rosenman, "Structural transition in peptide nanotubes," *Biomacromolecules*, vol. 12, pp. 1349–54, Apr. 2011.

[2] A. Heredia, I. Bdikin, S. Kopyl, E. Mishina, S. Semin, A. Sigov, K. German, V. Bystrov, J. Gracio, and A. L. Kholkin, "Temperature-driven phase transformation in self-assembled diphenylalanine peptide nanotubes," *J. Phys. D: Appl. Phys.*, vol. 43, no. 46, 2010.

[3] N. Amdursky, M. Molotskii, E. Gazit, and G. Rosenman, "Self-assembled bioinspired quantum dots: Optical properties," *Appl. Phys. Lett.*, vol. 94, no. 26, p. 261907, 2009.

[4] X. Yan, Y. Su, J. Li, J. Früh, and H. Möhwald, "Uniaxially oriented peptide crystals for active optical waveguiding," *Angew. Chem. Int. Ed.*, vol. 50, pp. 11186–91, Nov. 2011.

[5] L. Adler-Abramovich, D. Aronov, P. Beker, M. Yevnin, S. Stempler, L. Buzhansky, G. Rosenman, and E. Gazit, "Self-assembled arrays of peptide nanotubes by vapour deposition," *Nat. Nanotechnol.*, vol. 4, pp. 849–54, Dec. 2009.

[6] C. H. Görbitz, "The structure of nanotubes formed by diphenylalanine, the core recognition motif of Alzheimer's beta-amyloid polypeptide," *Chem. Comm.*, pp. 2332–4, June 2006.

[7] X. Yan, J. Li, and H. Möhwald, "Self-assembly of hexagonal peptide microtubes and their optical waveguiding," *Adv. Mat.*, vol. 23, pp. 2796–801, July 2011.

[8] J. Ryu, S. Y. Lim, and C. B. Park, "Photoluminescent peptide nanotubes," *Adv. Mat.*, vol. 21, pp. 1577–1581, Apr. 2009.

[9] N. Na, X. Mu, Q. Liu, J. Wen, F. Wang, and J. Ouyang, "Self-assembly of diphenylalanine peptides into microtubes with "turn on" fluorescence using an aggregation-induced emission molecule.," *Chem. Comm.*, vol. 49, pp. 10076–8, Oct. 2013.

[10] R. A.Hill, V. Sedman, S. Allen, P. Williams, M. Paoli, L. Adler-Abramovich, E. Gazit, L. Eaves, and S. Tendler, “Alignment of aromatic peptide tubes in strong magnetic fields,” *Adv. Mat.*, vol. 19, pp. 4474–4479, Dec. 2007.

[11] N. Kol, L. Adler-Abramovich, D. Barlam, R. Z. Shneck, E. Gazit, and I. Rousso, “Self-Assembled Peptide Nanotubes Are Uniquely Rigid Bioinspired Supramolecular Structures,” *Nano Lett.*, vol. 5, pp. 1343–1346, July 2005.

[12] Y. Shen, *The principles of nonlinear optics.* Wiley Series in Pure and Applied Optics, J. Wiley, 1984.

[13] S. Sioncke, T. Verbiest, and A. Persoons, “Second-order nonlinear optical properties of chiral materials,” *Mat. Sci. Eng.: R*, vol. 42, pp. 115–155, Nov. 2003.

[14] M. J. Nystrom, B. W. Wessels, W. P. Lin, G. K. Wong, D. a. Neumayer, and T. J. Marks, “Nonlinear optical properties of textured strontium barium niobate thin films prepared by metalorganic chemical vapor deposition,” *Appl. Phys. Lett.*, vol. 66, no. 14, p. 1726, 1995.

[15] J. Li, C.-H. Wen, S. Gauza, R. Lu, and S.-T. Wu, “Refractive Indices of Liquid Crystals for Display Applications,” *J. Displ. Tech.*, vol. 1, pp. 51–61, Sept. 2005.

[16] E. P. Kaiser and W. Parrish, “Preparation of immersion liquids,” *Ind. Eng. Chem. Res.*, vol. 11, pp. 560–562, Oct. 1939.

[17] C. H. Gorbitz, “Nanotube formation by hydrophobic dipeptides,” *Chem. Eur. J.*, vol. 7, no. 23, pp. 5153–5159, 2001.

[18] M. Jaworska, A. Jeziorna, E. Drabik, and M. J. Potrzebowski, “Solid state nmr study of thermal processes in nanoassemblies formed by dipeptides,” *J. Phys. Chem. C*, vol. 116, no. 22, pp. 12330–12338, 2012.

[19] P. Gill, T. T. Moghadam, and B. Ranjbar, “Differential scanning calorimetry techniques: applications in biology and nanoscience,” *J. Biomol. Tech.*, vol. 21, pp. 167–93, Dec. 2010.

[20] M. J. Wang, S. J. Xiong, X. L. Wu, and P. K. Chu, “Effects of water molecules on photoluminescence from hierarchical peptide nanotubes and water probing capability,” *Small*, vol. 7, no. 19, pp. 2801–2807, 2011.

[21] N. Amdursky, M. Molotskii, D. Aronov, L. Adler-Abramovich, E. Gazit, and G. Rosenman, “Blue luminescence based on quantum confinement at peptide nanotubes,” *Nano Lett.*, vol. 9, pp. 3111–5, Sept. 2009.

[22] K. Cho and Y. Toyozawa, “Exciton-phonon interaction and optical spectra self-trapping, zero-phonon line and phonon sidebands,” *J. Phys. Soc. Jpn.*, vol. 30, no. 6, pp. 1555–1574, 1971.

[23] S. Anghel, G. Boulon, A. Brenier, E. Fortin, S. Klokishner, D. Koshchug, L. Kulyuk, and K. Sushkevich, “Spectroscopic characterization of Ti-doped $\alpha - \mathrm{ZnAl_2S_4}$ spinel-type single crystals,” *J. Phys.: Condens. Matter*, vol. 22, p. 055903, Feb. 2010.

Chapter 4

Optical properties of self-assembled DPFO microstructures [1]

The aim of this chapter is to study the variety of optical effects occurring in molecular crystals fabricated from 2,7-diphenyl-9H-fluoren-9-one (DPFO) molecules by self-organisation from solution in heptane. The molecular structure of DPFO gives rise to the presence of a linear optical response in the visible spectral range. We have observed the appearance of two photon luminescence (TPL) in the same spectral range. DPFO microfibres demonstrate strong second harmonic generation (SHG) which can occur due to the non-centrosymmetric molecular packing inside the structure. We demonstrate that the DPFO microfibres can be used as waveguides for the visible spectral range.

4.1 Introduction

For the next generation of integrated optical circuits, one-dimensional (1D) multi-responsive materials with tunable nonlinear optical (NLO) properties are highly desired for optics and optoelectronics [1; 2]. While inorganic NLO active micro-/nano- fibers have been developed as photonic components [3] there are few examples of organic 1-D assemblies with strong NLO properties [4], despite their intrinsic advantages of ease of assembly and clear structure-property correlations. One of the most commonly applied NLO effects is second harmonic generation (SHG), in which two incident photons combine to generate a photon with doubled frequency and thus doubled energy (described in details in chapter 5). This SHG occurs when an intense laser beam interacts with a medium with a high second-order susceptibility [5]. For organic materials this is achieved by a high molecular hyperpolarizability (strongly dipolar conjugated donor(D)-acceptor (A)), combined with a non-centrosymmetric crystallographic structure of molecules [6]. A further NLO process is two-photon excitation luminescence

---

[1] This chapter is based on J. Xu, S. Semin et al., Adv. Mat.,2013

(TPL). It is related to the energy levels of a molecule and, hence, can occur independently from the presence of the SHG. It is a third- order NLO process, in which two photons are absorbed simultaneously to reach an excited state followed by radiative relaxation processes (details of two-photon process are described in Chapter 2)[7; 8]. Typical molecules that display a high two-photon absorption cross-section have strong quadrupoles or octupoles (D-A-D, A-D-A, or more complex D-A-substituted molecular systems) [9].

Organic Intramolecular Charge Transfer (ICT) compounds are examples of molecules with strongly conjugated D and A parts [10], which results in intrinsically high hyperpolarizabilities that are widely employed as second- and/or third- order NLO chromophores [11]. The main impediment for the development of large libraries of materials for SHG from these ICT compounds is the requirement of the NLO chromophores to be arranged noncentrosymmetrically [12]. Approaches such as macromolecular scaffolding [12], field-assisted poled-polymer alignment [13], controlled Langmuir-Blodgett techniques [14], and utilisation of the intermolecular interaction for design of molecular crystals [15] have all been developed to induce macroscopic non-centrosymmetry. Some of these strategies, however, generate materials that show poor light propagation due to losses or poor coupling to integrated optical circuits, for which 1D crystalline architectures are more suitable [16].

Rubahn et al. have successfully demonstrated organic nanofibre frequency doublers from *p*-hexaphenylene (*p*6P) and other functionalized oligo-*p*-phenylenes [4]. These nanofibers were produced in a sophisticated high-vacuum growth procedure on a muscovite mica substrate and the nanofibers were required to be carefully transferred for optical examinations. Much simpler solution-based processing techniques would be strongly favoured, but unfortunately such examples are rare.

It was previously reported that fluorene bridged ICT compounds are able to self-assemble via simple solution processing steps into 1-D microfibers with interesting linear optical properties [17]. In this chapter, the self-assembly of a new V-shaped fluorenone based ICT compound 2,7-diphenyl-9H-fluoren-9-one (DPFO) (fig. 4.1a) into a unique non-centrosymmetric microfibre structure is reported [18]. The arrangement of the molecules inside the structure results in a permanent dipole along the fibre's long axis and a transition dipole perpendicular to it. The microfibres display both a SHG and TPL response and the behaviour of the signals makes it possible to spectrally and spatially separate both NLO effects. The spatial separation is possible due to the highly localised and directional waveguiding properties of TPL. The easy processability, perfect crystalline microfire structure, and intrinsic highly efficient NLO effects of the DPFO microfibres offer great opportunities for applications in photonic devices.

4.2 Linear optical properties of DPFO

DPFO belongs to the class of intramolecular charge transfer (ICT) molecules, where one part of the molecule works as an electron donor (D) and the other one as an acceptor (A). These parts are connected to each other with a relatively long conjugation acting as a bridge. Such molecular structure leads to the delocalisation of the π-electrons and predicts the appearance of luminescence in the visible region (fig. 4.1(d)).

The self-assembly process organises them in well-defined molecular microcrystals in a heptane environment (fig. 4.1b). In order to study the linear optical properties in both solution and aggregated state, UV-visible absorption and photoluminescence (PL) measurements of DPFO molecules were performed. Self-assembly of the molecules in aggregated and elongated structures does not lead to dramatic changes in the absorption and PL spectra compared to molecules in solvent (fig. 4.1(c) and (d)). The DPFO molecules dissolved in tetrahydrofuran (THF) have a broad absorption peak centred at 433 nm, whereas microfibres suspended in heptane have a maximum absorption at 425 nm. The shape of both absorption peaks is similar for separate molecules and microfibres. When both samples were excited at 430 nm, the DPFO molecules demonstrated a PL maximum at 537 nm, while the microfibres emitted at 541 nm. This close position of absorption/emission peaks for individual molecules and fibres can be an indication that the $\pi - \pi$ stacking of DPFO molecules is not very strong and does not influence the optical properties of the material in the aggregated state. The quantum yield of separate DPFO molecules increased from 21% in solution (THF) to 28% for powders of DPFO microstrucutres.

4.3 Nonlinear optical properties of DPFO

The noncentrosymmetric crystal structure (Cmc2_1 space group), high polarity of the molecule, and the 1-D fiber-like morphology make DPFO single crystalline supramolecular architectures a candidate for the observation of the nonlinear optical (NLO) effects.

The NLO response of the DPFO microfibers has been examined by a scanning SHG set-up described in Chapter 3. Samples were excited with a femtosecond laser and the polarisation of the incident beam was linear which was modified with a half-wave plate, while all the polarisation components were detected. The two-photon excited optical spectra of the DPFO crystal collected by a charge-coupled device detector (CCD) show the presence of both SHG and TPL responses (see fig.4.2 (a)). The group of narrower peaks in the left part of the figure corresponds to the SHG signal generated in the DPFO microstrucuture. Locations of the peaks correspond to the half of the wavelength of the excitation laser $\lambda_{SHG} = \frac{\lambda_{exc}}{2}$. The broad peak with the maximum at $\lambda_{TPL} = 530$ nm can be identified as the TPL signal and did not change position as the excitation wavelength was changed. TPL is a resonant process, it means there is a real optical transition which can be excited if the the energy of the photons is sufficient to overcome the barrier between ground and excited state. The position of the center of this broad peak corresponds to the position of the luminescence obtained by single-photon excitation.

The power dependence of the two signals confirms their nonlinear optical nature. As shown in fig.4.2(b), the intensity for both SHG and TPL increases quadratically with the power of the input laser, with slopes of about 2 (1.94 for SHG and 1.99 for TPL respectively) confirming the two-photon nature for both of them [19].

The NLO processes in the fiber-shaped single crystals are expected to be strongly polarization-dependent due to their well-oriented dipole moments [20]. The SHG is

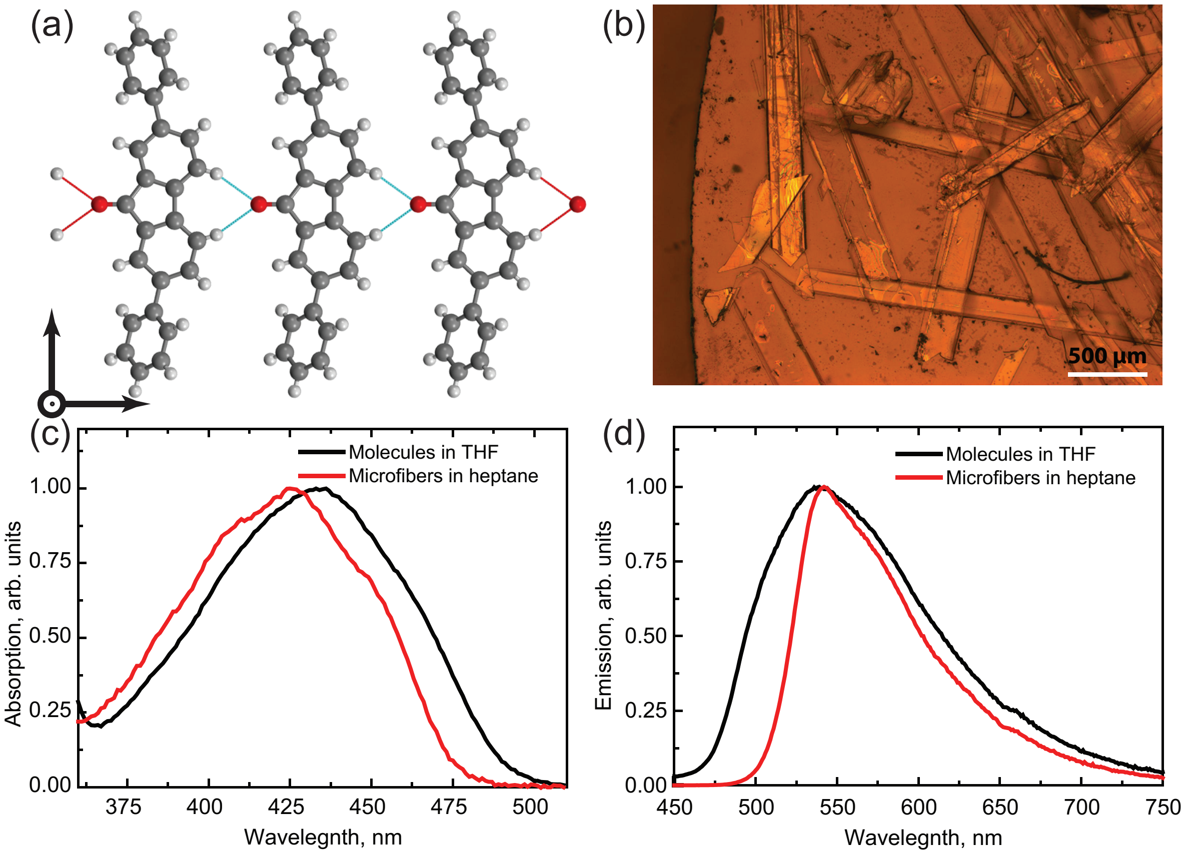

Figure 4.1: (a) Molecular packing of the DPFO into the crystal structure. Gray spheres represent carbon atoms, red ones - oxygen, white- hydrogen dipole moment is aligned along c axis of the crystal; (b) Optical image of DPFO microfibers from heptane on the glass substrate; (c) Absorption and (d) emission spectra of DPFO molecules/microfibres. Black curves on both plots ((c) and (d)) correspond to the spectra from separate molecules dissolved in THF solvent, red curves correspond to the assembled structures (microfibres) in the heptane environment.

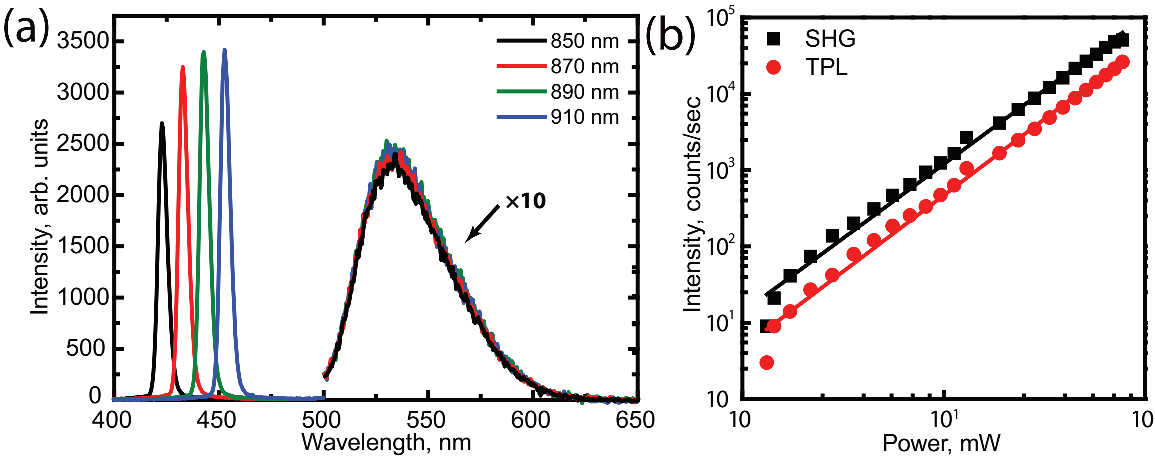

Figure 4.2: Nonlinear optical properties of DPFO microfibers. While the excitation was performed in the whole range of the Ti:sap laser, only selected spectra are plotted. (a) Optical spectrum for DPFO microfibers for different excitation wavelengths. Narrow peaks correspond to the SHG signal and shift as function of the excitation wavelength. Broad peak corresponds to the TPL signal; (b) Intensity of SHG and TPL signal as function of incident laser power. Both signals demonstrate quadratic behaviour, confirming the two-photon nature of SHG and TPL.

related to the permanent dipole moment difference between the ground and excited states $\Delta\mu = \mu_e - \mu_g$ and the transition dipole (μ_{ge}). Excited-state calculations indicate that the lowest optically allowed excitation involves mainly (89%) the electronic transition from HOMO to LUMO (fig. 4.3(a)) and is calculated at about 3.4 eV (368 nm) with the transition dipole (μ_{ge}) oriented along the molecule (the crystallographic *b*-axis; fig. 4.3 (a)), and the change of the permanent dipole ($\Delta\mu$) along the long fiber axis (the c-axis, fig. 4.3 (c)) [21]. HOMO/LUMO levels for the DPFO molecules were obtained by INDO/SCI excited-state calculations in the Materials Studio Package.

Both the second-order SHG and the third-order TPL from two crossing microfibres were studied by confocal laser scanning microscopy (CLSM)(fig.4.4(a)) in transmission geometry,. When detecting only the SHG, the fibres yielded much more signal when the polarisation of the excitation was along the fibre (fig. 4.4 (b), (c)). When detecting both SHG and TPL, the difference of the signal intensity from the two fibres, by rotating the excitation polariser from vertical to horizontal, was not so pronounced (fig. 4.4 (d), (e)). From this data we can conclude that TPL gives a higher contribution to the detected signal than SHG and has less dependence on the polarisation state of excitation light.

Polarisation dependence of the NLO responses an be related to the dipole moments of the molecule. To determine the effects of the transition dipole moment (μ_{qe}) and the difference of the permanent dipole moment between the ground and the excited states ($\Delta\mu$) on the two NLO processes, the polarization dependence of both SHG and TPL has been measured at 400 and 530 nm, respectively, as a function of the polarisation angle of the incident beam. The NLO signals were recorded on a single microfibre along all three crystallographic axes in reflection (along the *b*-axis) or transmission (along the *a*-

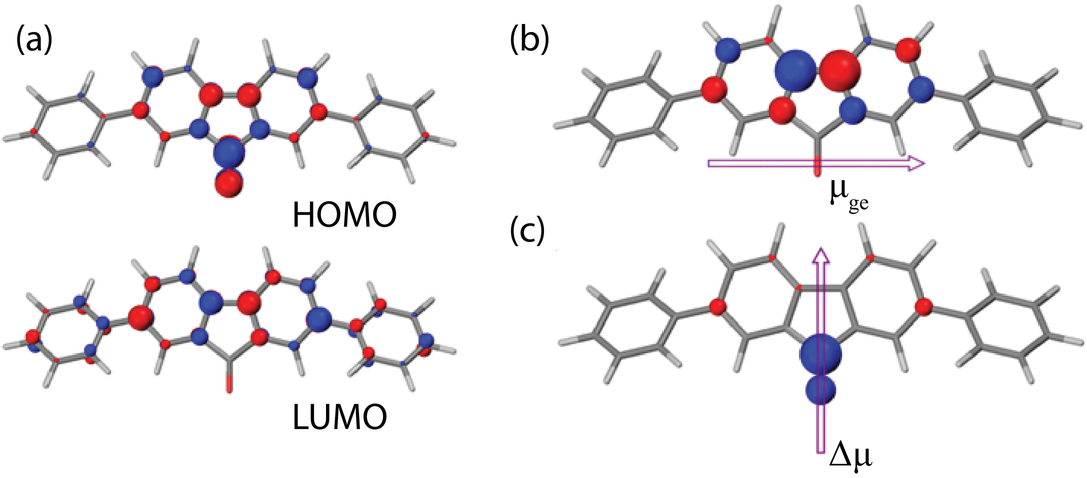

Figure 4.3: The structure of the lowest optically allowed transition in a single DPFO molecule. (a) Shape of the HOMO and LUMO wavefunctions. The size and colour of the spheres represent the amplitude and sign of LCAO (Linear Combination of Atomic Orbital) coefficient, respectively. (b) Transition density (blue and red spheres) and the transition dipole (the arrow μ_{ge}). (c) Excited-state minus ground-state charge distribution (blue and red spheres) and the state dipole difference (the arrow $\Delta\mu$) for a single DPFO molecule. The size and color of the spheres represent the amplitude and sign (blue is negative and red positive) of the charge, respectively. The geometry of a single DPFO molecule has been extracted from the X-ray resolved structure and used as input for excited-state calculations (using an active space of 20 occupied and 20 unoccupied molecular orbitals).

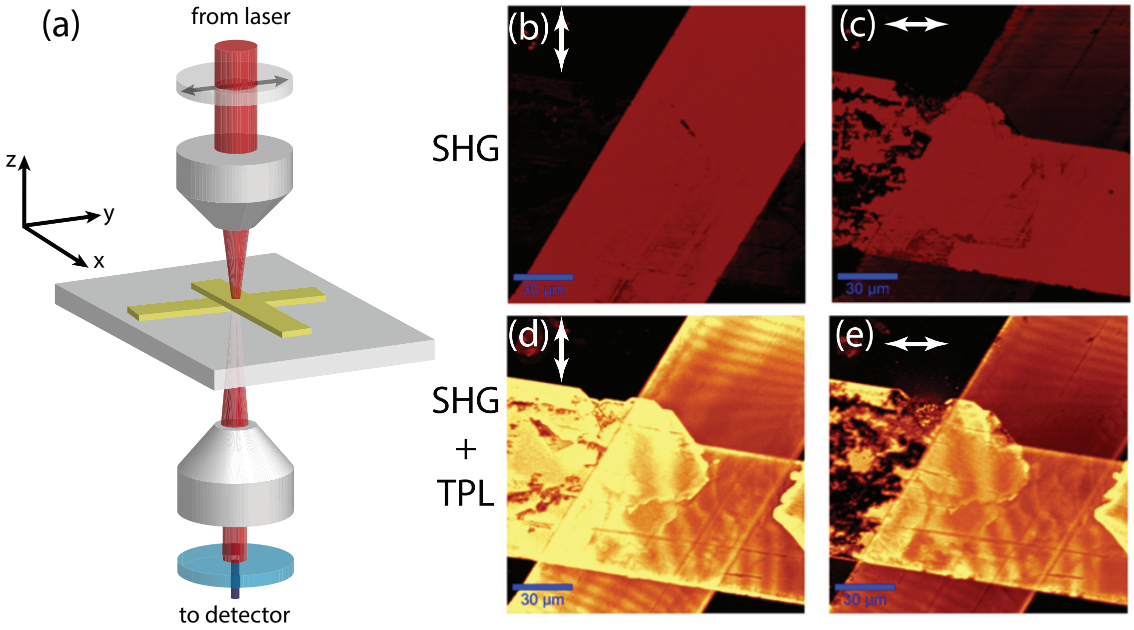

Figure 4.4: Polarisation dependence examined by confocal laser scanning microscopy (CLSM). (a) Schematic representation of the set-up. Transmitted light is sent to the detector; (b),(c) CLSM images of two crossing fibres taken by detecting SHG only with vertical polarisation (left) and horizontal polarisation (right). (d),(e) CLSM images of two crossing fibres taken by detecting both SHG and TPF signals with vertical polarisation (left) and horizontal polarisation (right). The arrows represent the orientation of the excitation polarisation. The excitation wavelength $\lambda_{ex} = 800$ nm.

and c-axes) geometry. The geometry of the experiments and the results are summarised in fig. 4.5. For the case of excitation perpendicular to the substrate and along the b-axis (fig. 4.5 (a)) the SHG signal shows a two-fold anisotropic behaviour. A reflection geometry was used as the substrate and the sample holder are not transparent for a transmission detecting geometry along the b-axis. In this geometry, the p-polarisation is parallel to $\Delta\mu$, and μ_{ge} is not affected by the polarisation. The excitation beam is perpendicular to the permanent dipole, which is expected to maximize the polarisation ratio $\rho = \dfrac{I_{max} - I_{min}}{I_{max} + I_{min}}$. Calculation of ρ, in fact, gives a value of virtually unity, which is higher than for any reported organic crystal and even higher than for inorganic nanowires [22], demonstrating a high order of alignment of the DPFO molecules inside the structure. Excitation along the b-axis, which is parallel to μ_{ge} of the molecules in the microfibre, results in an isotropic behaviour of the TPL response . The microfibre was also excited parallel to the substrate, detected in transmission mode. SHG after excitation along the c-axis (fig. 4.5 (b)) was measured and was found to give a high polarization ratio of $\rho = 1.00 \pm 0.02$. With the excitation parallel to $\Delta\mu$ of the molecules in this geometry, the polarisation dependence originates solely from the μ_{ge} in the molecules [23]. TPL also shows a clear excitation polarisation dependence with a maximum in the emission when the polarisation direction is parallel to μ_{ge} and a $\rho = 0.67 \pm 0.04$. A polarisation ratio, $\rho = 0.34 \pm 0.04$ was observed for TPL when the pump beam was parallel to the a-axis (fig. 4.5 (c)). The beam in this case was perpendicular to both $\Delta\mu$ and μ_{ge}, and the SHG signal shows a fourfold pattern with maxima in the directions of both dipoles.

4.4 Light propagation in DPFO microfibers

Both the crystalline structure and the promising optical properties of DPFO microfibres allow to propose this material as a candidate for organic waveguides. Our studies were conducted in the geometry of the experiment when the k-vector of the excitation beam was perpendicular to the long axis of the structure and all the images were recorded in transmission geometry from the back side, i.e. from the substrates side (geometry of experiment can be found on fig. 4.4).

When pumped at 800 nm, a bright bluish spot (can be attributed to $\lambda_{SHG} = 400$ nm) appeared at the position of excitation of the fibre, while green light ($\lambda_{TPL} = 540$ nm) propagated to the edges of the microfibre (fig. 4.6 (a)-(c)). The different intensity of the central spot occurs due to the high sensitivity of the nonlinear response to the incident polarisation as shown in the previous section. When the polarisation was perpendicular to the long axis of the fibre this results in almost no observable SHG while the TPL component is clearly seen in the excitation spot (fig. 4.6 (a)). When the polarisation was rotated 90°, the bright SHG overpowers the TPL (fig. 4.6 (c)). However the orientation of the polariser hardly affected the intensities of the side spots (marked with green circles in fig. 4.6).

In order to prove that the observed light spots correspond to SHG and TPL, respectively, local spectral measurements were performed (by confocal scanning laser

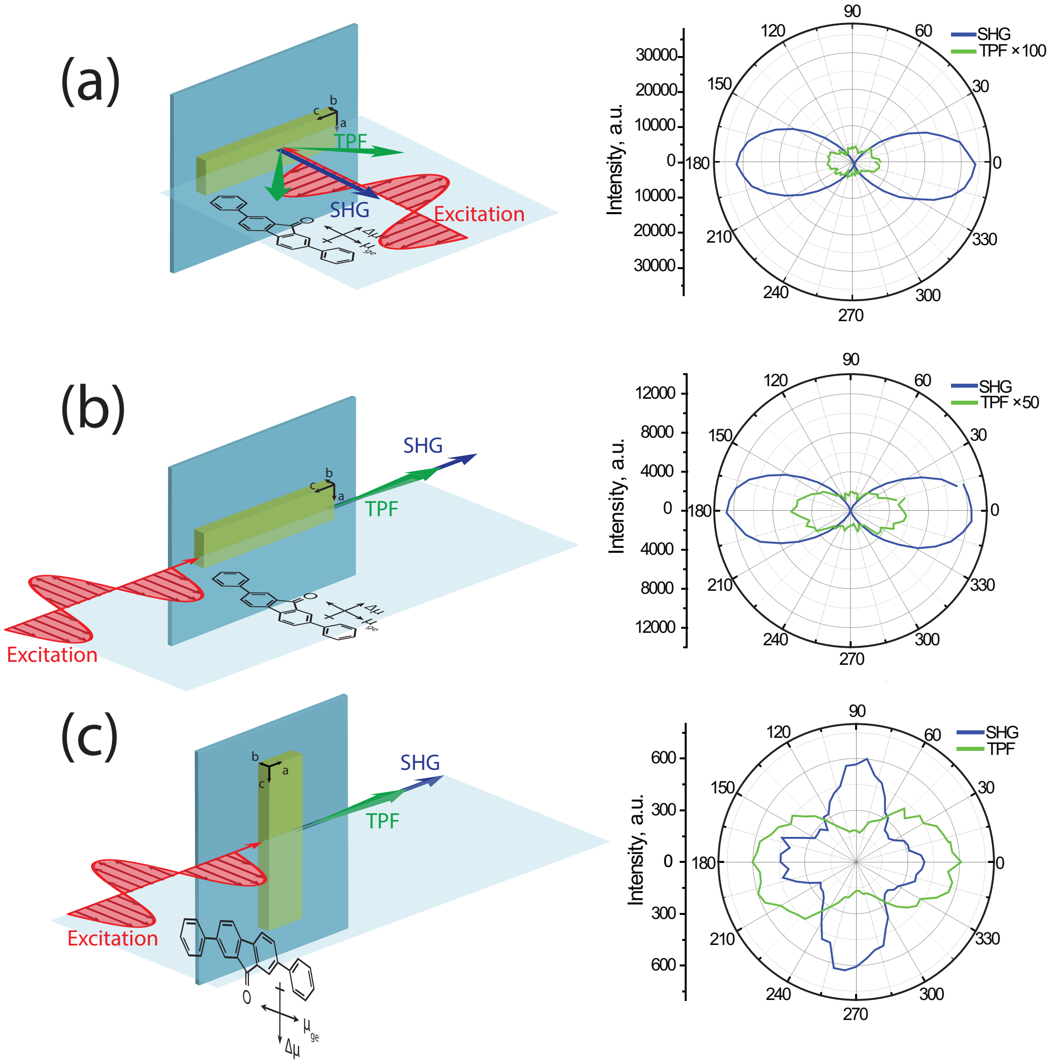

Figure 4.5: Schematic representation of the reflection or transmission geometries (left), and their corresponding angular dependence of SHG and TPL intensity on the excitation polarisation examined along the crystallographic axes (right). Width of the structure is about 100 μm, thickness about 1 μm. The insets represent the orientation of the DPFO molecules, and its corresponding transition dipole (μ_{ge}, double-headed arrows) and state dipole change ($\Delta\mu$, single-headed arrows). Laser pump: 800 nm, 16 mW. (a) Reflection geometry along the b-axis. (b) Transmission geometry along the c-axis. The p-polarisation is parallel to μ_{ge}, and $\Delta\mu$ is not involved. (c) Transmission geometry along the a-axis. The polarization rotates from p-polarization (parallel to μ_{ge}) to s-polarization (parallel to $\Delta\mu$). The reflection geometry along the b-axis was set by adjusting both incidence and detection angles as 0° from the surface normal, while the transmission geometries along a- or c- axis have both angles of 90°.

microscope). Spectra taken from the excitation spot of the microfibre showed exclusively SHG; in contrast, the spectra taken from the areas at the edge of the microfibre gave mostly TPL signal (fig. 4.6 (d)). As such, we may conclude that TPL is the light which propagates in the observed direction inside a DPFO microfibre. The non-propagation of the SHG is a direct consequence of its high directionality (conservation of the wave vector $\vec{k}$). The TPL signal, however, propagates to the edges of the microfibre, clearly demonstrating that the microfibre acts as a waveguide for TPL. Thus the waveguiding of TPL in the DPFO microfibres allow spatial separation of the nonlinear optical signals generated in the structure. As it can be seen from these data TPL propagation is highly anisotropic and directional.

To check this anisotropic behaviour of the TPL propagation inside the DFPO microfibre and to get better understanding of the observed effect we have studied the waveguiding properties whilst the sample was excited at different areas.

Figure 4.7 shows a close up micrograph of an DPFO microfibre lying on the glass substrate and locally excited with the 800 nm femtosecond laser at different places. The end part of the fibre has a triangular shape. The bright green spot in the middle part of the sample is the location of excitation. For better observation of the TPL signal the intensity of the SHG signal was reduced to minimum as the polarization of the excitation light was aligned perpendicularly to the long axis of the microfibre (like shown on fig. 4.6 (a)).

The TPL signal from the excitation spot propagated to the sides of the microfibre, resulting in the appearance of two additional bright spots at the edges of the structure(fig. 4.7(a)). These light spots were strongly directional and propagation was along the short axis of the fibre. It can be observed that some weak and divergent luminescent propagates along the microfibre and comes out through the end of the microfibre (right side if panels in fig. 4.7(a),(b)). When the excitation spot was moved closer to the triangular end of the fibre, two additional spots were observed (fig. 4.7 (c),(d)). Their positions are indicated by the perpendicular line from the excitation spot to the edge of the microfibre. Propagation is visible only along these directions towards the edge (marked with black arrows), while no light was propagating in opposite direction (marked with red arrows). The further shift of excitation closer to the end of the structure shows only two spots, as the propagation conditions were fulfilled only for the two edges at the end of the fibre (fig. 4.7(e)), and again with no propagation in opposite direction.

All these observation clearly demonstrate that propagation of the TPL light occurs along directions normal to the edges of the DPFO microfibre. Such directionality and localization of the observed TPL is surprising, as usually TPL has a more isotropic behaviour.

Two possibilities can be proposed for the explanation of this peculiar behaviour of the waveguiding of the TPL light inside the DPFO microfibre. The first option involves the anisotropy of the crystal structure. The DPFO microfibre has an orthorhombic crystal lattice, thus fourfold symmetry of propagation is expected. The excited light, in this case, can have a higher propagation efficiency along certain directions (e.g. crystallographic axes), which are separated by 90°. As a confirmation of these considerations, we observe waveguiding along shorter directions or perpendicular to the edges of the DPFO microfibre. Propagation along the long axis can not be seen because of the

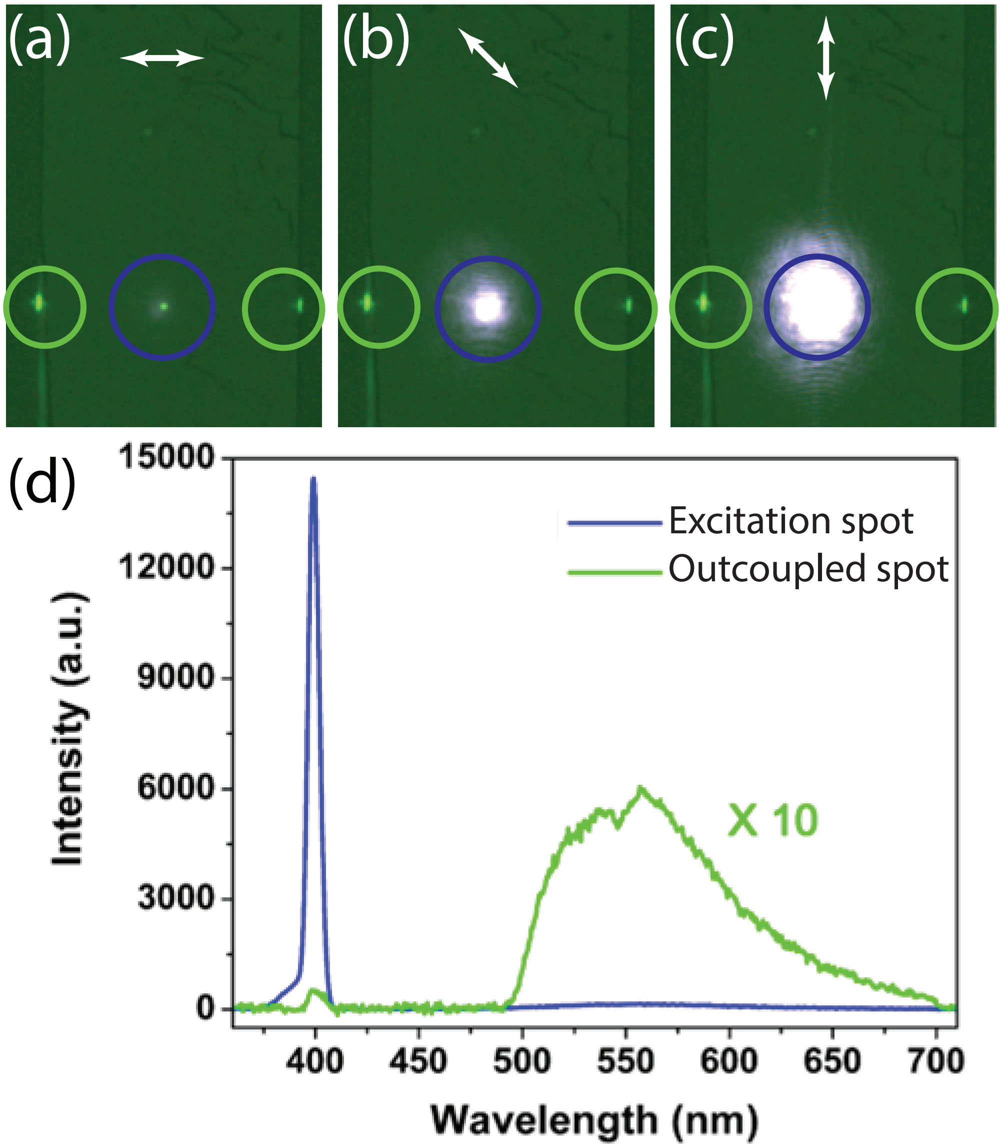

Figure 4.6: Propagation properties of the SHG and TPL, as well as demonstration of the polarisation control over SHG intensity. (a)-(c) Optical microscopy images of a DPFO microfibre excited with the femtosecond laser at 800 nm. Blue circles depict excitation spots and green circles represent exit spots. The polarisation of the incident beam was aligned perpendicularly in (a), 45° in (b) and parallel in (c) to the long axis of the microfibre; (d) Spectra obtained from excitation (blue line, collected from the region marked blue circle on panel (b)) and waveguided spot (green line, collected from the region marked green circle on panel (b)).

large size of the structure and it is simply out of the field of view of the objective. However, this assumption has some drawbacks. First, it does not explain the propagation behaviour in the end part of the fibre which has a triangular shape, where the direction of the propagation is changed (fig. 4.7 (c), (d)). The second drawback is that the anisotropy approach can not explain the absence of propagation in the backward direction (marked with red arrows), while the fourfold symmetry of the crystal lattice should lead to propagation in four directions.

The second possible explanation of observed TPL propagation assumes that anisotropy of the crystal does not play a role and propagation is fully isotropic as the luminescent process is supposed to be. To explain the observed behaviour of the light it is suggested that the light outcoupling is impeded for certain situations which we observe as directional propagation of the light. The total internal reflection (TIR) effect can be such a reason. TIR occurs when light is travelling from a medium with higher refractive index n_1 to one with lower one n_2(fig. 4.8 (a)). If the beam's angle of incidence at the interface is larger than some critical angle $\theta_{crit} = \arcsin(\frac{\mathrm{n}_2}{\mathrm{n}_1})$ it can not leave the medium and will be reflected back into the structure. Only fraction of the light (within ϕ angle) can be outcoupled from the structure. The higher the difference of refractive indices $\Delta\mathrm{n} = \mathrm{n}_1 - \mathrm{n}_2$ the more localised the outcoupled light would be. This assumption explains directionality and special conditions of observed light outcoupling, however, it also has some weak points. We estimate the DPFO refractive index to be equal $n_{DPFO} \approx 1.45$ which gives a critical angle of $\theta_{crit} \approx 43^\circ$ for the DPFO/air interface. Obviously, the observed divergence angle is much smaller than the value of the total internal reflection critical angle (fig.4.8 (b)). By changing of the position of the excitation spot from the edge of the structure we see that the divergence angle is always constant, and its value is about $\theta = (7 \pm 1)^\circ$. To fulfil the TIR conditions for such critical angle the refractive index of the DPFO should be equal to $\mathrm{n}_1 \approx 8.3$ which is too high and has no physical meaning.

We have designed and performed two experiments which could clarify the nature of the observed effect: (1) propagation of the TPL is induced by crystal anisotropy or (2) waveguiding is isotropic and TIR limits the amount of outcoupled light.

To study the influence of propagation anisotropy, the following experiment was done. Outcoupling of the light in the fibre can also be observed via defects. Hence defects are induced by a gradual increase of the laser intensity which resulted in the local burning of the microfiber. Such treatment resulted in a circular shape defect, the edges of which demonstrated the same outcoupling of the light as can be observed on the edges of microfibre (fig. 4.9(a)-(f)). The sample was excited by a laser at lower power near the defect in such a way that TPL should propagate in the DPFO microfibre along directions different from crystallographic axes. Images made with an optical microscope show that changes in position of the excitation spot change the intensity of the outcoupled light, however outcoupling was always observed (fig. 4.9(a)-(e)). Another experiment involved creation of a set of defects around the excitation spot which also does not show any preferable tendency of TPL propagation (fig. 4.9(f)). Both of these experiments demonstrate that the crystal anisotropy can not explain the directionality of propagation and outcoupling of the TPL.

If the directionality of propagation and outcoupling are caused by the total internal

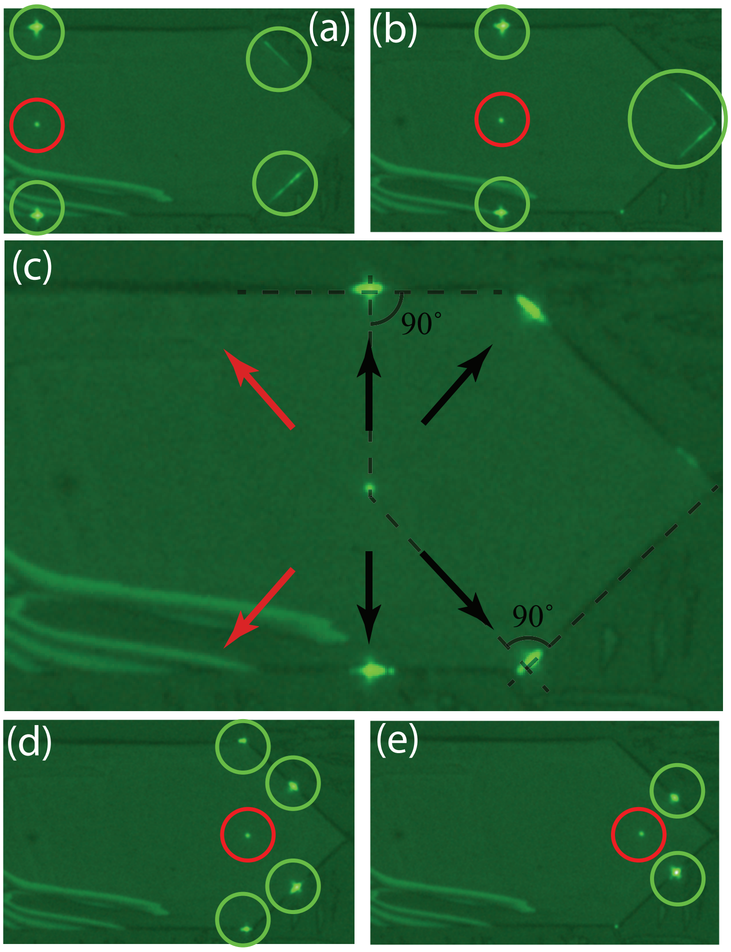

Figure 4.7: Propagation behaviour of the TPL in the DPFO microfibre. The excitation spot was gradually moved closer to the edge of the microfibre. (a) The spot marked with the red circle is the excitation spot, green circles mark the position of outcoupling at the edges and in the end of the microfibre; (b) The excitation spot was shifted closer to the end, the weak TPL distribution was changed; (c) Four well pronounced TPL spots. The outcoupling occurs only in the direction marked with black arrows and at 90° to the edge of the fibre; (d) Light can be outcoupled via the angles of the structures; (e) TPL propagates only in 2 directions as conditions are fulfilled only for the end of the structure.

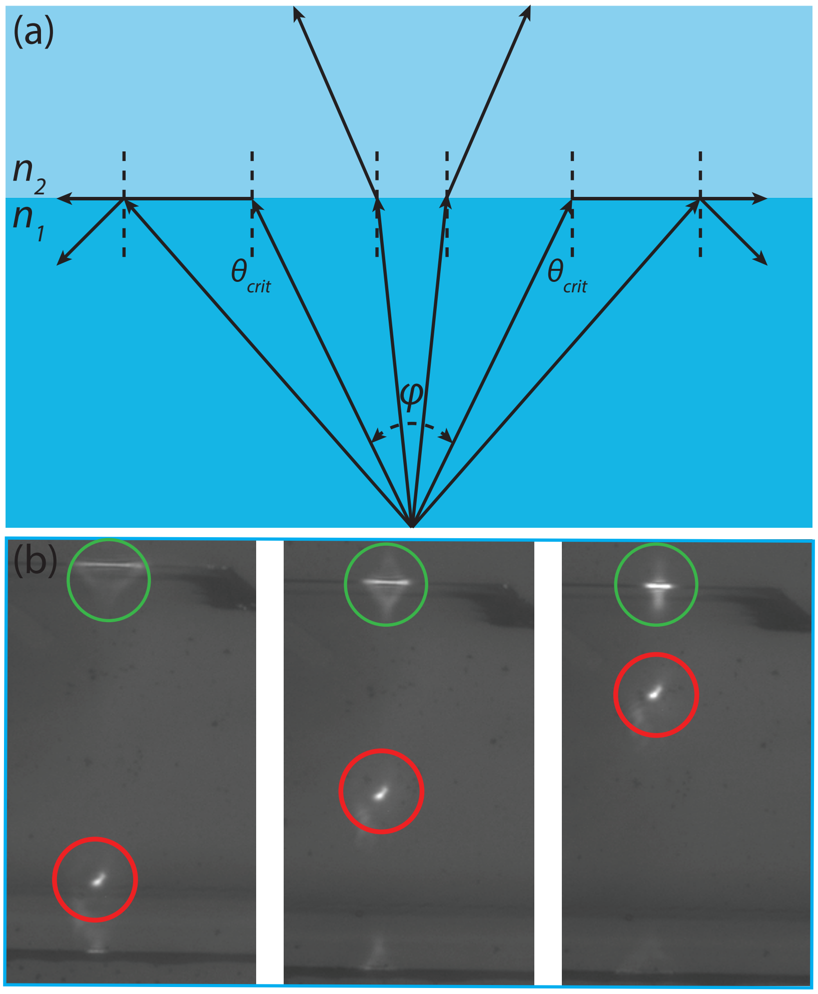

Figure 4.8: (a) Scheme of total internal reflection effect and its influence on the light outcoupling. (b) Waveguiding of TPL in the the DPFO fibres. Red circles mark the position of the excitation, while green circles mark position of the light outcoupling. Broadening of the outcoupling spot was observed as excitation was moved further from edge. This experiment allows to estimate divergence of the beam inside the DPFO microfibre and, therefore, calculate Θ_{crit} for the air/DPFO interface.

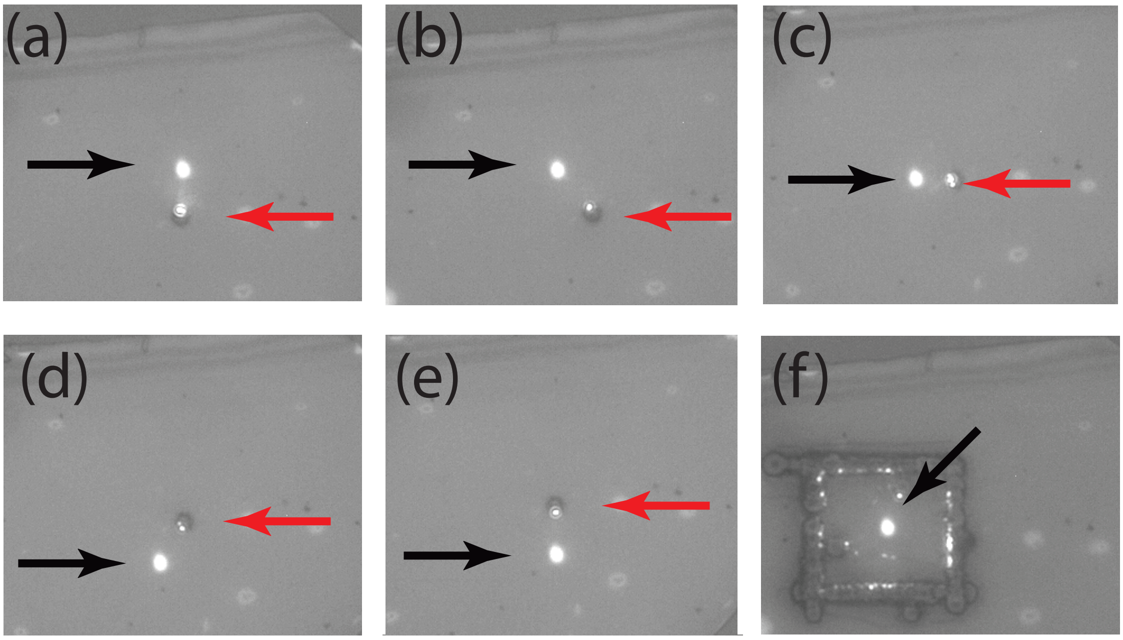

Figure 4.9: Influence of the artificial defect on the TPL propagation in the DPFO microfiber.(a)-(e) Excitation spot was moved around the defect in the DPFO microfiber. (f) Isotropic outcoupling of the TPL through rectangular defect. Black arrows correspond to place where microfiber was excited. Red arrows correspond to the defect where outcoupling was observed.

reflection effect, the refractive index difference between the DPFO microfibre and the environment should play a significant role. Increase of the environment refractive index should change the outcoupling efficiency, so the TPL light can exit the microfibre for a wider range of the angles of the propagated light. This should result in delocalisation of the outcoupled light. To check the influence of the environment, the sample was consequently covered with water ($n_{wat.} = 1.33$) and glycerine ($n_{glyc.} = 1.47$).

The results of these examinations are shown in fig. 4.10. Fig.4.10(a) shows the untreated sample, which demonstrates the previously described behaviour. We observe three light spots: one in the middle corresponds to the excitation spot, and two spot to the sides corresponds to the waveguided light (fig. 4.10(a)). After the DPFO sample was covered with water, light propagation was checked again (fig. 4.10(b)). Only a bright spot at the excitation spot was observed. DPFO microfibre covered with glycerine showed similar behaviour like in water, again no additional light spots were observed (4.10(d)). Note that, surrounded by the liquids the DPFO microfibre becomes less visible, since itsdd refractive index is close to the refractive index of DPFO. As a final check, after water or glycerine was removed, we observed the same effect as in the initial experiment (4.10(c)-(e)).

During the glycerine experiment, an air bubble was formed on the DPFO microfibre surface((4.10(f)) which allowed us to study both the DPFO/air and the DPFO/glycerine interface. Excitation of the DPFO microfibre close to the bubble resulted in the localization of the light on the DPFO/air interface, while no outcoupled light was observed on the DPFO/glycerine interface.

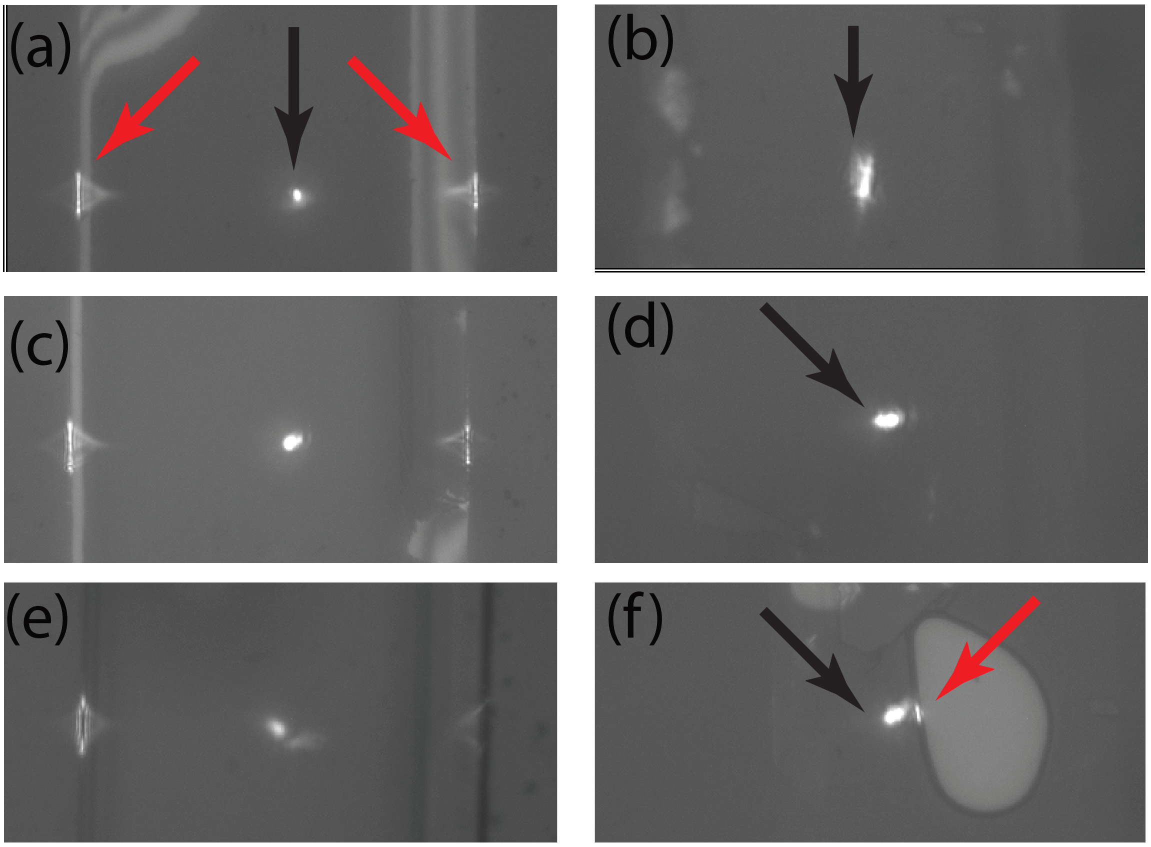

Figure 4.10: Dependence of the outcoupling efficiency on the environment refractive index.(a) Control experiment of the waveguiding in DPFO, air environment;(b) DPFO microfiber surrounded by water; (c) DPFO microfiber in air environment after water was removed;(d) DPFO microfiber in glycerine environment;(e) DPFO microfiber in air after glycerine was removed; (f) Waveguiding behaviour in glycerine with the excitation close to the air bubble. Black arrows mark the place of excitation. Red arrows mark the outcoupled light.

These results show a large influence of the environmental refractive index. Surrounded with liquids DPFO microfibres can not demonstrate light propagation and outcoupling. However, complete absence of the outcoupled light is not expected, as the total internal reflection predicts broadening of the outcoupled spot and not its complete disappearance.

All shown observations do not give a clear answer about the nature of the observed effect. Two possible models were proposed having drawbacks.

A further approach which is useful for our studies is to structure the sample with a focus ion beam (FIB), for the creation of precise artificial defects in the DPFO microfibre. We observed that the shape of the DPFO structure influences the outcoupling, hence different designs of the defects can help to understand anisotropy of light propagation or outcoupling and explore the possibility of optical device creation. Scanning near field optical microscopy (SNOM) could also be used for visualising the light propagation inside the DPFO microstructure. The later option goes beyond the present research and is left for the future investigations.

4.5 Conclusions

DPFO belongs to the class of molecules with intramolecular charge-transfer (ICT). The relatively large $\pi-$conjugation gives the possibility to observe strong linear and nonlinear optical responses in the visible range (wide luminescence peak with a maximum at 540 nm). Strong two-photon luminescence (TPL) was observed when the DPFO fibe was excited with a femtosecond laser at 800 nm. TPL is localised at the same spectral range as the spectra observed with single photon excitation.

In contrast to most other molecules with ICT, DPFO molecules can self-organize in a polar arrangement (microfibre) where the dipole moments are not compensated by adjacent molecules. Due to this fact, microfibres demonstrate SHG together with TPL. Both of the effects can be observed for a wide range of excitation wavelengths. Both linear and nonlinear optical properties makes this material interesting for photonic and optoelectronic applications.

As an example of such properties, we have demonstrated waveguiding of TPL in DPFO microfibres. Excited with the femtosecond laser, TPL can propagate through the fibre and can be outcoupled from the edges of the structure. Despite the usual isotropic behaviour of the luminescence, this propagating TPL showed novel and unique directionality and localization. Our observations demonstrate that waveguiding of the TPL in DPFO microfibres is not related to the crystal anisotropy, but depends on the refractive index of the environment. The total internal reflection effect can not be used for explanation of the observed effect, as it can not predict such strong localisation of the light. Use of SNOM and FIB techniques could give more details about the observed effect and its origin.

References

[1] D. Cotter, “Nonlinear optics for high-speed digital information processing,” *Science*, vol. 286, pp. 1523–1528, Nov. 1999.

[2] D. Smith, “Laser, nonlinear optics and optical computers,” *Nature*, vol. 316, p. 319, 1985.

[3] M. Cazzanelli, F. Bianco, E. Borga, G. Pucker, M. Ghulinyan, E. Degoli, E. Luppi, V. Véniard, S. Ossicini, D. Modotto, S. Wabnitz, R. Pierobon, and L. Pavesi, “Second-harmonic generation in silicon waveguides strained by silicon nitride.,” *Nat. Mat.*, vol. 11, pp. 148–54, Feb. 2012.

[4] J. Brewer, M. Schiek, a. Lützen, K. Al-Shamery, and H.-G. Rubahn, “Nanofiber frequency doublers.,” *Nano Lett.*, vol. 6, pp. 2656–9, Dec. 2006.

[5] J. E. Reeve, H. L. Anderson, and K. Clays, “Dyes for biological second harmonic generation imaging.,” *Phys. Chem. Chem. Phys.*, vol. 12, pp. 13484–98, Nov. 2010.

[6] C. Wang, T. Zhang, and W. Lin, “Rational synthesis of noncentrosymmetric metal-organic frameworks for second-order nonlinear optics.,” *Chem. Rev.*, vol. 112, pp. 1084–104, Feb. 2012.

[7] S. R. Marder, J. E. Sohn, and G. D. Stucky, *Materials for Nonlinear Optics*, vol. 455 of *ACS Symposium Series.* Washington, DC: American Chemical Society, Mar. 1991.

[8] G. S. He, L.-S. Tan, Q. Zheng, and P. N. Prasad, "Multiphoton absorbing materials: molecular designs, characterizations, and applications.," *Chem. Rev.*, vol. 108, pp. 1245–330, Apr. 2008.

[9] B. R. Cho, K. H. Son, S. H. Lee, Y.-s. Song, Y.-K. Lee, S.-j. Jeon, J. H. Choi, H. Lee, and M. Cho, "Two photon absorption properties of 1,3,5-tricyano-2,4,6-tris(styryl)benzene derivatives," *JACS*, vol. 123, pp. 10039–10045, Oct. 2001.

[10] J. Xu, L. Wen, W. Zhou, J. Lv, Y. Guo, M. Zhu, H. Liu, Y. Li, and L. Jiang, "Asymmetric and symmetric dipoledipole interactions drive distinct aggregation and emission behavior of intramolecular charge-transfer molecules," *J. Phys. Chem. C*, vol. 113, pp. 5924–5932, Apr. 2009.

[11] M. Albota, "Design of organic molecules with large two-photon absorption cross sections," *Science*, vol. 281, pp. 1653–1656, Sept. 1998.

[12] L. R. Dalton, A. W. Harper, R. Ghosn, W. H. Steier, M. Ziari, H. Fetterman, Y. Shi, R. V. Mustacich, A. K.-Y. Jen, and K. J. Shea, "Synthesis and processing of improved organic second-order nonlinear optical materials for applications in photonics," *Chem. of Mat.*, vol. 7, no. 6, pp. 1060–1081, 1995.

[13] K. D. Singer, J. E. Sohn, and S. J. Lalama, "Second harmonic generation in poled polymer films," *Appl. Phys. Lett.*, vol. 49, no. 5, p. 248, 1986.

[14] G. J. Ashwell, G. Jefferies, D. G. Hamilton, D. E. Lynch, M. P. S. Roberts, G. S. Bahra, and C. R. Brown, "Strong second-harmonic generation from centrosymmetric dyes," *Nature*, vol. 375, pp. 385–388, June 1995.

[15] G. R. Desiraju, "Supramolecular synthons in crystal engineering-a new organic synthesis," *Angew. Chem. Int. Ed.*, vol. 34, pp. 2311–2327, Nov. 1995.

[16] R. Yan, D. Gargas, and P. Yang, "Nanowire photonics," *Nat. Photon.*, vol. 3, pp. 569–576, Oct. 2009.

[17] J. Xu, H. Zheng, H. Liu, C. Zhou, Y. Zhao, Y. Li, and Y. Li, "Crystal hierarchical supramolecular architectures from 1-d precursor single-crystal seeds," *J. Phys. Chem. C*, vol. 114, pp. 2925–2931, Feb. 2010.

[18] J. Xu, S. Semin, D. Niedzialek, P. H. J. Kouwer, E. Fron, E. Coutino, M. Savoini, Y. Li, J. Hofkens, H. Uji-I, D. Beljonne, T. Rasing, and A. E. Rowan, "Self-assembled organic microfibers for nonlinear optics.," *Adv. Mat.*, vol. 25, pp. 2084–9, Apr. 2013.

[19] C. Chen, A. de Castro, and Y. Shen, "Surface-enhanced second-harmonic generation," *Phys. Rev. Lett.*, vol. 46, pp. 145–148, Jan. 1981.

[20] S. Brasselet, V. Le Floch, F. Treussart, J.-F. Roch, J. Zyss, E. Botzung-Appert, and A. Ibanez, “In situ diagnostics of the crystalline nature of single organic nanocrystals by nonlinear microscopy,” *Phys. Rev. Lett.*, vol. 92, p. 207401, May 2004.

[21] S. LeCours and H. Guan, “Push-pull arylethynyl porphyrins: new chromophores that exhibit large molecular first-order hyperpolarizabilities,” *JACS*, vol. 118, no. 15, pp. 1497–1503, 1996.

[22] J. C. Johnson, H. Yan, R. D. Schaller, P. B. Petersen, P. Yang, and R. J. Saykally, “Near-field imaging of nonlinear optical mixing in single zinc oxide nanowires,” *Nano Lett.*, vol. 2, pp. 279–283, Apr. 2002.

[23] R. M. Corn and D. a. Higgins, “Optical second harmonic generation as a probe of surface chemistry,” *Chem. Rev.*, vol. 94, pp. 107–125, Jan. 1994.

Summary

The development and investigation of new optical materials is of importance as it can lead to the observation of new physical phenomena and the discovery of new applications. The functional flexibility of organic molecules together with their ability to *self-assemble* into nano- and micro sized objects makes them promising to be useful for the growing area of miniaturized optical devices, as discussed in the Introduction.

This thesis contains optical studies of microsized objects fabricated via the self-assembly approach from two organic building blocks: diphenylalanine (FF) and 2,7-diphenyl-9H-fluoren-9-one (DPFO) molecules. Self-assembly is an example of a bottom-up approach for sample fabrication, i.e. the creation of complex objects from small building objects like atoms or molecules. Self-assembly exploits weak interactions: van der Waals forces, hydrogen bonds and π-interactions to arrange building blocks into nano and microobjects. After the general introduction to the field in chapter1, chapter 2 gave an introduction to the self-assembly process and the influence of the molecular and crystalline structure on the optical properties of organic materials, in particular the effects of extended π-conjugation and *chirality.* Conditions required for sample fabrication from FF and DPFO molecules are explained there.

Chapter 3 described the the light-matter interaction and optical effects which can be observed if an intense laser is used as a light source, such as non-linear effects as *two-photon luminescence* (TPL) and *second harmonic generation* (SHG). These effects can be observed as an absorption of two photons of incident light and the emission of one photon with exactly the double energy (for SHG) or smaller energy (for TPL). The first effect in general is nonresonant and is strongly related to the crystalline structure of the investigated material. The latter is resonant and originates form the energy levels of the molecules. Both of these effects can be used for characterisation of micro and nanoscale objects and can be observed when the samples are excited with a femtosecond laser. SHG and TPL are the basis for two-photon microscopy, a technique which is widely used for the study of biological cells and tissues, as it allows very local excitation of the samples resulting in high resolution 2D and 3D images. However as we do not limit our studies to nonlinear characterisation only, we also demonstrated that the investigated materials can be used as waveguides. We therefore described experimental set-ups which were used for nonlinear and waveguiding characterisation

of FF and DPFO microstructures.

In chapter 3 we studied the nonlinear optical properties of microtubes grown from water solution of FF molecules (FFMT). We demonstrated that as-grown FFMTs have a strong SHG response due to the lack of inversion symmetry of their crystal structure ($P6_1$ space group) which exhibits chirality (discussed in Chapter 1.1.3). The chiral arrangement of the FF molecules inside the microtube allows to observe chiroptical effects such as a difference of the SHG efficiency for right and left-circularly polarised light, i.e. the presence of SHG circular dichroism. The analysis of the data allows to conclude that the SHG response includes magnetodipole and electro quadrupole contributions.

It is known that FFMTs experience a *phase transition* when heated. The observed phase transition can be divided in two steps: one corresponds to the evaporation of the water molecules from the inner structure, the second one is caused by a molecular transformation. In our studies we observed a relation of the changes in the SHG response at this phase transition. Increasing of the laser fluence as well as heating of the sample results in a decrease of the SHG signal, which is an evidence of changes in the crystal structure of the FFMTs. At the same time we observe the appearance of two-photon luminescences in the green spectral range, originating from the treated regions of the sample. Such drastic changes can be also observed in the single photon luminescence signal. It shows a strong enhancement in the heated samples.

The undisturbed crystal structure of a FF-microtube clearly demonstrates *waveguiding*. Light propagation can be observed for wavelengths from the visible to near IR ranges of the spectrum. The local laser treatment of the FF-tube leads to the formation of regions which can generate TPL and act as a light source. The generated TPL can also propagate along the tube and be outcoupled from another defect or end of the tube. Both calculations and experiments demonstrate that the light is localised in the walls of the FFMT.

The observed appearance of TPL and the strong enhancement of the SPL in the heated FFMTs renews the interest in the self-assembled structures based on organic molecules with short conjugation, as it allows to obtain strong optical response in the visible range. Strong optical responses make these FF-microtubes structures promising candidates for photonic applications.

In chapter 4 we studied the nonlinear optical properties of DPFO microfibres, which belong to the class of molecules with intramolecular charge-transfer (ICT). The relatively large $\pi-$conjugation gives the possibility to observe strong linear and nonlinear optical responses in the visible range (wide luminescence peak with a maximum at 540 nm). Strong TPL was observed when the DPFO fibre was excited with the help of a femtosecond laser at 800 nm. The position of the TPL is similar to the position of the spectra observed with single photon excitation.

In contrast to most other ICT molecules, DPFO molecules can self-organise in a polar arrangement (microfibre) where the dipole moments are not compensated by adjacent molecules. Due to this, microfibres demonstrate SHG together with TPL. Both of these effects can be observed for a wide range of excitation wavelengths. Observed linear and nonlinear optical properties makes this material interesting for photonic and optoelectronic applications.

As an example of such applications, we demonstrated waveguiding of TPL in DPFO

microfibers. Excited with a femtosecond laser, TPL is shown to propagate in the bulk of the fibre and to couple out from the edges of the structure. Despite the usual isotropic behaviour of the luminescence, this propagating TPL showed unique directionality and localization. TPL light always outcouples if the direction of propagation is perpendicular to the edge of the structure. Our observations demonstrate that propagation of the TPL in DPFO microfibres is not related to the crystal anisotropy, but mainly depends on the refractive index of the environment. If the refractive index difference between the environment and the DPFO fibre decreases, no outcoupling is observed. The results presented in this thesis show the potential of organic molecules for photonic applications like nonlinear optics and waveguiding. Once we can control the self-organisation in predetermined structures, these potentially interesting materials can be fully explored.

Samenvatting

De ontwikkeling en onderzoek van nieuwe optische materialen is belangrijk omdat het tot de waarneming van nieuwe fysische verschijnselen en de ontdekking van nieuwe toepassingen kan leiden. De functionele flexibiliteit van organische moleculen met het vermogen via *self-assemblage* in nano- en micro objecten te creeren maakt ze veelbelovend bruikbaar voor toepassingen het groeiende gebied van geminiaturiseerde optische apparaten, zoals besproken in de inleiding.

Dit proefschrift bevat optische studies van micro objecten vervaardigd via de zelf-assemblage benadering van twee organische bouwstenen: diphenylalanine (FF) en 2,7-diphenyl-9H-fluoren-9-one (DPFO) moleculen. Zelf-assemblage is een voorbeeld van bottom-up benadering voor het maken van materialen, dat wil zeggen het creren van complexe objecten met behulp van kleine bouwsteen zoals atomen of moleculen. Zelforganisatie exploiteert zwakke interacties: van der Waals krachten, waterstof bindingen en π-interacties. Na de algemene inleiding op het veld in hoofdstuk 1, bevat hoofdstuk 2 een inleiding tot het zelf-assemblage proces en de invloed van de moleculaire en kristallijne structuur op de optische eigenschappen van organisch materialen, in het bijzonder de effecten van de uitgebreide π -conjugatie en *chiraliteit*. Voorwaarden die nodig zijn voor het samples fabricage van FF en DPFO moleculen worden er toegelicht.

Hoofdstuk 3 beschrijft de licht-materie interactie en de optische effecten die kunnen worden waargenomen als een intense laser wordt gebruikt als lichtbron. We introduceren niet-lineaire optische effecten als *twee-foton luminescentie* (TFL) en *tweede harmonische generatie* (THG). Deze effecten kunnen worden waargenomen als een absorptie van twee fotonen van het invallend licht en de emissie van een foton met precies de dubbele energie (voor THG) of een kleinere energie (voor TFL). Het eerste effect is in het algemeen niet resonant en is sterk gerelateerd aan de kristallijne structuur van het onderzochte materiaal. Laatstgenoemde effect is resonant en afkomstig van de energieniveaus van de moleculen. Beide effecten kunnen worden gebruikt voor de karakterisering van micro- en nanoschaal objecten wanneer de samples worden geexciteerd met een femtoseconde laser. Bijvoorbeeld, THG en TFL zijn de basis voor twee-foton microscopie, een techniek die algemeen wordt gebruikt voor de studie van biologische cellen en weefsels, omdat hiermee zeer lokale excitatie van de samples resulteerde in hoge resolutie 2D- en 3D-beelden. Maar aangezien we onze studies niet alleen tot niet-lineaire karakterisering beperken, hebben we ook geconstateerd dat de onderzochte materialen kunnen worden gebruikt als golfgeleiders. We beschrijven experimentele set-ups die werden gebruikt voor de karakterisering van niet-lineaire en golfgeleideinde eigenschappen van FF en DPFO microstructuren.

In hoofdstuk 4 bestuderen we de niet-lineaire optische eigenschappen van microfibres gegroeid uit een water oplossing van FF moleculen (FFMT). De vers gegroeide FFMTs vertonen een sterke THG respons door het ontbreken van inversiesymmetrie in hun kristalstructuur ($P6_1$ ruimtegroep), dat ook chiraliteit vertoont (besproken in hoofdstuk 1.1.3). De chirale ordening van de FF moleculen in de microfiber maakt het mogelijk om chiroptische effecten zoals een verschil van de THG efficientie voor rechts en links-circulair gepolariseerd licht waar te nemen, dat wil zeggen de aanwezigheid van THG circulair dichroisme. De analyse van de data maakt het mogelijk om te concluderen dat de THG response magnetische dipool en electro-quadrupool bijdragen bevat.

Het is bekend dat FFMTs een *faseovergang* vertonen bij verhitting. De waargenomen faseovergang kan worden onderverdeeld in twee stappen: de eerste gaat gepaard met de verdamping van de water moleculen uit de binnenstructuur, terwijl tweede gekarakteriseerd wordt door een moleculaire transformatie. In onze studies zien we een relatie tussen de veranderingen in de THG respons en deze faseovergang. Vergroting van de laser intensiteit en verwarming van het sample resulteert in een afname van het THG signaal, een bewijs voor de veranderingen in de kristalstructuur van de FFMTs. Tegelijkertijd zien we het verschijnen van twee-foton luminescentie in het groene spectrale gebied, afkomstig van de behandelde gebieden van het sample. Deze drastische veranderingen kunnen ook worden waargenomen in het normale luminescentiesignaal. Het toont een sterke toename in de verwarmde samples.

De ongestoorde kristalstructuur van een FF-microtube toont duidelijk *een golfgebieder* karakter. Lichtpropagatie kan worden waargenomen voor golflengten van het zichtbare tot het nabije IR bereik van het spectrum. De lokale laserbehandeling van deen FF-buis leidt tot de vorming van gebieden die TFL kunnen genereren en werken als een lichtbron. De gegenereerde TFL kan zich voortplanten langs de fiber en wordt geuitkoppeld via een ander dislocatie of aan einde van de fiber. Zowel berekeningen als experimenten tonen aan dat het licht gelokaliseerd wordt in de wanden van de FFMT.

Het verschrijven van TFL en de sterke toename van de SFL in de verwarmde FFMT's vernieuwt de interesse in de zelf-geassembleerde structuren op basis van organische moleculen met korte conjugatie, omdat hiermee een sterke optische respons in het zichtbare gebied wordt bereik. De sterke optische respons maken deze FF-microtubes structuren veelbelovende kandidaten voor fotonische toepassingen.

In hoofdstuk 5 bestuderen we de niet-lineaire optische eigenschappen van DPFO microvezels, die behoren tot de klasse van moleculen met intramoleculaire ladingsoverdracht (ICT). De relatief grote $\pi-$ conjugatie geeft de mogelijkheid om sterke lineaire en niet-lineaire optische respons in het zichtbare gebied (brede luminescentie piek met een maximum bij 540 nm) te observeren. Een sterke TFL signaal werd waargenomen wanneer de DPFO vezel werd gexciteerd met behulp van een femtoseconde laser bij 800 nm. Het spectrum van de TFL is vergelijkbaar met de spectra waargenomen met enkele foton excitatie.

In tegenstelling tot de meeste andere ICT-moleculen,kunnen DPFO moleculen zichzelf organiseren in een polaire structuur (microvezel) waar de dipoolmomenten niet worden gecompenseerd door aangrenzende moleculen. Hierdoor tonen de microvezels THG samen met TFL. Beide effecten kunnen worden waargenomen voor diverse golflengten. Waargenomen lineaire en niet-lineaire optische eigenschappen maken dit materiaal interessant voor fotonische en opto-elektronische toepassingen.

Als voorbeeld van dergelijke toepassingen hebben we golfgeleiding aangetoond van TFL in DPFO microvezels. Opgewekte TFL met een femtosecondelaser blijkt zich te verspreiden in de bulk van de vezel en niet te koppelen langs de randen van de structuur. Ondanks het gebruikelijke isotrope gedrag van de luminescentie, bleek de TFL in deze structuren zich in unieke richting en uit te koppelen, namelijk altijd loodrecht ten opzichte van de rand en van de structuur. Uit onze observatie blijkt dat de propagatie van TFL in DPFO microvezels niet gerelateerd is aan de kristal anisotropie, maar voornamelijk afhankelijk is van de brekingsindex van de omgeving. Indien het verschil in brekingsindex tussen de omgeving en de DPFO vezel afneemt, verdwijnt de uitkoppeling.

De resultaten in dit proefschrift laten het potentiaal zich van organische moleculen voor fotonische toepassingen zoals niet lineaire optica en golfgeleiding. Als de zelforganiatie gecontroleerd kan worden zodat deze plaats vindt in van te vorm bepaalde gewenste structuur dan kunnen deze materialen tot interessante toepassingen leiden.

List of publications

- **S. Semin**, A. van Etteger and Th. Rasing,“Two-regime Waveguiding in Self-assembled Peptide Tubes”, (in preparation).

- **S. Semin**, J. Xu, H. Salemink, P. Alkemade, A. van Etteger, and Th. Rasing, “Unique Directional and Localised Waveguiding in DPFO Microfibers”, (in preparation).

- J. Xu, **S. Semin**, J. Cremers, L. Wang, E. Fron, E. Coutino, M. Savoini, T. Chervy, C. Wang, Y. Li, H. Liu, Y. Li, P. H. J. Kouwer, T. W. Ebbesen, J. Hofkens, D. Beljonne, A. E. Rowan, and Th. Rasing, “Controlling Microsized Polymorphism Architectures with Distinct Linear and Nonlinear Optical Properties”, *Adv. Opt. Mat.*, accepted, 2015.

- M. De Torres, **S. Semin**, I. Razdolski, J. Xu, J.A.A.W. Elemans, T. Rasing, A. Rowan, R.J.M. Nolte, “Extended π-conjugated ruthenium zinc-porphyrin complexes with enhanced nonlinear-optical properties”, *Chem. Comm.*, 51, 2855-2858, 2015

- J. Xu, **S. Semin**, Th. Rasing, A. E. Rowan, “Organized Chromophoric Assemblies for Nonlinear Optical Materials: Towards (Sub) wavelength Scale Architectures”, *Small*, 11, 2015.

- **S. Semin**, A. van Etteger, L. Cattaneo, N. Amdursky, L. Kulyuk, S. Lavrov, A.Sigov, E. Mishina, G. Rosenman, and Th. Rasing, “Strong Thermo-Induced Single And Two-Photon Green Luminescence in Self-Organized Peptide Microtubes”, *Small*, 11, 2015.

- J. Xu, **S. Semin**, D. Niedzialek, P.H.J. Kouwer, E. Fron, E. Coutino, M.Savoini, Y.Li, J. Hofkens, H. Uji-I, D. Beljonne, Th. Rasing , and A. E. Rowan, “Self-Assembled Organic Microfibers for Nonlinear Optics”, *Advanced Materials*, 25(14), 2084, 2013.

- N. Amdursky, P. Beker, I. Koren, B. Bank-Srour, E. Mishina, **S. Semin**, and G. Rosenman, “Structural Transition in Peptide Nanotubes”, *Biomacromolecules*, 12(4), 134954, 2011.
- A. Heredia, I. Bdikin, S. Kopyl, E. Mishina, **S. Semin**, A. Sigov, K. German, V. Bystrov, J. Gracio, A.L. Kholkin,“Temperature-driven phase transformation in self-assembled diphenylalanine peptide nanotubes”, *J. Phys. D: Appl. Phys.*, vol. 43(46), 462001, 2010

Curriculum Vitae

Personal details

Name: Sergey Vladimirovich Semin

Date of birth: January 24, 1986

Place of birth: Bolgrad, USSR

E-mail: s.semin@science.ru.nl

Education

2011 - 2015	Radboud University Nijmegen, the Netherlands PhD research in Physics
2009 - 2011	Moscow State Institute of Radio Engineering, Electronics and Automation, Radio physics and electronics, PhD research in Physics Moscow, Russian Federation
2003 - 2008	Moscow State Institute of Radio Engineering, Electronics and Automation, Radio physics and electronics, Specialist (MSc equivalent), Moscow, Russian Federation Graduate work “Nonlinear optical properties of photonic crystals”
1993 - 2003	General education secondary (high) school 1066, Moscow, Russian Federation